学位論文

Phenomenology of Bino-Higgsino Resonant Dark Matter

(Bino-Higgsino共鳴暗黒物質の現象論)

平成27年12月博士（理学）申請

東京大学大学院理学系研究科
物理学専攻

石川　和哉

Abstract

The LHC discovered the Higgs boson but has not discovered any supersymmetric (SUSY) particles. The heavy sfermion scenario, or the SUSY scenario in which the SUSY scalar partners of the SM fermions (sfermions) are heavy $> \mathcal{O}(1\text{–}10)$TeV, is compatible with these results. In addition, the constraints from the flavor changing neutral current problem is relaxed. Thus, the heavy sfermion scenarios have attracted attentions. In this case, the neutralino lightest SUSY particle (LSP) can be the candidate for the dark matter (DM) only in limited cases. The Bino-Higgsino resonant DM model is one of the attractive models. In this model, the DM candidate is the Bino LSP which mixes with the Higgsino slightly. When the mass of the LSP is half of the Higgs boson mass or the Z boson mass, the current relic abundance can be explained with the resonant annihilation.

This model contains the light DM (Bino LSP) with the $\mathcal{O}(10)$ GeV mass and the heavy neutralinos and the chargino (Higgsinos) with the $\mathcal{O}(100)$ GeV masses. It makes the phenomenology rich in many experiments. Especially, the direct detections, the invisible decay and the LHC searches are sensitive to this model. In this thesis, we investigate the phenomenology of the Bino-Higgsino resonant DM model with combining these experiments. We consider the case that all the sfermions are heavy and the model is described by only three SUSY parameters. We study all parameter space comprehensively to investigate the rich phenomenology especially in the blind spot where the DM-DM-Higgs couplings vanishes. As a result, it is shown that there is still large viable parameter space. It is also shown that the combination of the future experiments can reveal almost all region of this model.

Contents

List of Figures

List of Tables

Chapter 1

Introduction

The standard model (SM) is a well-established model which can explain many experimental results in the particle physics. In addition, the Higgs boson was discovered at the LHC in July 2012 [1, 2]. Although all particles in the SM have been found, there are still many problems and mysteries about the SM. For example, there exists the hierarchy problem and there is no candidate for the dark matter (DM). To solve these problems, supersymmetric (SUSY) model is considered as one of the promising candidates for the new physics models beyond the SM [3, 4].

SUSY is the symmetry between bosons and fermions, and SUSY models contain the partner particle (SUSY particle) for each SM particle. The contributions from the SUSY particles cancel out the quadratic divergence of the quantum corrections to the Higgs boson mass. Although the little fine tuning with the size of $\mathcal{O}(10^{-2} \sim 10^{-6})$ remains, the hierarchy problem which need the unnatural fine tuning with the size of $\mathcal{O}(10^{-32})$ is solved. In addition, the lightest SUSY particle (LSP) can be a dark matter candidate if the R-parity is conserved.

To search these SUSY particles directly, the LHC had run at $\sqrt{s}$ =7 TeV during 2010 to 2011, at 8 TeV during 2012 and the LHC is running at 13 TeV now (from 2015). However, there is no sign of new particles yet and the mass bounds for new particles have been becoming stronger. For example, the squark mass should be larger than 1.6 TeV and the lower mass bound for the gluino is 1.4 TeV in mSUGRA model [5]. In addition, the masses of the stops are required to be heavier than $\mathcal{O}$(1–10) TeV to explain the Higgs boson mass 125GeV in the minimal SUSY extension of the SM (MSSM) [6–8]. From these facts, the heavy sfermion scenarios, or the SUSY scenarios in which the scalar partners of the SM fermions (sfermions) are heavy $> \mathcal{O}$(1–10) TeV, have attracted attentions [9–16]. In these scenarios, not only the Higgs boson mass can be explained but also the constraints from the LHC can be evaded. In addition, the constraints from the flavor changing neutral current (FCNC) problem are also relaxed [17, 18]. Thus, the heavy sfermion scenarios are considered as one of the attractive SUSY scenarios. We consider the heavy sfermion scenario in this thesis.

In the heavy sfermion scenario, although the lightest neutralino can be a DM candidate, the correct thermal relic abundance, $\Omega_\chi \simeq 0.120$ [19], can be obtained only in limited cases. It

happens when the mass of the pure Wino DM is about 3 TeV [20, 21], when the mass of the (almost) pure Higgsino DM is about 1 TeV [21,22], when the gaugino coannihilation occurs [23–27] or when the Bino mixes with the Higgsino sizably [28–36].

The Wino DM and the Higgsino DM with the mass $\mathcal{O}(100)$ GeV tend to give small thermal relic abundance since they can annihilate to the SM particles effectively. Since heavier mass decreases the annihilation cross section, the mass of the Wino (Higgsino) should be 3 (1) TeV to explain the current relic abundance [20–22]. In contrast, the Bino DM is typically overabundant if all the sfermions are heavy $> \mathcal{O}(1\text{–}10)$ TeV and the mixing with the Higgsinos is small. There are two ways for the Bino DM to give the correct thermal relic abundance: the Bino DM coannihilates with the other gauginos, or the mixing with the Higgsinos become sizable with $\mathcal{O}(100)$ GeV Higgsinos. The former case, the gaugino coannihilation scenario, is valid for the DM mass $\mathcal{O}(0.1\text{–}1)$ TeV [23–27]. In this case, with nearly degenerated Bino and gauginos, the coannihilation can decrease the number density of the DM and the current relic abundance can be obtained. The latter case, the Bino-Higgsino DM scenario, has two parameter regions: where the Bino-Higgsino mixing is tuned (well-tempered scenario) [28–30], and where the DM annihilate resonantly via the Higgs boson or the Z boson (resonant scenario) [30–37]. In the well-tempered scenario, the Higgsinos are nearly degenerated with the Bino. The mixing between the Bino and the Higgsino is maximized and the coannihilations among the neutralinos and chargino become also effective. These make the DM annihilation cross section large and the current relic abundance can be explained. However, almost all region except the blind spot where the DM-Higgs coupling vanishes [38] is excluded already [38, 39]. In the resonant scenario, although the mixing between the Bino and the Higgsino is not so large as the well-tempered model, the resonant annihilation can enhance the DM annihilation cross section. It happens when the mass of the DM, $m_{\chi_1^0}$, is a half of the Higgs boson or the Z boson, $m_{\chi_1^0} \sim m_h/2$ or $M_Z/2$, and the DM annihilation cross section is enhanced by the Higgs- or Z-resonance. In these regions, the DM mass is less than 100 GeV and the masses of the second and third heavier neutralino and the lightest chargino are $\mathcal{O}(0.1\text{–}1)$ TeV.

Although the heavy sfermion scenario is one of the attractive SUSY scenarios, the sfermions are heavy and it is difficult to search them directly by the experiments. Thus, the studies about the neutralinos/charginos, especially the DM, become necessary. Among the above DM models, the Bino-Higgsino resonant DM model gives variety of phenomena in the energy scale 10$\sim$1000 GeV: the DM scattering with nuclei, the invisible decays of the Higgs/Z boson to the DMs and the productions of the heavy neutralinos/chargino at the colliders. Thus, there are rich phenomena in the experiments even in the case where all the sfermions are heavy. Studying such phenomenology is important not only theoretically but also experimentally since the combining the results of various experiments is shown to be important to reveal this SUSY scenario. Thus, we study the phenomenology of the Bino-Higgsino resonant DM model in this thesis.

To investigate this Bino-Higgsino resonant model comprehensively, we include the following experimental constraints and future prospects: the relic abundance [19], the DM direct detec-

tion [40–43], the invisible decays of the Higgs/Z boson [44–49] and the chargino/neutralino searches [50, 51]. In this thesis, we assume the gluino and the Winos are heavier than a few TeV while the sfermions are assumed to be heavy $> \mathcal{O}(1\text{–}10)$ TeV. This is because the Wino with the mass $\gtrsim$ 500–700 GeV and the gluino do not affect the DM phenomenology. In addition, since the existence of $\mathcal{O}(100)$ GeV gluino and Winos enlarges the covered region of the constraints and the future prospects of the LHC SUSY searches, to evade the constraints and to give the conservative future prospects, we assume they do not contribute to the LHC SUSY searches. Thus, the gluino and the Winos are assumed to be heavier than a few TeV and we do not consider their effects. Then, the model is determined only by the three parameters: the Bino mass, M_1, the Higgsino mass, μ, and the ratio of the up-type and down-type Higgs vacuum expectation value, $\tan\beta$. Nevertheless, this scenario gives a variety of phenomena, especially near the blind spot where the DM-Higgs coupling vanishes. We will show that large parameter region is still viable and almost all region will be searched complementarily by the future experiments.

Let us comment on the standpoint of our study. There are studies which investigate the Bino-Higgsino DM model with resonant annihilation [32–36]. However, in these papers, only the scatter plots are performed. In contrast, we investigate essentially the whole parameter space of $(M_1, \mu, \tan\beta)$. It makes the existence of the blind spot clear, and the importance of it for the phenomenology is emphasized in our study which none of the previous works has done. In addition, we comprehensively include all the possible phenomena and experiments. Although the study for the spin independent (SI) cross section is performed in all papers [32–37], the study of the spin dependent (SD) cross section is partially done only in Ref. [36] . The Higgs boson invisible decay is also only commented in Ref. [33]. The LHC search with the 8 TeV analysis is investigated in Ref. [34–36]. On the other hand, the 14 TeV prospects are discussed with their original analysis only up to $m_{\chi_2^0} < 320$ GeV in Ref. [34]. Furthermore, none of the previous studies have analyzed the 14 TeV LHC prospects for the current model by using the results of the LHC [51]. We investigate all these phenomenology and show the importance of combining these experiments.

This thesis is based on the work by the author [52].

This thesis is outlined as follows.

First, in Chapter 2, we review the SUSY models. The minimal SUSY extension of the SM (MSSM) and the heavy sfermion models are reviewed. We also review the Bino-Higgsino resonant DM model briefly in Sec. 2.2.6.

Second, in Chapter 3, we review the phenomenology of the DM, especially of the Majorana DM. The thermal relic abundance, the direct detections, the invisible decays, the collider searches and the indirect detections are reviewed.

Then in Chapter 4, we introduce the Bino-Higgsino resonant DM model which we investigate in this thesis. The typical behavior of the masses and the couplings are also shown. We discuss the blind spot and the typical behavior of the heavy neutralinos/chargino at the LHC.

We analyze the Bino-Higgsino resonant DM model in Chapter 5. We calculate, analyze and discuss the following phenomena: relic abundance, SI scattering, SD Scattering, invisible decay, heavy neutralinos/chargino searches at the LHC, mono-photon/jet searches and indirect detections. We show the calculation of our analysis and the method of the simulations.

The results of our analysis are shown in Sec. 6. Especially, the main results are given in Figures 6.1–6.5. Sec. 7 is devoted to the conclusion.

In Appendix A, we show the SM values used in this thesis. We show the Wino contributions to the DM phenomenology in Appendix B. In Appendix C, we show the analytical calculations in the Bino-Higgsino resonant model. Especially, we perform $\mathcal{O}(M_Z s_W/\mu)$ expansion. Appendix D is devoted to the detailed calculation whose results are used in our analysis. Finally, in Appendix E, we show the validation of our analysis for the LHC searches.

Chapter 2

Supersymmetry

The standard model (SM) is a well-established model in the particle physics. However, there is a hierarchy problem and the SM does not have a candidate for the dark matter (DM). As one of the solutions to these problems, supersymmetry (SUSY) is considered to be a promising candidate for new physics beyond the SM [3]. Here, we briefly review SUSY models, especially the minimal SUSY extension of the SM (MSSM) in Sec. 2.1 and the heavy sfermion models in Sec. 2.2.

2.1 MSSM

First, we introduce the minimal SUSY extension of the SM (MSSM). Since SUSY is the symmetry between bosons and fermions, it adds the new partner particles (SUSY particles) for each SM particle (see Sec. 2.1.1). In Sec. 2.1.2, we see the spontaneous symmetry breaking of the Higgs fields. We show the solution to the hierarchy problem in Sec. 2.1.3: the contributions from the SUSY particles cancel out the quadratic divergence of the quantum corrections to the Higgs boson mass. In addition, the MSSM contains the candidate for the DM if the R-parity is conserved (Sec. 2.1.4). In this case, the lightest SUSY particle (LSP) can be a candidate for the DM. We also review the constraints from the Higgs boson mass (Sec. 2.1.5), the LHC searches (Sec. 2.1.6) and the FCNC problem (Sec. 2.1.7).

2.1.1 Lagrangian

The matter content of the MSSM is shown in Table 2.1. The charges under the gauge ($\mathrm{SU}(3)_C$, $\mathrm{SU}(2)_L$, $\mathrm{U}(1)_Y$) and the global symmetry ($\mathrm{U}(1)_B$ and $\mathrm{U}(1)_L$) are also shown. Note that two Higgs multiplets are necessary due to the holomorphy of the superpotential and the anomaly cancelation.

In the SUSY, the fermion χ_X and its corresponding boson ϕ_X are combined into one superfield with the superspace coordinates $\theta, \bar{\theta}$ and the auxiliary field. The chiral superfield X is

superfield	boson	fermion	$SU(3)_C$	$SU(2)_L$	$U(1)_Y$	$U(1)_B$	$U(1)_L$
L_f	$\phi_{lf} = \begin{pmatrix} \phi_{\nu f} \\ \phi_{ef} \end{pmatrix}$	$\chi_{lf} = \begin{pmatrix} \chi_{\nu f} \\ \chi_{ef} \end{pmatrix}$	1	2	-1/2	0	1
$\overline{E}_f$	$\phi_{\bar{e}f}$	$\chi_{\bar{e}f}$	1	1	1	0	-1
Q_f	$\phi_{qf} = \begin{pmatrix} \phi_{uf} \\ \phi_{df} \end{pmatrix}$	$\chi_{qf} = \begin{pmatrix} \chi_{uf} \\ \chi_{df} \end{pmatrix}$	3	2	1/6	1/3	0
$\overline{U}_f$	$\phi_{\bar{u}f}$	$\chi_{\bar{u}f}$	$\overline{3}$	1	-2/3	-1/3	0
$\overline{D}_f$	$\phi_{\bar{d}f}$	$\chi_{\bar{d}f}$	$\overline{3}$	1	1/3	-1/3	0
B	B_μ	χ_B	1	1	0	0	0
W^i	$W^i_\mu \quad (i = 1 \sim 3)$	χ^i_W	1	3	0	0	0
G^a	$G^a_\mu \quad (a = 1 \sim 8)$	χ^a_G	8	1	0	0	0
H_u	$H_u = \begin{pmatrix} H_u^+ \\ H_u^0 \end{pmatrix}$	$\chi_{H_u} = \begin{pmatrix} \chi_{H_u^+} \\ \chi_{H_u^0} \end{pmatrix}$	1	2	1/2	0	0
H_d	$H_d = \begin{pmatrix} H_d^0 \\ H_d^- \end{pmatrix}$	$\chi_{H_d} = \begin{pmatrix} \chi_{H_d^0} \\ \chi_{H_d^-} \end{pmatrix}$	1	2	-1/2	0	0

Table 2.1: Matter content of the MSSM. The subscript f denotes the family and $f = 1, 2, 3$.

written with the auxiliary field F_X as [4]

$$X = \phi_X(y) + \sqrt{2}\theta\chi_X(y) + \theta\theta F_X(y)\,, \tag{2.1}$$

where $y^\mu = x^\mu + i\bar{\theta}\bar{\sigma}^\mu\theta$. The vector superfield V^a for the gauge field is written with the auxiliary field D^a in the Wess-Zumino gauge as

$$V^a = \bar{\theta}\bar{\sigma}^\mu\theta V^a_\mu(y) + \bar{\theta}\bar{\theta}\theta\chi_V(y) + \theta\theta\bar{\theta}\bar{\chi}_V(y) + \frac{1}{2}\theta\theta\bar{\theta}\bar{\theta}D^a_V(y)\,. \tag{2.2}$$

The field strength W^a_α of the vector superfield V^a where α is a spinor index is also written with the field strength of the gauge field $F^a_{\mu\nu}$ as

$$W^a_\alpha = (\chi^a_V)_\alpha + \theta_\alpha D^a + \frac{1}{2}i\left(\sigma^\mu\bar{\sigma}^\nu\theta\right)_\alpha F^a_{\mu\nu} + i\theta\theta\left(\sigma_\mu\nabla^\mu\bar{\chi}^a_V\right)_\alpha\,, \tag{2.3}$$

where $\nabla^\mu\bar{\chi}^a_V = \partial^\mu\bar{\chi}^a_V + g_V f^{abc}V^b_\mu\bar{\chi}^c_V$.[1] Here, g_V denotes the gauge coupling for the gauge field V where g', g, g_s are the $U(1)_Y$, $SU(2)_L$, $SU(3)_C$ gauge couplings respectively. f^{abc} is the structure constant of the gauge $\left[T^a, T^b\right] = if^{abc}T^c$ and T^a is the representation matrix of $SU(2)_L$ and $SU(3)_C$.

The Lagrangian is composed of the Kähler potential which includes kinetic terms, the superpotential and the field strength terms as [4]

$$L = \int d\theta^2 d\bar{\theta}^2 K + \left(\int d\theta^2 W + h.c.\right) + \frac{1}{4}\sum_V\left(\int d\theta^2 W_\alpha W^\alpha + h.c.\right)\,. \tag{2.4}$$

[1] Note that for $U(1)_Y$, the superscript a does not exist and $\nabla^\mu\bar{\chi}_B = \partial^\mu\bar{\chi}_B$.

K is the Kähler potential

$$K = \sum_P X_P^\dagger e^{\sum_V 2g_V T^a V^a} X_P \,, \tag{2.5}$$

where P runs all the chiral superfields. W is the superpotential

$$W = \sum_{f,f'=1}^{3} \left(-Y_e^{ff'}(L_f \cdot H_d)\overline{E}_{f'} + Y_u^{ff'}(Q_f \cdot H_u)\overline{U}_{f'} - Y_d^{ff'}(Q_f \cdot H_d)\overline{D}_{f'} + \mu H_u \cdot H_d \right) , \tag{2.6}$$

with Yukawa couplings Y and the mu parameter μ.[2] After the auxiliary fields are integrated out, the Lagrangian becomes as:

$$\begin{aligned} L \;=\; & -\frac{1}{4}F_{\mu\nu}F^{\mu\nu} + i\overline{\chi}_B\overline{\sigma}^\mu\partial_\mu\chi_B - \frac{1}{4}W^i_{\mu\nu}W^{i\mu\nu} + i\overline{\chi}^i_W\overline{\sigma}^\mu D_\mu\chi^i_W - \frac{1}{4}G^a_{\mu\nu}G^{a\mu\nu} + i\overline{\chi}^a_G\overline{\sigma}^\mu D_\mu\chi^a_G \\ & + \sum_P \Big[(D_\mu\phi_P)^\dagger D_\mu\phi_P \; + i\overline{\chi}_P\overline{\sigma}^\mu D_\mu\chi_P - \sqrt{2}Y_P g' \left(\phi_P^\dagger\chi_B\cdot\chi_P + \overline{\chi}_P\cdot\overline{\chi}_B\phi_P \right) \\ & - \sqrt{2}g \left(\phi_P^\dagger\chi^i_W T^i\cdot\chi_P + \overline{\chi}_P\cdot\overline{\chi}^i_W T^i\phi_P \right) - \sqrt{2}g_s \left(\phi_P^\dagger\chi^a_G T^a\cdot\chi_P + \overline{\chi}_P\cdot\overline{\chi}^a_G T^a\phi_P \right) \Big] \\ & - \mu\chi_{H_u}\chi_{H_d} - \sum_{\{p_1,p_2,p_3,p_4\}} Y_{p_1}\left(\phi_{p_2}\chi_{p_3}\chi_{p_4} + \phi_{p_3}\chi_{p_2}\chi_{p_4} + \phi_{p_4}\chi_{p_2}\chi_{p_3}\right) + h.c. \\ & - |\mu|^2\left(|H_u|^2 + |H_d|^2\right) - \sum_{\{p_1,p_2,p_3,p_4\}} |Y_{p_1}|^2 \left(|\phi_{p_2}\phi_{p_3}|^2 + |\phi_{p_2}\phi_{p_4}|^2 + |\phi_{p_3}\phi_{p_4}|^2 \right) \\ & - \frac{g'^2}{2}\left(\sum_P Y_P\phi_P^\dagger\phi_P\right)^2 - \frac{g^2}{2}\left(\sum_P \phi_P^\dagger T^i\phi_P\right)^2 - \frac{g_s^2}{2}\left(\sum_P \phi_P^\dagger T^a\phi_P\right)^2 , \end{aligned} \tag{2.7}$$

where P runs all the superfields and $\{p_1,p_2,p_3,p_4\} = \{e_f, H_d, L_f, \bar{E}_f\}, \{u_f, H_u, Q_f, \bar{U}_f\}, \{d_f, H_d, Q_f, \bar{D}_f\}$. Y_P is a charge of $\mathrm{U}(1)_Y$ for multiplet P and T^i, T^a are the representation matrices of $\mathrm{SU}(2)_L$, $\mathrm{SU}(3)_C$.

At this stage, the SUSY particles' masses are the same as the SM particles. However, since the SUSY particles which have such masses are not discovered, the SUSY should be broken and the masses of the SUSY particles should be increased. In order not to violate the cancellation of the quadratic divergence, the SUSY should be broken softly. The breaking terms are called soft terms and given as [4]

$$\begin{aligned} L_{soft} = & -\frac{1}{2}\sum_{X=B,W,G} M_X\chi_X^{(i)}\cdot\chi_X^{(i)} + h.c. - \sum_{P,ff'} m^2_{\tilde{P}ff'}\phi^\dagger_{Pf}\phi_{Pf'} - m^2_{H_u}H_u^\dagger H_u - m^2_{H_d}H_d^\dagger H_d \\ & - \sum_{f,f'=1}^{3}\left(-A_e^{ff'}(\phi_{Lf}\cdot H_d)\phi_{\overline{E}f'} + A_u^{ff'}(\phi_{Qf}\cdot H_u)\phi_{\overline{U}f'} - A_d^{ff'}(\phi_{Qf}\cdot H_d)\phi_{\overline{D}f'} \right) + h.c. \\ & - B\mu H_u\cdot H_d + h.c. \end{aligned} \tag{2.8}$$

We denote $M_{1,2,3} = M_{B,W,G}$ respectively. The phenomenology of SUSY models are determined by these soft terms.

[2] Here, we assume R-parity conservation.

2.1.2 Spontaneous Electroweak Symmetry Breaking

In the MSSM, two Higgs fields have the vacuum expectation values (vev) after the spontaneous electroweak symmetry breaking. The tree level potential of the Higgs fields $V_H^{\rm tree}$ is obtained from the Lagrangian (2.7) and (2.8),

$$\begin{aligned} V_H^{\rm tree} &= \left(|\mu|^2 + m_{H_u}^2\right)|H_u|^2 + \left(|\mu|^2 + m_{H_d}^2\right)|H_d|^2 + (B\mu H_u \cdot H_d + h.c.) \\ &\quad + \frac{g^2+g'^2}{8}\left(|H_u|^2 - |H_d|^2\right)^2 + \frac{g^2}{2}|H_d^\dagger H_u|^2 \,. \end{aligned} \tag{2.9}$$

Here we assume the charged fields and the colored fields do not have the vev in order not to break the $\mathrm{U}(1)_Y$ and $\mathrm{SU}(3)_C$ symmetries. In addition, since we assume the R-parity is conserved, the sneutrinos also do not have vevs. Then only the Higgs fields have vevs. We can redefine the Higgs fields to satisfy $\langle H_u^+ \rangle = 0$ by using the degree of freedom of $\mathrm{SU}(2)\times\mathrm{U}(1)$ symmetry, and the vev of the Higgs fields can be written as

$$\langle H_u \rangle = \begin{pmatrix} 0 \\ v_u \end{pmatrix} \equiv \begin{pmatrix} 0 \\ v\sin\beta \end{pmatrix}, \quad \langle H_d \rangle = \begin{pmatrix} v_d \\ 0 \end{pmatrix} \equiv \begin{pmatrix} v\cos\beta \\ 0 \end{pmatrix}. \tag{2.10}$$

The Higgs fields have non-zero vev when $H_u^0 = H_d^0 = 0$ is not the minimum,

$$\begin{aligned} &\det \begin{pmatrix} \frac{\partial^2 V_H^{\rm tree}}{\partial (H_u^0)^2} & \frac{\partial^2 V_H^{\rm tree}}{\partial H_u^0 \partial H_d^0} \\ \frac{\partial^2 V_H^{\rm tree}}{\partial H_u^0 \partial H_d^0} & \frac{\partial^2 V_H^{\rm tree}}{\partial (H_d^0)^2} \end{pmatrix}_{H_u = H_d = 0} < 0 \,, \\ &\rightarrow \left(|\mu|^2 + m_{H_u}^2\right)\left(|\mu|^2 + m_{H_d}^2\right) < |B\mu|^2 \,. \end{aligned} \tag{2.11}$$

In this case, $v^2 = \langle H_u \rangle^2 + \langle H_d \rangle^2$ becomes the SM Higgs vacuum expectation value $v \sim 174$ GeV. The condition for the potential minimization can be written as

$$\frac{\partial V_H^{\rm tree}}{\partial H_u^0}\Big|_{\rm vev} = \frac{\partial V_H^{\rm tree}}{\partial H_d^0}\Big|_{\rm vev} = 0 \,. \tag{2.12}$$

From these equations, the following relations among the SUSY parameters can be obtained,

$$|\mu|^2 = -\frac{M_Z^2}{2} + \frac{m_{H_u}^2 \tan^2\beta - m_{H_d}^2}{1 - \tan^2\beta} \,, \tag{2.13}$$

$$B\mu = -\frac{1}{2}\sin 2\beta M_Z^2 + \frac{\tan\beta\left(m_{H_u}^2 - m_{H_d}^2\right)}{1 - \tan^2\beta} \,, \tag{2.14}$$

where $M_Z^2 = \left(g^2 + g'^2\right)v^2/2$ is the mass of the Z boson.

As we see in Sec. 2.1.5, it is important to include the radiative corrections to the Higgs sector when we calculate the SM Higgs boson mass. Since the radiative corrections change Eq. (2.13) and (2.14), we show the contribution here. As an example, we show the one-loop corrections from the top and stops which give the largest contribution to the SM Higgs mass. Including the

one-loop corrections from the tops and stops, the potential of the Higgs fields changes as [53]

$$\begin{aligned} V_H &= V_H^{\rm tree} + V_H^t \,, \qquad (2.15)\\ V_H^t &= \frac{1}{32\pi^2}\left(3\sum_{i=1,2} M_{\tilde{t}_i}^4\left(\ln\frac{M_{\tilde{t}_i}^2}{Q^2}-\frac{3}{2}\right) - 6M_t^4\left(\ln\frac{M_t^2}{Q^2}-\frac{3}{2}\right)\right), \end{aligned}$$

where Q is the renormalization scale and

$$\begin{aligned} M_{\tilde{t}_{1,2}}^2 &= \frac{1}{2}\left(2Y_t^2|H_u^0|^2 + m_{\tilde{t}}^2 + m_{\bar{\tilde{t}}}^2 \mp \sqrt{(m_{\tilde{t}}^2 - m_{\bar{\tilde{t}}}^2)^2 + 4Y_t^2 X_t^2 |H_u^0|^2}\right), \qquad (2.16)\\ M_t &= Y_t H_u^0 \,. \qquad (2.17) \end{aligned}$$

Here, $m_{\tilde{t}}^2 = m_{\tilde{Q}33}^2, m_{\bar{\tilde{t}}}^2 = m_{\bar{\tilde{U}}33}^2, X_t = A_t - \mu\cot\beta, A_t = A_u^{33}$ and we assume that the stops do not mix with the other squarks, e.g. $m_{\tilde{Q}3f}^2 = 0$ for $f \neq 3$ (see also Eq. (2.8)). Including these corrections, the condition for the potential minimization (2.12) changes as $\frac{\partial V_H}{\partial H_u^0}\Big|_{\rm vev} = \frac{\partial V_H}{\partial H_d^0}\Big|_{\rm vev} = 0$ and the following relations are obtained

$$\begin{aligned} |\mu|^2 &= -\frac{M_Z^2}{2} + \frac{m_{H_u}^2\tan^2\beta - m_{H_d}^2}{1-\tan^2\beta} + \frac{\frac{1}{2v_u}\frac{\partial V_H^t}{\partial H_u^0}\Big|_{\rm vev}\tan^2\beta - \frac{1}{2v_d}\frac{\partial V_H^t}{\partial H_d^0}\Big|_{\rm vev}}{1-\tan^2\beta}\,, \qquad (2.18)\\ B\mu &= -\frac{1}{2}\sin 2\beta M_Z^2 + \frac{\tan\beta\left(m_{H_u}^2 - m_{H_d}^2\right)}{1-\tan^2\beta} + \frac{\tan\beta\left(\frac{1}{2v_u}\frac{\partial V_H^t}{\partial H_u^0}\Big|_{\rm vev} - \frac{1}{2v_d}\frac{\partial V_H^t}{\partial H_d^0}\Big|_{\rm vev}\right)}{1-\tan^2\beta}\,. \qquad (2.19) \end{aligned}$$

After the spontaneous symmetry breaking, the SM fermions have the mass. For example, the top quark get the mass $m_t = Y_t v\sin\beta$. In order for the Yukawa coupling Y_t not to blow up in high energy scale, $\tan\beta > 1$ is considered. $\tan\beta = \langle H_u\rangle/\langle H_d\rangle$ is the ratio of the vacuum expectation values of the up- and down-type Higgs and it is the important parameter for the phenomenology.

2.1.3 Hierarchy Problem

Here, we see the cancellation of the quadratic divergence between the SUSY particles and the SM particles.

First, let us see the hierarchy problem [54–57]. In the SM, the Higgs sector is written as

$$L \ni (D^\mu H_{\rm SM})^\dagger (D_\mu H_{\rm SM}) - \mu_{\rm SM}^2 H_{\rm SM}^\dagger H_{\rm SM} - \lambda_{\rm SM}(H_{\rm SM}^\dagger H_{\rm SM})^2 \,, \qquad (2.20)$$

where $H_{\rm SM}$ is the SM Higgs field. Thus the Higgs boson mass m_h^2 at the tree level is given by

$$m_h^2 = -2\mu_{\rm SM}^2 \,. \qquad (2.21)$$

The problem is that quantum corrections for this parameter have the quadratic divergences. For example, the radiative correction from the top loop (Figure 2.1 (a)) is

$$m_h^2 = -2\mu_{\rm SM}^2 - \frac{Y_t^2}{8\pi^2}\Lambda^2 + \mathcal{O}\left(\log(\Lambda^2)\right) \,, \qquad (2.22)$$

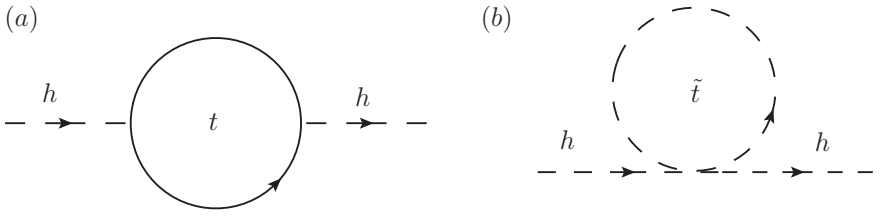

Figure 2.1: An example of the cancellation of the quadratic divergence between the SM particle (a: top) and the SUSY particle (b: stop).

where Λ is a cutoff scale of the SM. If we consider that the SM is valid up to Planck scale ($\mathcal{O}\left(10^{19}\right)$ GeV), the second term of the right hand side of Eq. (2.22) becomes $\mathcal{O}\left(10^{36}\right)$ GeV^2. Since $m_h = 125$ GeV [58], the left hand side of Eq. (2.22) becomes $\mathcal{O}\left(10^4\right)$ GeV^2 and $\mu_{\rm SM}$ should be tuned to satisfy Eq. (2.22). Thus, the unnatural fine tuning with the size of 10^{-32} is needed. This is the hierarchy problem.

In SUSY, the partner particles of the SM particles which give the quadratic divergence cancel out the divergence from the SM particles. Let us see the divergence of the top particle for example. In the MSSM, there are two stops. By the symmetry, the stops' couplings to the Higgs field is proportional to the top's coupling Y_t as shown in Eq. (2.7)

$$L \ni -Y_t H_u^0 \chi_t \chi_{\bar{t}} - Y_t^2 |H_u^0|^2 |\phi_t|^2 - Y_t^2 |H_u^0|^2 |\phi_{\bar{t}}|^2 \,. \tag{2.23}$$

Then, calculating the the contributions from Figure 2.1 (a) and (b), the quadratic divergence is cancelled as [4]

$$m_h^2 = \left(m_h^{\rm tree}\right)^2 - \frac{Y_t^2}{8\pi^2}\Lambda^2 + \frac{Y_t^2}{16\pi^2}\Lambda^2 \times 2 + \mathcal{O}\left(\log(\Lambda^2)\right) \,, \tag{2.24}$$

where the third term comes from the stop contributions. As a result, the problem of the unnatural fine tuning seems to be solved.

On the other hand, the logarithm terms become large when the SUSY particles are heavy $\gg \mathcal{O}(100)$GeV. For example, the logarithm term from the stops in Eq. (2.24) is given as

$$m_h^2 \;\; = \;\; \left(m_h^{\rm tree}\right)^2 - \frac{Y_t^2}{8\pi^2} M_{\tilde{t}}^2 \ln \frac{\Lambda^2}{M_{\tilde{t}}^2} + \cdots \,, \tag{2.25}$$

where $\cdots$ denote the terms which are independent of Λ and the higher loop corrections. Here, we assume that two stops have the same mass $M_{\tilde{t}}$. From this equation, if we consider the very heavy SUSY particles $\gg \mathcal{O}(100)$GeV, the problem of the unnatural fine tuning arises again. Thus, the hierarchy problem is solved when the masses of the SUSY particles are not different so much with the electroweak scale. When the stops are 1 (100) TeV, the logarithm term becomes $\mathcal{O}(10^{6(10)})$ GeV^2 and the size of the tuning becomes $\mathcal{O}(10^{-2(6)})$. In SUSY, although the problem of the unnatural fine tuning (the size of 10^{-32}) is solved, there still remains the little fine tuning (the size of $\mathcal{O}(10^{-2\sim-6})$) when the masses of the SUSY particles are $\mathcal{O}$(1–100) TeV.

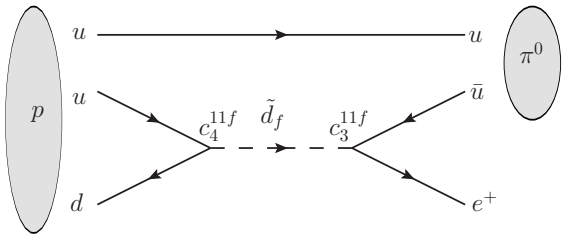

Figure 2.2: An example of the proton decay process is shown. Here, we assume R-parity is violated and there exist non-zero coupling c_3^{11f} and c_4^{11f}.

2.1.4 Dark Matter

In Eq. (2.6), we assume R-parity conservation. R-parity is a discrete symmetry defined as

$$R_p = (-1)^{3B+L+2S}\,, \tag{2.26}$$

where S is a spin and B (L) is the baryon (lepton) number defined in Table. 2.1. With this definition, the SM particles have $R_p = 1$ and the SUSY particles have $R_p = -1$. If R-parity is violated, the following terms can exist in the superpotential [4]

$$W \ni c_1^f H_u \cdot L_f + c_2^{ff'f''} L_f \cdot L_{f'} \overline{E}_{f''} + c_3^{ff'f''} Q_f \cdot L_{f'} \overline{D}_{f''} + c_4^{ff'f''} \epsilon_{\alpha\beta\gamma} \overline{U}_f^{\alpha} \overline{D}_{f'}^{\beta} \overline{D}_{f''}^{\gamma}\,, \tag{2.27}$$

where α, β, γ denote color indices. $c_1 \sim c_3$ terms violate the lepton number and c_4 term violates the baryon number. If both of the lepton number breaking term and the baryon number breaking term exist, the proton can decay. For example, if there exist c_3^{11f} and c_4^{11f}, sdown($\tilde{d}_f$) exchange process for proton decay $p \to e^+\pi^0$ arises (see Figure 2.2). The decay width for this process can be roughly estimated by dimensional analysis as [4]

$$\Gamma(p \to e^+\pi^0) \sim m_p^5 \frac{1}{m_{\tilde{d}f}^4} |c_3^{11f} c_4^{11f}|^2\,. \tag{2.28}$$

When the proton decays only by this process, the lifetime of the proton τ_p becomes as

$$\begin{aligned} \tau_p &= \frac{1}{\Gamma(p \to e^+\pi^0)} \sim \frac{m_{\tilde{d}f}^4}{m_p^5} \frac{1}{|c_3^{11f} c_4^{11f}|^2} \\ &\sim 8.2 \times 10^{33} \text{years} \left(\frac{m_{\tilde{d}f}}{1\text{TeV}}\right)^4 \left(\frac{1.9 \times 10^{-27}}{|c_3^{11f} c_4^{11f}|}\right)^2 \end{aligned} \tag{2.29}$$

From the Super-Kamiokande experiment, the lifetime of the proton is strongly constrained [59]: $\tau_p < 8.2 \times 10^{33}$ years. When there is the above process only and the mass of the sdown $m_{\tilde{d}i}$ is 1 (100) TeV, the constraints become $|c_3^{11f} c_4^{11f}| \lesssim 10^{-27}(10^{-23})$. Thus, one of c_3 or c_4 should be suppressed at least. In order to suppress these terms, we assume R-parity conservation.

When R-parity is conserved, the lightest SUSY particle (LSP) becomes stable since it has $R_p = -1$ and can not decay to the SM particles. Especially, when all scalar SUSY particles (sfermions) are heavy, the lightest neutralino LSP can be a good candidate for the DM. There are four neutralinos in the MSSM and the mass term is written as,

$$L \ni -\frac{1}{2}\left(\chi_B\ \chi_W^3\ \chi_{H_d^0}\ \chi_{H_u^0}\right)\begin{pmatrix} M_1 & 0 & -M_Z s_W c_\beta & M_Z s_W s_\beta \\ 0 & M_2 & M_Z c_W c_\beta & -M_Z c_W s_\beta \\ -M_Z s_W c_\beta & M_Z c_W c_\beta & 0 & -\mu \\ M_Z s_W s_\beta & -M_Z c_W s_\beta & -\mu & 0 \end{pmatrix}\begin{pmatrix} \chi_B \\ \chi_W^3 \\ \chi_{H_d^0} \\ \chi_{H_u^0} \end{pmatrix} + h.c.\,. \tag{2.30}$$

$s_\beta \equiv \sin\beta, c_\beta \equiv \cos\beta$ and $s_W = \sin\theta_W = g'/\sqrt{g^2+g'^2}, c_W = \cos\theta_W$ denote the Weinberg angle.

This 4×4 mass matrix, M_n, can be diagonalized by an orthogonal matrix, O_n, as

$$O_n M_n O_n^T = \begin{pmatrix} \epsilon_1 m_{\chi_1^0} & 0 & 0 & 0 \\ 0 & \epsilon_2 m_{\chi_2^0} & 0 & 0 \\ 0 & 0 & \epsilon_3 m_{\chi_3^0} & 0 \\ 0 & 0 & 0 & \epsilon_4 m_{\chi_4^0} \end{pmatrix}, \quad \begin{pmatrix} \chi_{\chi_1^0} \\ \chi_{\chi_2^0} \\ \chi_{\chi_3^0} \\ \chi_{\chi_4^0} \end{pmatrix} \equiv O_n \begin{pmatrix} \chi_B \\ \chi_W^3 \\ \chi_{H_d^0} \\ \chi_{H_u^0} \end{pmatrix}. \tag{2.31}$$

$\epsilon_i = \pm 1$ and we define as $0 < m_{\chi_1^0} < m_{\chi_2^0} < m_{\chi_3^0} < m_{\chi_4^0}$. The lightest neutralino, χ_1^0, can be a DM candidate. We call the DM model as X-ino DM model when X-ino is the main component of χ_1^0: for example, Bino DM model for $\chi_1^0 \sim \chi_B$ and Bino-Higgsino DM model where χ_1^0 is composed of $\chi_B, \chi_{H_d^0}$ and $\chi_{H_u^0}$.

2.1.5 Higgs Boson Mass

The Higgs boson was discovered at the LHC in July 2012 [1,2]. Its mass has also been determined by combining the results of the ATLAS and the CMS [58]

$$m_h = 125.09 \pm 0.21(\text{stat.}) \pm 0.11(\text{syst.})\text{GeV}\,. \tag{2.32}$$

Here, we briefly review the Higgs boson mass in the MSSM.

After the spontaneous symmetry breaking, the Higgs fields becomes as

$$H_u = \begin{pmatrix} H_u^+ \\ v_u + \frac{1}{\sqrt{2}}(h_u + iA_u) \end{pmatrix}, \quad H_d = \begin{pmatrix} v_d + \frac{1}{\sqrt{2}}(h_d + iA_d) \\ H_d^- \end{pmatrix}, \tag{2.33}$$

where $A_{u,d}$ is the pseudo scalar Higgs, H^+ is the charged Higgs and the $h_{u,d}$ is the neutral Higgs. The mass matrix for the neutral Higgs is calculated from the potential Eq. (2.9) as

$$\begin{aligned} L &\ni -\frac{1}{2}(h_u\ h_d)\begin{pmatrix} |\mu|^2 + m_{H_u}^2 - \frac{1}{2}c_{2\beta}M_Z^2 + s_\beta^2 M_Z^2 & -B\mu - \frac{1}{2}s_{2\beta}M_Z^2 \\ -B\mu - \frac{1}{2}s_{2\beta}M_Z^2 & |\mu|^2 + m_{H_d}^2 + \frac{1}{2}c_{2\beta}M_Z^2 + c_\beta^2 M_Z^2 \end{pmatrix}\begin{pmatrix} h_u \\ h_d \end{pmatrix} \\ &= -\frac{1}{2}(h_u\ h_d)\begin{pmatrix} c_\beta^2 m_A^2 + s_\beta^2 M_Z^2 & -\frac{1}{2}s_{2\beta}(m_A^2 + M_Z^2) \\ -\frac{1}{2}s_{2\beta}(m_A^2 + M_Z^2) & s_\beta^2 m_A^2 + c_\beta^2 M_Z^2 \end{pmatrix}\begin{pmatrix} h_u \\ h_d \end{pmatrix}, \end{aligned} \tag{2.34}$$

where $m_A^2 = 2B\mu/s_{2\beta}$ is the diagonalized mass of the pseudo scalar Higgs and we use the relation Eq. (2.13) and (2.14). We can diagonalize this matrix by the mixing angle α as

$$\begin{pmatrix} h \\ H \end{pmatrix} \equiv \begin{pmatrix} \cos\alpha & -\sin\alpha \\ \sin\alpha & \cos\alpha \end{pmatrix} \begin{pmatrix} h_u \\ h_d \end{pmatrix} , \tag{2.35}$$

$$m_{h,H}^2 = \frac{1}{2}\left(m_A^2 + M_Z^2 \mp \sqrt{\left(m_A^2 - M_Z^2\right)^2 + 4m_A^2 M_Z^2 s_{2\beta}^2} \right) , \tag{2.36}$$

$$\tan 2\alpha = \frac{m_A^2 + M_Z^2}{m_A^2 - M_Z^2} \tan 2\beta \, . \tag{2.37}$$

In the limit $m_A \gg M_Z$, h becomes the SM Higgs boson. Thus, at the tree level, the mass of the Higgs boson is written as

$$\left(m_h^{\text{tree}}\right)^2 = \frac{1}{2}\left(m_A^2 + M_Z^2 - \sqrt{\left(m_A^2 - M_Z^2\right)^2 + 4m_A^2 M_Z^2 s_{2\beta}^2} \right) . \tag{2.38}$$

Note that this value can not exceed the Z boson mass M_Z and $m_h = 125$ GeV can not be explained.

On the other hand, the radiative corrections can raise this Higgs boson mass [6,7]. Including the radiative corrections, $m_h = 125$GeV can be explained in the MSSM. Here, we show the one-loop contributions from the top and stops which give the largest corrections. Including the contribution from the top and stops, the potential of the Higgs fields changes as Eq. (2.15). Then, the mass matrix for the neutral Higgs changes as

$$L \ni -\frac{1}{2}\left(h_u \; h_d\right) M \begin{pmatrix} h_u \\ h_d \end{pmatrix} , \tag{2.39}$$

$$\begin{aligned} M = & \\ & \begin{pmatrix} |\mu|^2 + m_{H_u}^2 - \frac{1}{2}c_{2\beta}M_Z^2 + s_\beta^2 M_Z^2 + \frac{1}{2}\frac{\partial^2 V_H^t}{\partial (H_u^0)^2}\Big|_{\text{vev}} & -B\mu - \frac{1}{2}s_{2\beta}M_Z^2 + \frac{1}{2}\frac{\partial^2 V_H^t}{\partial H_u^0 \partial H_d^0}\Big|_{\text{vev}} \\ -B\mu - \frac{1}{2}s_{2\beta}M_Z^2 + \frac{1}{2}\frac{\partial^2 V_H^t}{\partial H_u^0 \partial H_d^0}\Big|_{\text{vev}} & |\mu|^2 + m_{H_d}^2 + \frac{1}{2}c_{2\beta}M_Z^2 + c_\beta^2 M_Z^2 + \frac{1}{2}\frac{\partial^2 V_H^t}{\partial (H_d^0)^2}\Big|_{\text{vev}} \end{pmatrix} \\ & = \begin{pmatrix} c_\beta^2 m_A^2 + s_\beta^2 M_Z^2 + \frac{1}{2}\frac{\partial^2 V_H^t}{\partial (H_u^0)^2} - \frac{1}{2v_u}\frac{\partial V_H^t}{\partial H_u^0}\Big|_{\text{vev}} & -\frac{1}{2}s_{2\beta}(m_A^2 + M_Z^2) + \frac{1}{2}\frac{\partial^2 V_H^t}{\partial H_u^0 \partial H_d^0}\Big|_{\text{vev}} \\ -\frac{1}{2}s_{2\beta}(m_A^2 + M_Z^2) + \frac{1}{2}\frac{\partial^2 V_H^t}{\partial H_u^0 \partial H_d^0}\Big|_{\text{vev}} & s_\beta^2 m_A^2 + c_\beta^2 M_Z^2 + \frac{1}{2}\frac{\partial^2 V_H^t}{\partial (H_d^0)^2} - \frac{1}{2v_d}\frac{\partial V_H^t}{\partial H_d^0}\Big|_{\text{vev}} \end{pmatrix} . \end{aligned}$$

Here, $m_A^2 = 2B\mu/s_{2\beta}$ with the conditions (2.18) and (2.19). In the case $m_A \gg M_Z$, the mixing angle α does not change compared to the tree level one and the diagonalization is performed as Eq. (2.35). Then the mass of the Higgs boson is calculated as

$$m_h^2 = \left(m_h^{\text{tree}}\right)^2 + \Delta m_h^2 \, , \tag{2.40}$$

$$\begin{aligned} \Delta m_h^2 = & \frac{\cos^2\alpha}{2}\left(\frac{\partial^2 V_H^t}{\partial \left(H_u^0\right)^2}\Big|_{\text{vev}} - \frac{1}{v_u}\frac{\partial V_H^t}{\partial H_u^0}\Big|_{\text{vev}} \right) \\ & + \frac{\sin^2\alpha}{2}\left(\frac{\partial^2 V_H^t}{\partial \left(H_d^0\right)^2}\Big|_{\text{vev}} - \frac{1}{v_d}\frac{\partial V_H^t}{\partial H_d^0}\Big|_{\text{vev}} \right) - \sin\alpha\cos\alpha \frac{\partial^2 V_H^t}{\partial H_u^0 \partial H_d^0}\Big|_{\text{vev}} . \end{aligned}$$

Then substituting Eq. (2.15), the Higgs boson mass becomes as

$$m_h^2 = \left(m_h^{\rm tree}\right)^2 + \frac{3m_t^4}{4\pi^2 v^2}\left(\ln\left(\frac{M_S^2}{m_t^2}\right) + \frac{X_t^2}{M_S^2}\left(1 - \frac{X_t^2}{12M_S^2}\right)\right). \tag{2.41}$$

Here, $M_S^2 = \sqrt{m_{\tilde{t}_1}^2 m_{\tilde{t}_2}^2}$ where $m_{\tilde{t}_i} = M_{\tilde{t}_i}|_{\rm vev}$ is the mass of the stop. In this expression, for example when $M_S \sim 1$ TeV and $X_t = 0$, $m_h = 125$ GeV can be explained.

As we saw, $m_h = 125$ GeV can be explained if we include the radiative corrections. However, there are other contributions from the down type particles and higher loops which can give the negative corrections. Thus, including these contributions are also important. The results with including two-loop level calculation are shown in Ref. [8]. In the High-scale Supersymmetric model where all the SUSY particles have the same mass as the supersymmetry breaking scale and X_t is tuned to give a maximal contribution, the result is shown in the left of Figure 2.3. The result of the Split Supersymmetric model is shown in the right of Figure 2.3 where the fermonic SUSY particles are assumed to be relatively light $M_1 = m_t = M_2/2 = \mu/2 = M_3/6.4$ and the other SUSY particles have the same mass as the supersymmetry breaking scale. Although the mass of the Higgs boson depends on the spectra of the SUSY particles and the A-terms, typically the SUSY breaking scale are needed to be $\mathcal{O}(2\text{–}10^7)$ TeV to explain the Higgs boson mass 125 GeV. Thus, in the MSSM, sfermions, especially stops, are supposed to be heavier than $1 \sim 10$ TeV.

2.1.6 LHC Searches

The LHC is the proton-proton collider and searching new physical signals. The discovery of the Higgs boson is the prominent result. In addition, the SUSY particles have been searched at the LHC. However, there is no signal of the SUSY particles yet. Thus, the mass spectra of them are constrained. Here, we briefly review these constraints.

At the LHC, there are experiments called as the ATLAS and the CMS. Since they give the similar results, we review results of the ATLAS here. The LHC had run from 2010 to 2011 at $\sqrt{s} = 7$ TeV and in 2012 at $\sqrt{s} = 8$ TeV. The ATLAS recorded the integrated luminosity 4.7 fb^{-1} at 7 TeV and 20.3 fb^{-1} at 8 TeV. For the preparation to run in the high energy, the LHC had stopped during 2013 to 2014. And now, in 2015, the run at 13 TeV is starting.

The SUSY particles, especially colored particles, are the main targets at the LHC. This is because the LHC is the proton-proton collider and the production cross sections of the colored particles are large. Especially, the gluino and the squarks are easily produced at the LHC with the processes like $pp \to \tilde{g}\tilde{g}$ or $pp \to \tilde{q}\tilde{q}$ and so on where $\tilde{g}, \tilde{q}$ denotes gluino and squark respectively. The produced gluinos and squarks decay to the SM particles and the DMs since the gluino and squarks have odd R-parity and the final state should also contain odd R-parity lightest particle, i.e. the LSP. Since the gluino/squark decay produces many quarks and the DMs, the typical signal is composed of many jets, a few leptons and the missing energy. This is because the light quark is observed as a jet, the top quark can decay to leptons via the W

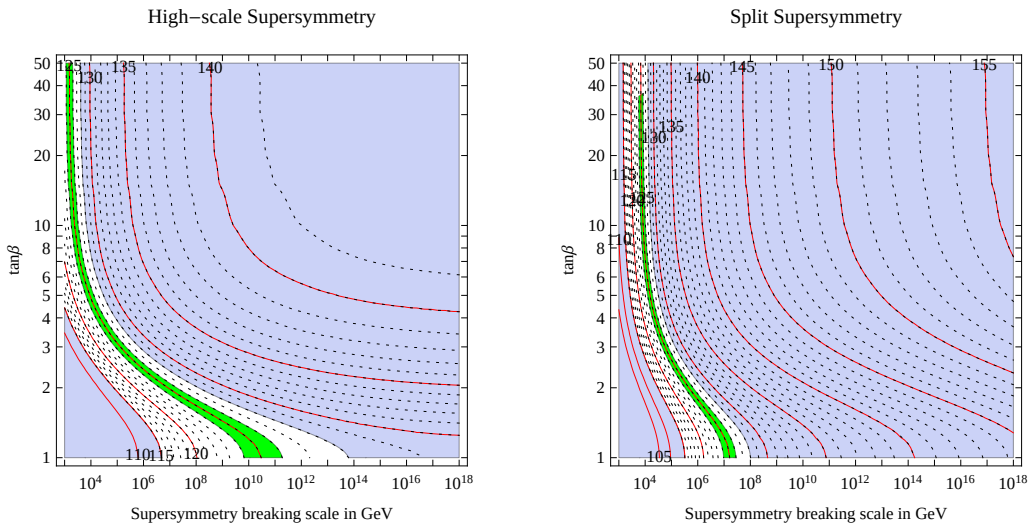

Figure 2.3: The contours of the Higgs boson mass is shown. These are the results of Ref. [8]. (left) The result of the High-scale Supersymmetric model where all the SUSY particles have the same mass as the supersymmetry breaking scale and X_t is tuned to give a maximal contribution. (right) The result of the Split Supersymmetric model where the fermonic SUSY particles are relatively light $M_1 = m_t = M_2/2 = \mu/2 = M_3/6.4$ and the other SUSY particles have the same mass as the supersymmetry breaking scale. The green shaded region denote 124 GeV$< m_h <$126 GeV.

boson and the DM which can not be detected is observed as missing energy. Thus, multi-jets plus missing energy processes including a few (or zero) leptons have been searched.

Since no significant excess of number of events is discovered, the mass spectra of the gluino and the squarks are constrained. Although the constraints depend on the mass spectra, here we show some results of simple model in Figure 2.4. The left upper figure and the lower figures are the results in Ref. [5] and the right upper figure is the result in Ref. [60]. First, let us see the result for the mSUGRA/CMSSM model (the left upper figure of Figure 2.4). In this model, the soft terms are determined only by four parameters: the universal sfermion mass m_0, the universal gaugino mass $m_{1/2}$, the universal A-term A_0 and the sign of μ. In addition, $\tan\beta$ is also the parameter. These masses and A-terms are assumed to be same for all sfermions (gauginos) at the grand unified theory scale $\sim 10^{16}$ GeV. At the low energy $\sim$ 1TeV, these values of each SUSY

particle become different since the dependence of the Yukawa couplings or the gauge couplings and their radiative effects are different for each SUSY particle. Especially, the stops tends to be lighter than the other squarks and the gaugino masses become as $M_1 : M_2 : M_3 \simeq 1 : 2 : 7$. With these mass spectra, the constraints are obtained as the left upper figure of Figure 2.4. In this case, the constraints become $m_{\tilde{g}} \gtrsim 1.4$ TeV and $m_{\tilde{q}} \gtrsim 1.6$ TeV.

Next, let us see the result of the simplified model. The left lower figure shows the constraints on the mass of the gluino when the squarks are heavy enough and the gluino decay to the top pairs and the DM via virtual stop. The constraint becomes $m_{\tilde{g}} \gtrsim 1.4$ TeV when the DM is relatively light $m_{\chi_1^0} \sim \mathcal{O}(100)$ GeV. The right lower figure shows the constraints on the masses of the first and second generation squarks when the gluino is heavy enough. The constraint becomes $m_{\tilde{q}} \gtrsim 0.9$ TeV when $m_{\chi_1^0} \sim \mathcal{O}(100)$ GeV. The right upper figure shows the constraints on the mass of the stop in Ref. [60]. This is the case when the gluino is heavy enough and the constraint becomes $m_{\tilde{t}} \gtrsim 0.7$ TeV when $m_{\chi_1^0} \sim \mathcal{O}(10)$ GeV.

Although the results change by the mass spectrum, the light SUSY particles with the mass $\mathcal{O}(100)$ GeV are constrained now. The productions of the neutralinos/charginos are also searched at the LHC. We review this in Sec. 3.4.2.

2.1.7 Flavor Changing Neutral Current

In the MSSM, if no symmetries are assumed in the soft terms, there can be sizable off-diagonal soft mass terms, i.e. $m^2_{\tilde{P}ff'}, A_p^{ff'}$ with $f \neq f'$. These terms results flavor changing neutral current (FCNC) process. However, no FCNC process for the SM leptons are observed and constraints are set by experiments. Especially, the MEG experiment sets strongest bound on the branching ratio of the process $\mu \to e\gamma$: $\mathrm{Br}(\mu \to e\gamma) < 5.7 \times 10^{-13}$ [61].

In the MSSM, the diagrams shown in Figure 2.5 contribute to the process $\mu \to e\gamma$ if there exists non-zero value of $m^2_{\tilde{l}ff'}, m^2_{\tilde{\bar{e}}ff'}$. The effective Lagrangian related to this process can be written as

$$L \ni \frac{1}{2} e m_\mu \bar{\psi}_\mu \sigma_{\mu\nu} \left(A^L P_L + A^R P_R \right) \psi_e F^{\mu\nu} + h.c.\,. \tag{2.42}$$

From this Lagrangian, the decay width for $\mu \to e\gamma$ can be calculated as

$$\Gamma(\mu \to e\gamma) = \frac{e^2}{16\pi} m_\mu^5 \left(|A^L|^2 + |A^R|^2 \right) . \tag{2.43}$$

A^L, A^R are calculated from the diagrams in Figure 2.5. Although the detailed calculations are given in Ref. [62], here we show a simple example case to estimate the constraints. For example, let us consider the loop contribution from the Wino-slepton loop assuming that there exist non-zero value of $m^2_{\tilde{l}12}$ and other off-diagonal terms are zero. In this case, only A^L becomes non-zero and can be estimated by mass insertion approximation as [18]

$$A^L = -\frac{g^2}{128\pi^2} \frac{\delta_{\tilde{l}12}}{m^2_{\tilde{l}}} , \tag{2.44}$$

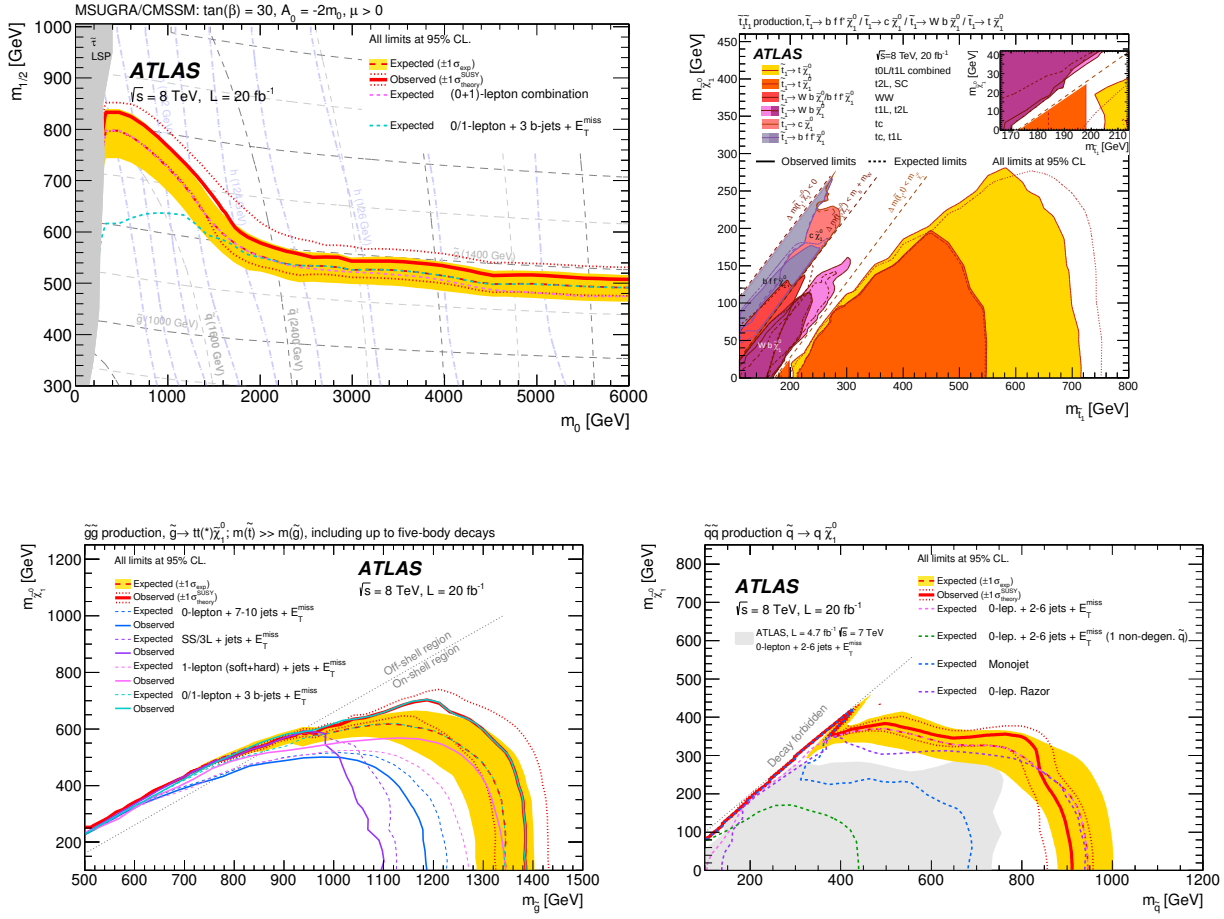

Figure 2.4: The current constraints for the gluino and the squarks are shown. The left upper figure and the lower figures are the results in Ref. [5]. The right upper figure is the results in Ref. [60]. See text for details.

where $\delta_{\tilde{l}12} = (m^2_{\tilde{l}12} - m^2_{\tilde{l}})/m^2_{\tilde{l}}$ and we assume $m^2_{\tilde{l}} = m^2_{\tilde{l}11} = m^2_{\tilde{l}22}$ and $M_2 \sim |\mu| \ll m_{\tilde{l}}$. Then the branching ratio $\mathrm{Br}(\mu \to e\gamma)$ becomes as

$$\begin{aligned} \mathrm{Br}(\mu \to e\gamma) &= \frac{\Gamma(\mu \to e\gamma)}{\Gamma_\mu} \\ &\sim \frac{1}{\Gamma_\mu}\frac{e^2}{16\pi} m_\mu^5 \left(\frac{g^2 \delta_{\tilde{l}12}}{128\pi^2 m^2_{\tilde{l}}}\right)^2 \qquad (2.45) \\ &\sim 5.7 \times 10^{-13} \times \left(\frac{\delta_{\tilde{l}12}}{0.3}\right)^2 \left(\frac{6\ \mathrm{TeV}}{m_{\tilde{l}}}\right)^4, \qquad (2.46) \end{aligned}$$

where Γ_μ is the total decay width of μ and $\Gamma_\mu = 2.99 \times 10^{-19}$ GeV [63]. Thus, to evade the MEG constraints, $m_{\tilde{l}} \gtrsim 6$ TeV is needed for $\delta_{\tilde{l}12} = 0.3$.

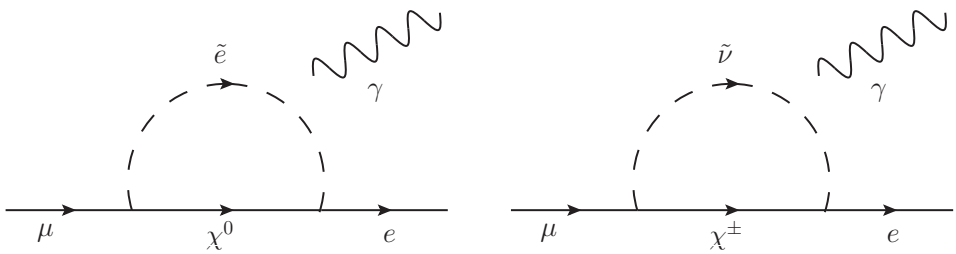

Figure 2.5: The diagrams which contribute to the $\mu \to e\gamma$ process are shown.

The calculations for the heavy sfermion models are performed in Ref. [17,18] (see Figure 2.6). In Ref. [17] (left figure of Figure 2.6), two models, the heavy gaugino model and the AMSB model, are considered with $\mu = m_{\tilde{l}}, \tan\beta = 50, \delta_{\tilde{l}12} = \delta_{\tilde{e}12} = 0.1$ where $\delta_{\tilde{e}12} = (m^2_{\tilde{e}12} - m^2_{\tilde{e}})/m^2_{\tilde{e}}$ and other off-diagonal terms are zero. In the heavy gaugino model, the masses of the gauginos are assumed as $M_3 = m_{\tilde{l}}$ with the GUT relation $\frac{3}{5}\frac{M_1}{g'^2} = \frac{M_2}{g^2} = \frac{M_3}{g_s^2}$. In the AMSB model, the masses of the gauginos are assumed as $M_i = -\frac{b_i g_i^2}{16\pi^2} m_{3/2}$ where $b_i = (-11, -1, 3)$ and $m_{3/2} = 5m_{\tilde{l}}$. The right figure of Figure 2.6 is the result of Ref. [18] with assuming $M_1 = M_2 = |\mu|$, $\tan\beta = 5$ and all relevant off-diagonal terms sizable $\delta_{\tilde{P}ff'} = 0.3$. Although the constraints change by the mass spectra of the gauginos and the Higgsinos, typically $m_{\tilde{l}} \gtrsim \mathcal{O}(10)$ TeV is needed for sizable off-diagonal soft term $\delta_{\tilde{P}}ff' \sim \mathcal{O}(0.1)$.

2.2 Heavy Sfermion Models

As shown in Sec. 2.1.5, to explain the Higgs boson mass 125 GeV in the MSSM, the SUSY breaking scale is needed to be higher than ∼1 TeV. Especially, when the SUSY breaking scale is larger than $\mathcal{O}$(1–10)TeV, not only the Higgs boson mass can be explained but also the constraints from the LHC can be evaded (Sec. 2.1.6). In addition, the constraints from the FCNC problem are also relaxed (Sec. 2.1.7). Thus, the high scale SUSY models, especially the heavy sfermion models, are one of the attractive SUSY models and have attracted attentions. Here, we review the heavy sfermion scenario (Sec. 2.2.1).

In the SUSY models, the lightest neutralino can be a candidate for the DM . However, in the heavy sfermion scenario, the correct thermal relic abundance can be obtained only in limited cases (Sec. 2.2.2): pure Wino DM with the mass about 3 TeV [20, 21] (Sec. 2.2.3), (almost) pure Higgsino DM with the mass about 1 TeV [21, 22] (Sec. 2.2.4), gaugino coannihilation scenario [23–27] (Sec. 2.2.5) and Bino-Higgsino DM [28–36] (Sec. 2.2.6).

Although the heavy sfermion model is one of the attractive SUSY models, the sfermions are heavy and it is difficult to search them directly by the experiments. Thus the studies about the neutralinos/charginos, especially the DM, become necessarily. Among the DM models, the Bino-Higgsino resonant DM model gives variety of phenomena in the energy scale 10∼1000 GeV. It is important to study such phenomenology combining the possible experiments. In this thesis,

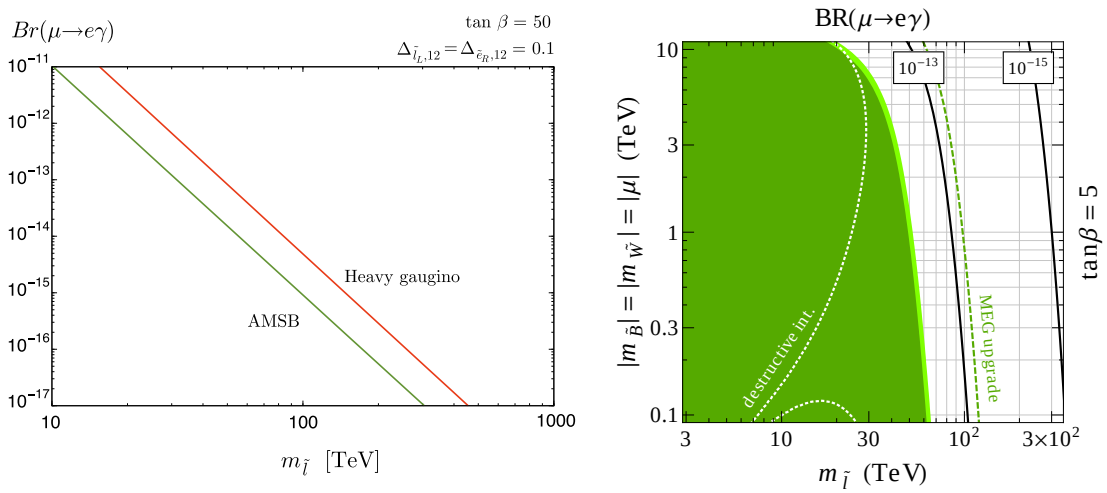

Figure 2.6: The example of the constraints from $\mu \to e\gamma$ are shown. The left figure is the result of Ref. [17] with $\mu = m_{\tilde{l}}, \tan\beta = 50, \delta_{\tilde{l}12} = \delta_{\tilde{e}12} = 0.1$ where $\delta_{\tilde{e}12} = (m^2_{\tilde{e}12} - m^2_{\tilde{e}})/m^2_{\tilde{e}}$ and other off-diagonal terms are zero. The red line is the result of the heavy gaugino model assuming $M_3 = m_{\tilde{l}}$ with the GUT relation $\frac{3}{5}\frac{M_1}{g'^2} = \frac{M_2}{g^2} = \frac{M_3}{g_s^2}$. The green line is the result of the AMSB model assuming $M_i = -\frac{b_i g_i^2}{16\pi^2} m_{3/2}$ where $b_i = (-11, -1, 3)$ and $m_{3/2} = 5m_{\tilde{l}}$. The right figure is the result of Ref. [18] with assuming $M_1 = M_2 = |\mu|$, $\tan\beta = 5$ and all relevant off-diagonal terms $\delta_{\tilde{P}ff'} = 0.3$.

we investigate the Bino-Higgsino resonant DM comprehensively (Sec. 2.2.6).

2.2.1 Heavy Sfermion Scenarios

As written above, the SUSY model with the SUSY breaking scale larger than $\mathcal{O}$(1–10)TeV is one of the attractive models since it can explain the Higgs boson mass, it is compatible with the LHC results and it can evade the FCNC problem. In this case, the sfermions are heavy as the SUSY breaking scale. On the other hand, the gauginos are suggested to be relatively light when the DM is the thermal relic DM. Thus, there have been studies to explain the gap between the size of the soft terms for the sfermion masses and for the gauging masses (for example there are Refs. [9–16]).

In the heavy sfermion scenarios, typically the soft terms for the sfermion masses are given in the tree level while the soft terms for the gaugino masses are given in the one loop level. It occurs when the SUSY breaking fields are charged under some global symmetries. Since the representation of the SUSY breaking fields and the shapes of the couplings are different in each model, the mass spectra are a little bit different in these scenarios. For example, in the split SUSY [9–11], the sfermions are very heavy $\gg \mathcal{O}(10)$ TeV while the Bino, the Wino and the Higgsino are within $\mathcal{O}$(0.1–1) TeV and each neutralino can be a candidate for the DM. In the spread SUSY [12, 13], the mass spectra of the gauginos and Higgsinos become wider than the

split SUSY and the candidates for the DM is the Wino or the Higgsino. In the pure gravity mediation model [14–16], the sfemions are heavy $\mathcal{O}$(10–1000) TeV and the gauginos are $\mathcal{O}(1)$ TeV. The Wino is the LSP and can be a candidate for the DM.

Although there are many studies to explain the size of the soft terms, we concentrate on the phenomenology of the DM and we assume the low energy effective Lagrangian as shown in Sec. 4.

2.2.2 DM in Heavy Sfermion Scenarios

In the heavy sfermion scenarios, the lightest neutralino LSP can be a candidate for the DM. However, the correct thermal relic abundance can be obtained only in limited cases. There are cases where the dominant component of the DM is the Wino, the Higgsino and the Bino. In the Wino DM case, the thermal relic abundance can be explained with the mass about 3 TeV [20, 21]. The Higgsino DM is also the candidate of the thermal relic DM when the mass is about 1 TeV [21, 22]. We show these models in Sec. 2.2.3 and 2.2.4. On the other hand, when the dominant component of the DM is the Bino and there is almost no contribution from the Wino and the Higgsino, the DM is typically overabundant. In this case, the Bino DM should coannihilate with the gauginos [23–27] or the mixing with the Higgsino should be increased [28–36]. The former case, gaugino coannihilation model, is reviewed in Sec. 2.2.5. The latter case, the Bino-Higgsino model is also discussed in Sec. 2.2.6.

2.2.3 Pure Wino DM

In the Wino DM case, the DM can annihilate to the SM particles effectively since the Wino couples to the gauge bosons. When the mass of the Wino is $\mathcal{O}(100)$ GeV, the annihilation cross section becomes larger than $\sim 10^{-26}\mathrm{cm}^3\mathrm{s}^{-1}$ and it makes the relic abundance to be too small compared to the current value (see also Sec. 3.1). The annihilation cross section decreases as the mass increases. Thus, the heavier the Wino become, the larger the relic abundance become. When the mass of the Wino become ~ 3 TeV, the relic abundance can be explained [20, 21].

When the soft masses of the gauginos are given by the one loop level supergravity effects which are called as the anomaly mediated gaugino masses, the Wino tends to become the LSP [64, 65]. In this case, the charged Wino is nearly degenerated with the lightest neutral Wino. Thus, the coannihilations among the charged Wino and the neutral Wino contribute to the annihilation cross section. In addition, the non-perturbative effects called as the Sommerfeld enhancement give the large contribution to the annihilation cross section [20, 21]. This occurs because the nearly degenerated Winos attract each other. Including these effects, the mass of the Wino in order to explain the current relic abundance becomes ~ 3 TeV [20, 21].

Although this model contains about 3 TeV Winos and other heavier $\gtrsim \mathcal{O}(10)$ TeV SUSY particles, the LHC can probe this model with searching the disappearing track of the chargino decay [66–68]. With the indirect detections, for example detection of cosmic rays such as photons, anti-protons and positrons, this model also can be probed [69–74]

2.2.4 (Almost) Pure Higgsino DM

The (almost) pure Higgsino DM case is similar to the pure Wino DM case. The Higgsino couples to the gauge bosons and its annihilation cross section is larger than $\sim 10^{-26}\mathrm{cm}^3\mathrm{s}^{-1}$ when the mass is $\mathcal{O}(100)$ GeV. Thus, the relic abundance is typically small for $\mathcal{O}(100)$ GeV Higgsino and the mass of the Higgsino ~ 1 TeV is necessary [21, 22].

There are the charged Higgsino and two neutral Higgsinos in this model. Since the Higgsino mix with the gauginos, the masses of the two neutral Higgsinos are different. Thus, in this model, the two neutral Higgsinos form the two Majorana neutralinos and the lightest one becomes the Majorana DM. The mass difference between the two Majorana neutralinos decreases as the mixing with the gauginos decreases. When the Bino and the Wino become heavier than $\sim 10^8$ GeV, the mass differences becomes small $\sim 10^{-4}$ GeV and it is constrained from the inelastic scattering with the nucleus [22]. Thus, the mixing between the Higgsinos and the Bino/Wino can not become too small and we call this model as (almost) pure Higgsino DM model.

In this model, it is different from the pure Wino case that there is small Sommerfeld enhancement in the annihilation cross section since the Higgsino forms SU(2) doublets while the Wino forms SU(2) triplet [20, 21]. Since the mass splitting of the chargino and the neutralino is not small enough, there are no disappearing track in the LHC which is different form the pure Wino case: in pure Wino case the mass differences between the chargino and the LSP is ∼160 MeV and the chargino travels $\mathcal{O}$(1–10) cm before decay [67], in (almost) pure Higgsino case the mass differences is ~ 350 MeV and the chargino travels $\lesssim$ 1cm [22]. Thus the LHC can not search this model easily. However, since the two neutral Higgsinos are nearly degenerated, this model is sensitive to the inelastic scattering with the nucleus [22].

2.2.5 Gaugino Coannihilation

When the gauginos are nearly degenerated, the coannihilation can occur [23–27]. The coannihilation is the process that the DM and the gaugino which is slightly heavier than the DM annihilate to the SM particles: i.e. the process like DM $\chi_2^0 \to$ SM SM where χ_2^0 is the nearly degenerated gaugino. In this case, these particles freeze out at approximately the same temperature and the coannihilation process decreases the DM number density. Thus, even the Bino DM which does not mix with the Higgsino sufficiently can explain the current relic abundance. The Bino-Wino coannihilation and the Bino-Gluino coannihilation can give the proper relic abundance when their masses are $\mathcal{O}$(0.1–1) TeV. In these cases, the Higgsinos are considered to be heavy and there is no DM scattering with the nucleus. However, since the gauginos are within the reach of the LHC, this model can be probed by the LHC experiments [75–77].

2.2.6 Bino-Higgsino DM

When the dominant component of the DM is the Bino and the all sfermions are heavy enough, this pure Bino DM can not explain the current thermal relic abundance. This is because ob-

viously the pure Bino does not couple to any other particles sufficiently in this case. There is almost no annihilation cross section and the freeze out occurs at the early time. It results in an overabundant DM (See also Sec. 3.1). Thus, to explain the current relic abundance, the pure Bino should coannihilate with other gauginos or mix with the Higgsinos sizably to increase the annihilation cross section. The gaugino coannihilation case is shown in Sec. 2.2.5. Here we consider the latter case that the Bino mixes with the Higgsino sufficiently.

The Bino-Higgsino DM is one of the good candidates for the DM. To enhance the annihilation cross section, there are two mechanisms: (i) enhance the couplings and include coannihilations with tunings, or (ii) enhance the cross section by resonant annihilation. The former type (i) is called well-tempered model [28–30]. In this model, the Bino and the Higgsino are tuned to be nearly degenerated, $m_{\chi_1^0} \sim m_{\chi_2^0} \sim m_{\chi_3^0} \sim m_{\chi_1^\pm}$. This tuning gives maximal mixing of the Bino and the Higgsino and the DM's couplings to the SM particles become large. In addition, with nearly degenerated neutralinos and charginos, new processes contribute to increase the DM annihilation cross section: for example, the process DM DM$\to W^+W^-$ with t-channel chargino exchange and the coannihilation process DM $\chi_2^0 \to$ SM SM are added. From these two effects, the DM annihilation cross section becomes large enough to explain the current relic abundance. Although the current relic abundance can be explained in the wide range of the parameter space 100 GeV$\lesssim |\mu| \lesssim$ 1000 GeV with $M_1 \sim |\mu|$, almost all regions except for the blind spot where the DM-Higgs coupling vanishes are already excluded by the DM direct searches [38, 39].

On the other hand, in the latter case (ii), the DM annihilation cross section is enhanced by the resonant annihilation. Since the Bino mixes with the Higgsino slightly, the Bino can annihilate to SM particles especially via the Higgs boson or the Z bosons. When the mass of the DM is about half of the particle X which the DM couples, the cross section of the process DM DM $\to X \to$ SM SM is enhanced. The candidates for the resonant particle are the Higgs boson and the Z boson when all other SUSY particles are heavy [30–36]. The allowed mass range is $m_{\chi_1^0} \sim M_1 \sim m_h/2$ or $M_Z/2$ while μ can change in wider range (100 GeV$\lesssim |\mu| \lesssim$2500 GeV).

Since the mass of the DM is $\mathcal{O}(10)$ GeV and the masses of the heavier neutralinos and charginos are $\mathcal{O}(100)$ GeV, this model gives a variety of phenomena in the experiments. Especially, when all the sfermions are heavy, the light neutralinos and charginos are one of the clues to reveal the SUSY models. As shown in Sec. 3, the direct detections have good sensitivity in this mass range, the invisible decay can occur and the LHC can search these particles. Combining these experiments, we can extract information about the new particles and identify the model. Thus, it is very important to investigate the light DM model in the heavy sfermion scenario now. The light DM is the special property of the Bino-Higgsino resonant model. To prepare for the discovery or the exclusion by the experiments and to give the insight to new experiments, we investigate this Bino-Higgsino model with resonant annihilation comprehensively in this thesis.

In this thesis, we investigate essentially the whole parameter space while the previous works [32–36] has done only the scatter plots. With this analysis, the existence of the blind

spot becomes clear, and the importance of investigating the blind spot region is emphasized (see Chapter 4, 5 and 6). In addition, we comprehensively study the phenomenology including the direct detection, the invisible decays and the LHC searches. The study for the SI cross section is performed in all papers [32–36]. However, the study for the SD cross section is partially done only in Ref. [36] and the Higgs boson invisible decay is also only commented in Ref. [33]. Although the LHC search with 8 TeV analysis is investigated in Ref. [34–36], the 14 TeV prospects are discussed with their original analysis only up to $m_{\chi_2^0} < 320$ GeV in Ref. [34]. Furthermore, none of the previous studies have analyzed the 14 TeV LHC prospects of the current model by using the results of the LHC [51]. We investigate all these phenomenology and show the importance of combining these experiments. The detailed description of this model is given in Chapter 4.

Chapter 3

Dark Matter

The dark matter (DM) is one of the clue to the new physics since the SM does not contain a candidate for the DM. Especially, weakly interacting massive particles (WIMPs) are good candidates for the DM. In order to search the DM, there are many experiments. Here we briefly review the phenomenology of the DM, especially the Majorana DM.

First, we see about the thermal relic abundance in Sec. 3.1. In Sec. 3.2, the current status of the direct detections for the spin independent scattering and the spin dependent scattering are discussed. Sec. 3.3 is written about the invisible decay of the Higgs boson and the Z boson. The collider searches for the DM is also discussed in Sec. 3.4. Finally, we take a glance at the indirect searches in Sec. 3.5.

3.1 Thermal Relic Abundance

Here, we briefly show the calculation of the thermal relic abundance [78, 79]. At the early stage of the Universe, the DM is thermalized. Then the number density of the DM evolves by the expansion of the Universe and the balance of the creation and annihilation. When the temperature is higher than the mass of the DM, the DM is in thermal equilibrium. However, as the temperature decreases, the number density deviates from the equilibrium number density. Then the yield which is the ratio of the number density of the DM and the entropy density becomes constant. It is called as freeze out (see Figure 3.1). Finally, the DM remains until today. The current DM relic abundance is observed as Ωh^2 =0.120 by the Planck [19].

Next, we show the calculation of the thermal relic abundance. The thermal relic abundance of the DM is calculated by solving the Boltzmann equation [78]

$$\frac{1}{a^3}\frac{d\left(a^3 n\right)}{dt} = \frac{dn}{dt} + 3Hn = \langle\sigma v\rangle(n_{\rm eq}^2 - n^2)\,, \tag{3.1}$$

where n is the DM number density, a is the cosmological scale factor and t is the cosmic time. Here, $H = a^{-1}da/dt = \sqrt{8\pi G\rho/3}$ is the Hubble parameter with the gravitational constant G

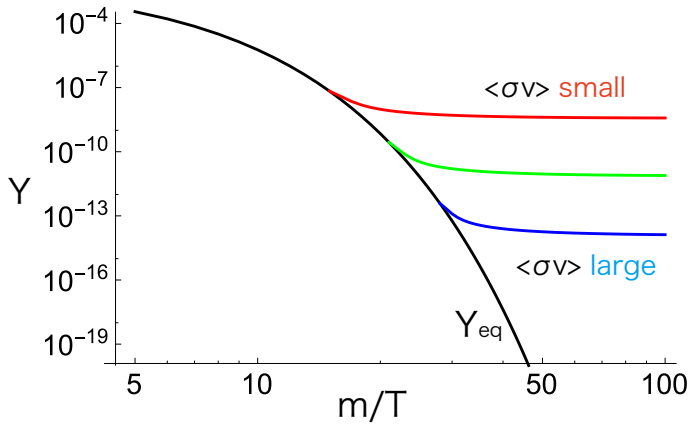

Figure 3.1: The evolution of the DM abundance is shown in $(m/T, Y)$-plane. The black line denotes the equilibrium yield $Y_{\rm eq}$. The red, green and blue lines show the yield with changing the value of $\langle\sigma v\rangle$.

and the total energy density $\rho = \pi^2 g_\rho T^4/30$. T denotes the temperature which is related to t by

$$\frac{dt}{dT} = -\frac{1}{HT}\left(1 + \frac{1}{3}\frac{d(\ln g_s)}{d(\ln T)}\right) . \tag{3.2}$$

Here, parameters g_s and g_ρ are the relativistic degrees of freedom associated to the entropy density and the energy density respectively. As shown in Eq. (3.1), the evolution of the DM number is determined by the Hubble expansion and the balance on the equilibrium number density $n_{\rm eq}$ with the thermally averaged annihilation cross section $\langle\sigma v\rangle$. With the modified Bessel functions of the first and second kind $K_{1,2}$, $n_{\rm eq}$ and $\langle\sigma v\rangle$ are written as [79]

$$n_{\rm eq} = g_\chi \frac{m^2 T}{2\pi^2} K_2(m/T) \tag{3.3}$$

$$\begin{aligned}\langle\sigma v\rangle(T) &= \frac{\int d^3p_1 d^3p_2\ e^{-E_1/T} e^{-E_2/T} \sigma v}{\int d^3p_1 d^3p_2\ e^{-E_1/T} e^{-E_2/T}} \\ &= \frac{1}{8m^4 T\left(K_2(m/T)\right)^2} \int_{4m^2}^{\infty} \sigma(s)\sqrt{s}(s-4m^2) K_1(\sqrt{s}/T) ds\,.\end{aligned} \tag{3.4}$$

where m is the DM mass and $g_\chi = 2$ for the Majorana DM. $\sigma(s)$ is the annihilation cross section of the DM and it depends on the model. The Boltzmann equation is rewritten by using $Y = n/s$ with the entropy density $s = 2\pi^2 g_s T^3/45$,

$$\frac{dY}{dt} = s\langle\sigma v\rangle(Y_{\rm eq}^2 - Y^2)\,. \tag{3.5}$$

Let us see the behavior of the Boltzmann equation (3.1) (see also Figure 3.1). At the early epoch $T \gg m$, $H \ll \langle\sigma v\rangle n_{\rm eq}$ is satisfied and Eq. (3.1) becomes $\frac{dn}{dt} \sim \langle\sigma v\rangle(n_{\rm eq}^2 - n^2)$. In this time, the DM is in the equilibrium $n \sim n_{\rm eq}$ and the number density decreases by $n \propto T^3$. After the temperature decreases $T \lesssim m$, the equilibrium number density decreases exponentially

$n_{\rm eq} \propto \exp(-m/T)$. Then near $T \sim m/20$, the production of the DMs becomes suppressed and Eq. (3.1) becomes $\frac{dn}{dt} \sim -3Hn - \langle\sigma v\rangle n^2$. As the number density obeys this equation, it decreases differently from the equilibrium number density, $n_{\rm eq}$. After the number density decreases further, the annihilation of the DMs becomes also suppressed. Finally, when $T \ll m$, Eq. (3.1) becomes $\frac{dn}{dt} \sim -3Hn$ and the number density evolves only by the Hubble expansion. At this stage $Y = n/s$ becomes constant and the DM remains until today. This is the freeze out. The relic abundance Ω is given by

$$\Omega = \frac{ms(T_0)Y(T_0)}{\rho_{\rm crit}}, \quad \rho_{\rm crit} = \rho(T_0) = \frac{3H^2(T_0)}{8\pi G}\,, \tag{3.6}$$

where T_0 is the current temperature of the Universe. The relic abundance is determined by the mass of the DM, m, and the annihilation cross section of the DM, σ. As shown in Figure 3.1, the small value of $\langle\sigma v\rangle$ tends to make the DM abundance large and the large value tends to make the DM abundance small.

As we can see from Figure 3.1, the size of the annihilation cross section σ or $\langle\sigma v\rangle$ is important to explain the current relic abundance value. With too small annihilation cross section, the DM can not annihilate to the SM particles enough and it becomes overabundant. On the other hand, with too large annihilation cross section, the DM tends to annihilate more than necessary and it does not remain enough. If the annihilation cross section is constant, it is needed to be $\sim 3 \times 10^{-26}{\rm cm}^3{\rm s}^{-1}$ to explain the current DM abundance.

3.2 Direct Detection

The DM has been searched by direct detection experiments. Especially, the LUX [40] and the XENON [41–43] have high sensitivity in the vast region of the DM mass, $m_{\rm DM} = \mathcal{O}(1\text{–}10^4)$ GeV. In these experiments, the nuclei (xenon) can be scattered by the DM if the interaction between the DM and the nuclei exists. They see the recoil energy of the nuclei. However, there is no signal of the DM yet, and they give constraints. Here we briefly show the current status and the future sensitivity for the spin-independent (SI) cross section of the DM (Sec. 3.2.1) and the spin-dependent (SD) cross section of the DM (Sec. 3.2.2).

3.2.1 Spin Independent Scattering

The spin independent (SI) scattering cross section is determined by the coupling between the nucleon and the DM. When the DM is a Majorana fermion, the effective coupling is given as $L \ni \sum_{N=p,n} \lambda_N \overline{\psi}_{\rm DM}\psi_{\rm DM}\overline{N}N$. [1] With this coupling, the SI cross section can be calculated as

$$\sigma_N^{\rm SI} = \frac{4}{\pi}\lambda_N^2 \frac{m_N^2 m_{\rm DM}^2}{(m_{\rm DM}+m_N)^2}\,, \tag{3.7}$$

[1] Note that the term as $\overline{\psi}_{\rm DM}\gamma_\mu\psi_{\rm DM}$ vanishes for the Majorana fermion DM.

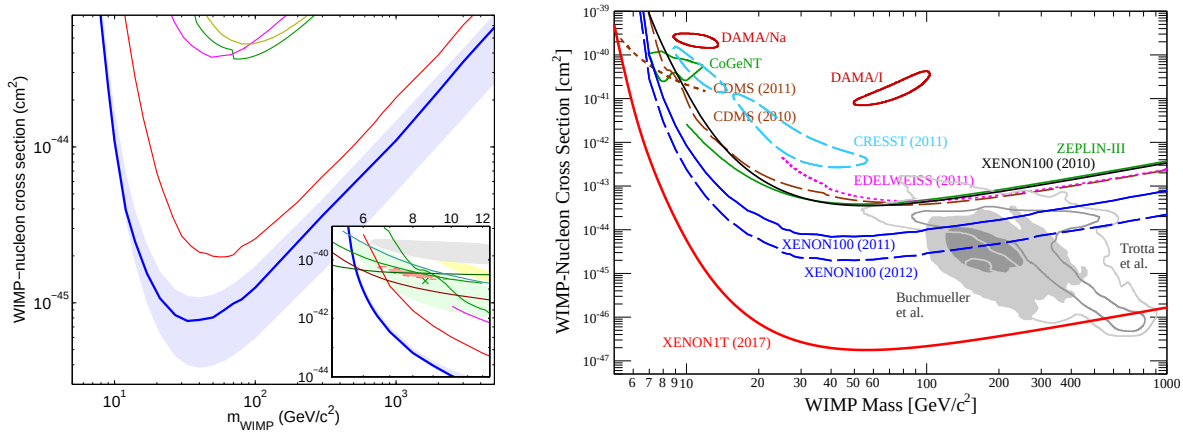

Figure 3.2: Current status for the SI scattering cross section. The constraints from the LUX [40] (left: blue line) and the future prospects from the XENON [41] (right: red line) are shown.

where m_N is the mass of the nucleon. The scalar exchanging process, for example the Higgs boson exchange, can contribute to this cross section.

Now, the LUX [40] sets the strongest constraints on this SI scattering cross section $\sigma_N^{\rm SI}$ (Figure. 3.2). It reaches to $\mathcal{O}(10^{-45}$–$10^{-44})$ cm^2 depending on the mass of the DM. The future prospect of the XENON [41] is also shown in Figure. 3.2. The XENON 1T can reach up to $\mathcal{O}(10^{-47})$ cm^2 for $20 \lesssim m_{\rm DM} \lesssim 200$ GeV.

3.2.2 Spin Dependent Scattering

The spin dependent (SD) scattering cross section is similar to the SI scattering cross section except that it corresponds to the spin dependent process. The effective coupling between the nucleon and the DM is given by $L \ni \sum_{N=p,n} \xi_N \overline{\psi}_{\rm DM} \gamma^5 \gamma_\mu \psi_{\rm DM} \overline{N} \gamma^5 \gamma^\mu N$. The cross section becomes as

$$\sigma_N^{\rm SD} = \frac{12}{\pi} \xi_N^2 \frac{m_N^2 m_{\rm DM}^2}{(m_{\rm DM} + m_N)^2} \,. \tag{3.8}$$

For example, the vector boson exchanging process like the Z boson exchanging process can contribute to this process.

The current constraints come from the XENON100 [42].[2] The future prospects of the XENON 1T are estimated in Ref. [43]. We show these results in Figure. 3.3. Note that the constraints and the future prospects for the cross section between the neutron and the DM are stronger than those for the one between the proton and the DM. The constraints reach to $\mathcal{O}(10^{-40})$ cm^2 and the future prospects reach to $\mathcal{O}(10^{-41})$ cm^2.

[2]The LUX has not published the results of the SD scattering. There is a study [80] giving the SD constraints which is based on the LUX data.

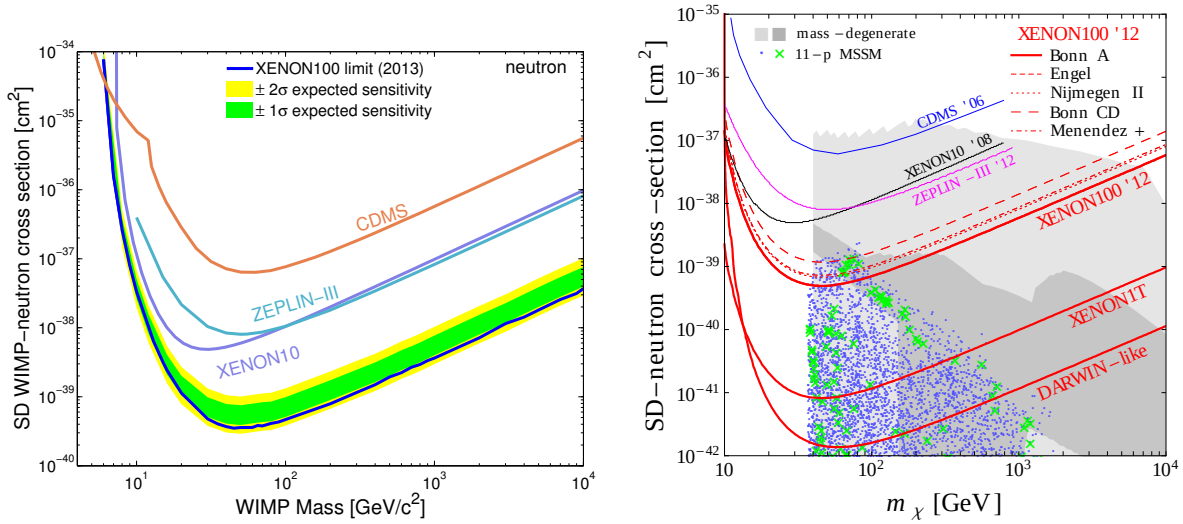

Figure 3.3: Current status for the SD scattering cross section. The constraints from the XENON100 [42](left: blue line) and the future prospects estimated in Ref. [43] (right: red line) are shown.

3.3 Invisible Decay

If the DM is a fermion and has a coupling to the boson X with a form like X-DM-DM, the boson X decays to two DMs for $m_{\rm DM} \leq m_X/2$. Especially, the Higgs boson and the Z boson can decay to two DMs for $m_{\rm DM} \leq m_h/2$ and $m_{\rm DM} \leq M_Z/2$ respectively. Since the DM can not be detected in the collider experiments, these boson seem to decay invisibly. The process which X decays invisibly is called as invisible decay of the particle X. There are experiments to search these processes [44–49]. We briefly review the invisible decay of the Higgs boson and the Z boson here.

3.3.1 Higgs boson Invisible Decay

In the SM, the Higgs boson can decay invisibly only by the process $h \to ZZ^* \to \nu\nu\nu\nu$ with small fraction $\mathrm{Br}(h \to \nu\nu\nu\nu) = \Gamma(h \to \nu\nu\nu\nu)/\Gamma(h \to \mathrm{SM}) \simeq 1 \times 10^{-3}$.[3] On the other hand, in new physics models if the DM couples to the Higgs boson with $m_{\rm DM} \leq m_h/2$, the Higgs boson can also decay invisibly by the process $h \to$ DMs. In this case, the branching ratio of the Higgs boson invisible decay becomes

$$\mathrm{Br}(h \to \text{invisible}) = \frac{\Gamma(h \to \nu\nu\nu\nu) + +\Gamma(h \to \mathrm{DMs})}{\Gamma(h \to \mathrm{SM}) + \Gamma(h \to \mathrm{DMs})} \,. \tag{3.9}$$

This Higgs boson invisible decay process is searched and planed to be searched [44–48].

At present, there are constraints by the global fits of the Higgs boson which use the data from the Tevatron and the LHC [44, 45]. In the analyses, the χ^2 fittings on the experimental cross

[3]Here, we estimate the branching ratio by multiplying the theoretical Higgs branching ratio $\mathrm{Br}(h \to ZZ^* \to 4f) = 0.0264$ [63] and the square of the Z boson branching ratio $\mathrm{Br}(Z \to \nu\nu)$=0.2000±0.0006 [63] where f denotes the SM fermion except the top and the Higgs boson mass is 125 GeV.

sections of the Higgs boson production processes are performed. As the fitting parameters, the Higgs boson couplings to the SM particles and the Higgs boson invisible decay width are used. As the experimental cross sections, they consider the combination of the production processes (gluon gluon fusion, vector boson fusion, and associated production with a top pair) and the decay processes ($h \to ZZ^*, WW^*, \gamma\gamma, \tau^+\tau^-, b\bar{b}$). Various constraints are obtained by changing the assumption for the fitting parameters. In the case all the Higgs boson couplings are assumed to be the SM value and only the Higgs boson invisible decay width is the fitting parameter, the constraints become as $\mathrm{Br}(h \to \text{invisible}) < 0.17$ (95% CL.) [44] and $\mathrm{Br}(h \to \text{invisible}) < 0.19$ (95% CL.) [45]. In the case the Higgs boson couplings to the gluon and the photon are also added to the fitting parameters, the constraints become as $\mathrm{Br}(h \to \text{invisible}) < 0.26$ (95% CL.) [44] and $\mathrm{Br}(h \to \text{invisible}) < 0.29$ (95% CL.) [45].

There are plans to search the invisible decay of the Higgs boson directly. At the High-Luminosity (HL) LHC, there are studies for the process $pp \to Zh$, $h \to$invisible. The sensitivity for this process with 3000 fb^{-1} is estimated [46, 47]. The sensitivity depends on the size of the systematic uncertainties: for "realistic scenario" in Ref. [46] $\mathrm{Br}(h \to \text{invisible}) < 0.062$ (95% CL), for "conservative scenario" in Ref. [46] $\mathrm{Br}(h \to \text{invisible}) < 0.14$ (95% CL) and in Ref. [47] $\mathrm{Br}(h \to \text{invisible}) <$ 0.08–0.16 for the ATLAS and 0.06–0.17 for the CMS (95% CL). The ILC is also planning to measure the Higgs boson invisible decay width directly with the process $e^-e^+ \to Zh$, $h \to$invisible. The sensitivity is estimated as $\mathrm{Br}(h \to \text{invisible}) < 0.004$ (95% CL) with 1150 fb^{-1} at $\sqrt{s} = 250$ GeV [48].

3.3.2 Z boson Invisible Decay

The difference between the Higgs boson invisible decay and the Z boson invisible decay is that the Z boson can decay invisibly with a large fractions even in the SM. It is because the Z boson couples to the neutrinos and it can decay to two neutrinos. This decay width $\Gamma(Z \to \nu\nu)$ is well measured at the LEP [49]. If the DM couples to the Z boson with $m_{\mathrm{DM}} \leq M_Z/2$, new contribution to the invisible decay width is added,

$$\Gamma(Z \to \text{invisible}) = \Gamma(Z \to \nu\nu) + \Gamma(Z \to \text{DM DM})\,. \tag{3.10}$$

Thus, a gap between the experimental value of $\Gamma(Z \to \text{invisible})$ and the SM prediction value of $\Gamma^{\mathrm{SM}}(Z \to \nu\nu)$ is used to set the constraint on new physical invisible decay width like a decay to the DMs: $\Delta\Gamma(Z \to \text{invisible}) = \Gamma(Z \to \text{invisible}) - \Gamma^{\mathrm{SM}}(Z \to \nu\nu) < 2.0$ MeV (95% CL) [49].

3.4 Collider Searches

The DM can be produced at the colliders and there are experiments to search it. There are two types of the production: (i) the direct production [80, 81] and (ii) the production by other particle's decay [50, 51, 82, 83]. In the former case (i), the DMs are produced by the process like $pp \to$ DM DM or $e^+e^- \to$ DM DM. However, since the DM can not be detected at the

collider, these processes give no signals in events. Thus, the additional radiation process, i.e. mono-jet or mono-photon process, is considered $pp \to \text{DM DM } j$ or $e^+e^- \to \text{DM DM } \gamma$. We review these searches in Sec. 3.4.1. The later case (ii) depends on not only the DM itself but also the model which includes the DM. The models which contain the DM candidates typically introduce additional particles and the Z_2 symmetry. The Z_2 charge of the DM is odd and the additional particles which also have odd charge can decay to DM. Thus, when the additional particles are within the range of the collider, they are produced and decay to the DMs. The processes like $pp \to Y_1 Y_2 \to X$ DM DM can appear in the experiments where Y_i denotes the additional particles and X denotes the combination of the SM particles. For example, in the SUSY case, the heavy neutralino χ_2^0 and the chargino $\chi_1^\pm$ can be produced at the LHC with the process like $pp \to W^\pm \to \chi_2^0 \chi_1^\pm \to Z\chi_1^0 W^\pm \chi_1^0 \to ll\chi_1^0 l\nu\chi_1^0$ where l denotes the SM lepton and χ_1^0 is the DM (see also Sec. 2.1.6). As same as the direct production, the DMs can not be detected. Thus the final states with the SM particles and the missing energy are searched. We review this heavy neutralino and chargino production searches of the SUSY models at the LHC in Sec. 3.4.2.

3.4.1 Mono-photon and Mono-jet

The mono-photon events and the mono-jet events are the typical signature of the DM production. Since the DM can not be detected in the collider experiments, the initial state radiations (ISR) become the clues to search the DM. The DMs are measured as the missing energy and the signal contains the ISR and the missing energy.

In the e^+e^- collision, the process $e^+e^- \to \text{DM DM } \gamma$ can occur where the ISR is the photon. The LEP searched this process [81]. However, the results are consistent with the value of the SM prediction process $e^+e^- \to \nu\nu\gamma$. The constraint is set on the unknown process $e^+e^- \to X\gamma$: its cross section should be $\lesssim$ 0.05–0.2 pb at $\sqrt{s} = 205$ GeV depending on the missing energy 60–200 GeV (see Figure 3.4).

In the LHC, the process $pp \to \text{DM DM } j$ can occur where the ISR is the jet. It is the same case as the LEP that there is no excess in the signal. In Ref. [80], the constraints from the CMS [84] at $\sqrt{s} = 8$ TeV 19.5fb^{-1} are translated to the constraints on the generic vector mediator model. In Ref. [80], two vector mediator models are considered: vector model $L \ni \sum_q g_q Z'_\mu \bar{\psi}_q \gamma^\mu \psi_q + g_{\text{DM}} Z'_\mu \bar{\psi}_{\text{DM}} \gamma^\mu \psi_{\text{DM}}$ and axial-vector model $L \ni \sum_q g_q Z'_\mu \bar{\psi}_q \gamma^\mu \gamma^5 \psi_q + g_{\text{DM}} Z'_\mu \bar{\psi}_{\text{DM}} \gamma^\mu \gamma^5 \psi_{\text{DM}}$ where q denotes the SM quarks. The constraints are set on the couplings g_q, g_{DM} and the masses of Z'_μ and the DM. The results with assuming $g_q = g_{\text{DM}}$ is shown in the blue lines of Figure 3.5. Here, we roughly extract the constraints for the case that the mediator is the SM Z boson and the DM couples to the SM Z boson with the axial-vector coupling. For the SM Z boson, there exists both of the vector and axial-vector couplings $L \ni \sum_q (g_q^V Z_\mu \bar{\psi}_q \gamma^\mu \psi_q + g_q^A Z_\mu \bar{\psi}_q \gamma^\mu \gamma^5 \psi_q)$ and $g_u^V = 0.07, g_u^A = 0.19, g_d^V = -0.13, g_d^A = -0.19$ while the constraints are set by assuming there is only vector (axial-vector) coupling. However, since the cross section becomes $\sigma \propto (g_q^V)^2 + (g_q^A)^2$ in the massless limit $m_q \to 0$ and the results for the vector model are almost same as the axial-

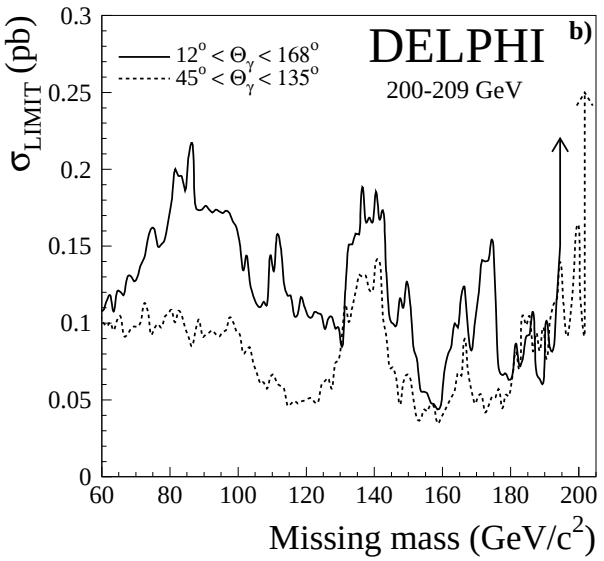

Figure 3.4: The constraints from the LEP mono-photon search [81] are shown. Depending on the missing mass, the cross section for $e^+e^- \to X\gamma$ is constrained at $\sqrt{s} = 205$ GeV.

vector model (see Figure 3.5), we roughly estimates that the constraints in this case becomes same as those of the axial-vector model with $g_q \sim 0.2$ and $M_{\rm med} = M_Z = 91.2$ GeV. Then the constraints on the DM coupling to the Z boson become as $|g_{\rm DM}| \lesssim 0.2$–$0.6$ for the mass of the DM 10–100 GeV.

3.4.2 Heavy Neutralino/Chargino Production

The production of the neutralinos/charginos are searched at the LHC like those of the colored SUSY particles (see Sec. 2.1.6). Although the production cross sections of the neutralinos/charginos are smaller than those of the colored SUSY particle, typically the decay product contains the leptons and the QCD background can be suppressed. Thus, the neutralinos/charginos can be searched at the LHC.

As shown in Sec. 2.2, the heavy sfermion scenarios in the SUSY models are well studied. In these scenarios, the neutralinos/charginos searches become important since the sfermions are heavy and not produced at the LHC. In this case, the pair of the neutralinos/charginos are produced by the electroweak process. If kinematically arrowed, the produced neutralino/chargino decay to the DM associated with the gauge boson or the Higgs boson. These processes are searched and especially the process,

$$pp \to \chi_2^0 \chi_1^\pm \to Z\chi_1^0 W^\pm \chi_1^0 \to ll\chi_1^0 l\nu\chi_1^0 , \tag{3.11}$$

(l denotes e, μ, τ) are well studied by the ATLAS and CMS since this process gives a high sensitivity [50, 51, 82, 83]. Here, we review the searches for this process.

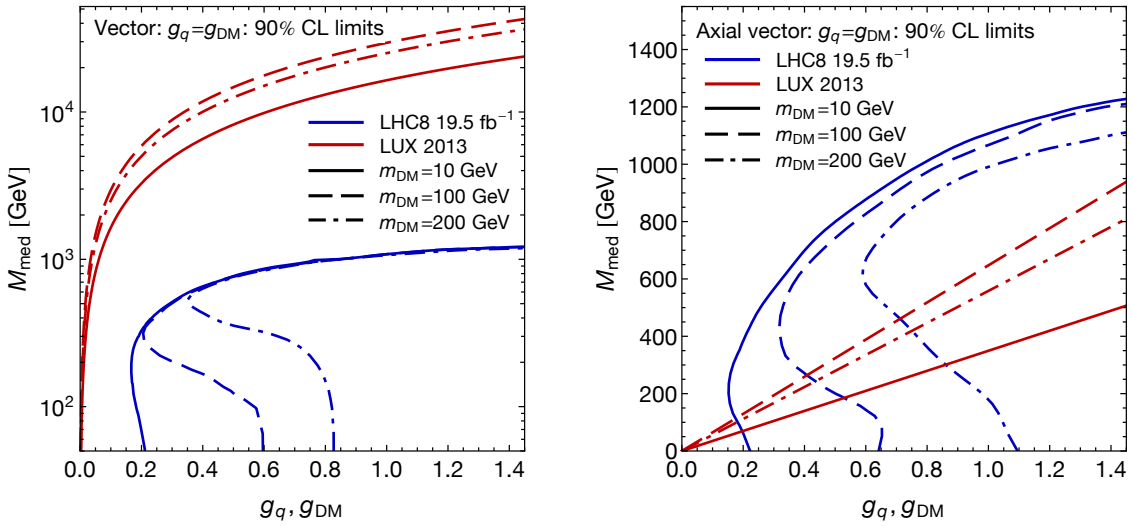

Figure 3.5: The constraints from the mono-jet search are shown. These are the results of Ref. [80] and the constraints from the CMS [84] at $\sqrt{s} = 8$ TeV 19.5fb^{-1} are translated to the constraints on the generic vector mediator model (left: vector model, right: axial-vector model). See text for details.

At 8 TeV, since there is no discovery of the signal for these searches, the constraints are set by the ATLAS with 20.3 fb^{-1} [50]. Note that the CMS also gives the constraints which are weaker than the ATLAS results [82]. When the sleptons are absent, the process (3.11) gives the strongest constraints. Although there is also analysis for the Wh process, $pp \to \chi_2^0\chi_1^\pm \to h\chi_1^0 W^\pm\chi_1^0 \to ll\chi_1^0 l\nu\chi_1^0$, it gives very weak constraints. The constraints for the process (3.11) given by the ATLAS [50] are shown in Figure 3.6. This constraints are set by assuming the simplified pure Bino-Wino model:

(i) There exist the pure Bino DM χ_1^0, the pure Wino neutralino χ_2^0 and the pure Wino chargino $\chi_1^\pm$.

(ii) The masses of χ_2^0 and $\chi_1^\pm$ are the same, $m_{\chi_2^0} = m_{\chi_1^\pm}$.

(iii) They decay as $\chi_2^0 \to Z\chi_1^0$ and $\chi_1^\pm \to W^\pm\chi_1^0$ with 100%, i.e. Br($\chi_2^0 \to Z\chi_1^0$) =Br($\chi_1^\pm \to W^\pm\chi_1^0$)=1.

Note that the pure Wino can not decay to the Bino. The slight mixing with the Higgsino makes it possible for the pure Wino to decay to the Higgs boson and the Bino. Even in this case, the (almost) pure Wino can not decay to the Z boson and the Bino with larger fraction. Thus, this pure Bino-Wino model is a toy model and only the benchmark of the searches. In addition, in this analysis, the production cross section is calculated by assuming the pure Wino. It makes the cross section larger than that of the neutralinos which contain the Higgsino component. In order to translate these constraints to the physical model, we need to simulate the ATLAS analysis and reinterpret the constraints in that model (see also Sec. 5.5). As a benchmark, the pure Wino mass up to 350 GeV is excluded when the mass of the DM is 0–100 GeV.

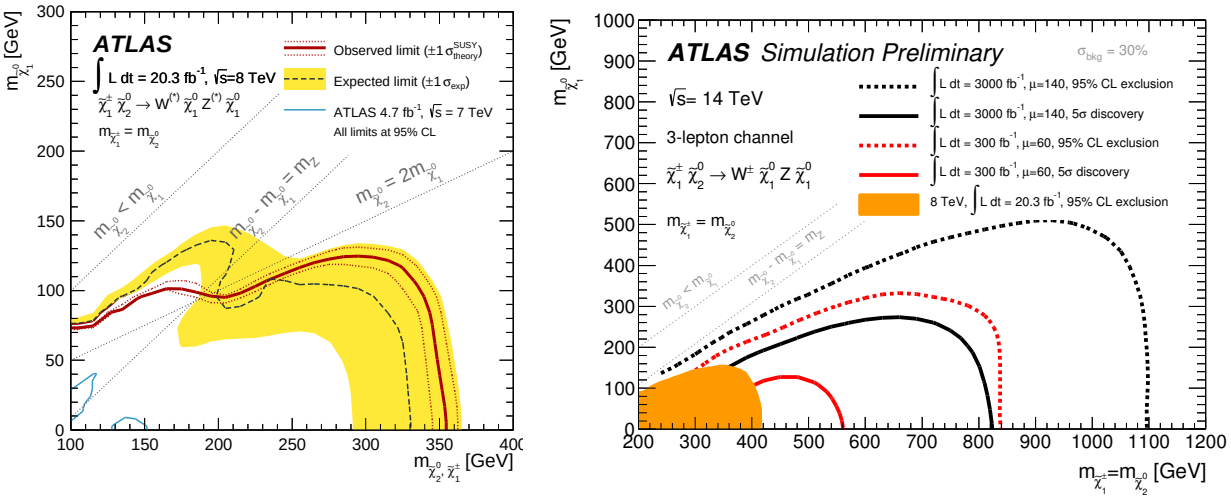

Figure 3.6: The constraints and the future prospects of the neutralino/chargino searches by the ATLAS are shown. (left) The constraints set by the ATLAS [50] at 8 TeV are shown. (right) The future prospects by the ATLAS [51] at 14 TeV with 300 fb^{-1} and 3000 fb $^{-1}$ are shown. In these plots, the pure Bino-Wino model is assumed (see text for details).

The future prospects at 14 TeV are also given by the ATLAS [51] and the CMS [83]. Since the ATLAS and the CMS give the similar results, we review the ATLAS analysis. It is the same as the 8 TeV case, the process (3.11) gives a highest sensitivity while the Wh process gives a weaker sensitivity. The future prospects for the process (3.11) given by the ATLAS [51] is shown in Figure 3.6. Here, the pure Bino-Wino model is also assumed. Thus, we need to simulate and reinterpret the future prospects in order to apply them to the physical model. In Figure 3.6, the results with 300 fb^{-1} and 3000 fb $^{-1}$ are shown. The exclusion limit for the Wino mass can be 800 GeV and 1100 GeV for the DM mass 0–100GeV with 300 fb^{-1} and 3000 fb $^{-1}$ respectively.

3.5 Indirect Detection

The DM can annihilate in the present Universe. There are many experiments to search this phenomenon. Especially, the observation of the cosmic rays (Sec. 3.5.1) and the observation of the neutrinos from the Sun (Sec. 3.5.2) exist. Here, we briefly review these observations.

3.5.1 Cosmic Rays

In the present Universe, the DM can annihilate to the SM particles in the high DM density regions. The produced SM particles emit the photons, positrons, anti-protons and so on which lead cosmic rays. For the light DM, the strong constraints come from the observation by the Fermi-LAT [85]. In the experiment, the targets are the gamma rays from the dwarf spheroidal satellite galaxies of the Milky Way where the dwarf spheroidal satellite galaxies contain the

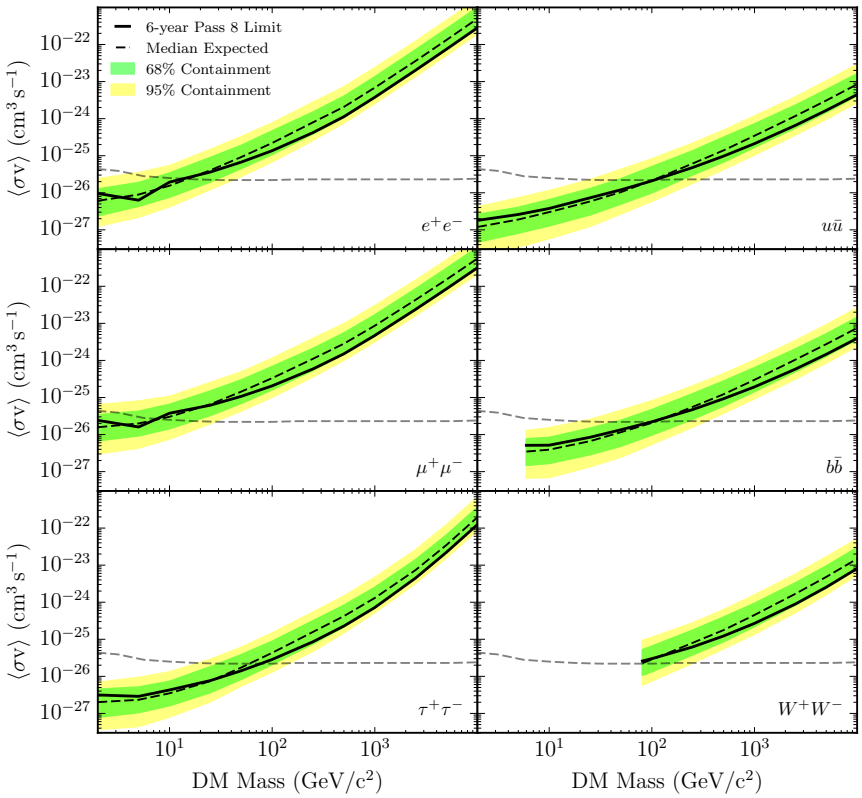

Figure 3.7: The constraints from the observations of the gamma rays from the dwarf spheroidal satellite galaxies by the Fermi-LAT are shown [85]. The constraints on the each annihilation channel $e^+e^-, \mu^+\mu^-, \tau^+\tau^-, u\bar{u}, b\bar{b}, W^+W^-$ are shown where 100% branching fraction is assumed for each channel.

substantial DM component. Since there is no excess of the signal, there are constraints. The constraints are set on the DM annihilation cross section in the present Universe: $\langle\sigma v\rangle$ with the limit $v \to 0$. The results are shown in Figure 3.7. Here, the constraints on the each annihilation channel $e^+e^-, \mu^+\mu^-, \tau^+\tau^-, u\bar{u}, b\bar{b}, W^+W^-$ are shown where 100% branching fraction is assumed for each channel. W^+W^- channel is considered when the DM mass is larger than the W boson mass. As shown, the constraints are similar for all channels since the gamma ray spectra are similar and it mainly depends on the mass of the DM. The constraints reach up to $10^{-27} \sim 10^{-26}\text{cm}^3\text{s}^{-1}$ for the mass of the DM 10–100 GeV.

3.5.2 DM Annihilation in the Sun

In the present Universe, the DM can be captured in the Sun. The captured DMs annihilate to the SM particles and it leads to generate the neutrinos. The emitted neutrinos from the Sun are searched. However, there is no excess now and the Super-Kamiokande gives the strongest

bound [86]. The constraints are set on the effective scattering cross section as [87]

$$\sigma_p^{\mathrm{SI/SD(eff)}} = \sigma_p^{\mathrm{SI/SD}} \tanh^2 \left(\sqrt{\Gamma_{\mathrm{cap.}}\Gamma_{\mathrm{ann.}}} t_\odot \right) , \tag{3.12}$$

where $\sigma_p^{\mathrm{SI/SD}}$ is the SI/SD scattering cross section, $\Gamma_{\mathrm{cap.}}, \Gamma_{\mathrm{ann.}}$ are the capture rate and the annihilation rate of the DM in the Sun and $t_\odot \sim$4.5 billion years is the age of the solar system. Here, $\sqrt{\Gamma_{\mathrm{cap.}}\Gamma_{\mathrm{ann.}}} t_\odot$ can be calculated as [87]

$$\sqrt{\Gamma_{\mathrm{cap.}}\Gamma_{\mathrm{ann.}}} t_\odot = 1.8(1.3) \times \left(\frac{\sigma_p^{\mathrm{SI/SD}}}{10^{-40}\mathrm{cm}^2} \right)^{1/2} \left(\frac{\langle \sigma v \rangle |_{v\to 0}}{10^{-29}\mathrm{cm}^3\mathrm{s}^{-1}} \right)^{1/2} \left(\frac{50\mathrm{GeV}}{m_{\mathrm{DM}}} \right)^{1/4} . \tag{3.13}$$

Note that the DM annihilation cross section is the one in the present Universe, i.e. $\langle \sigma v \rangle$ with the limit $v \to 0$. When $\sqrt{\Gamma_{\mathrm{cap.}}\Gamma_{\mathrm{ann.}}} t_\odot \gg 1$ is satisfied, the DMs are in the equilibrium between the capture and the annihilation. In this case, the capture and the annihilation occur continuously and the effective scattering cross section become as $\sigma_p^{\mathrm{SI/SD(eff)}} = \sigma_p^{\mathrm{SI/SD}}$. Note that $\tanh(x) = 1$ for $x \gg 1$ and $\tanh(x) = 0$ for $x = 0$.

The constraints are set by the Super-Kamiokande [86] (Figure 3.8). The results are shown with assuming the branching fraction 100% for each $b\bar{b}, \tau^+\tau^-, W^+W^-$) channel. W^+W^- channel is considered when the mass of the DM exceeds the mass of the W boson. The constraints for the $\tau^+\tau^-$ channel is stronger than the $b\bar{b}$ channel. This is because τ emits the neutrino directly by its decay while b emits the neutrons from the hadronic decays. The constraints on the SI effective scattering cross section are much weaker than those of the direct detections (Sec. 3.2.1). On the other hand, the constraints on the SD effective scattering cross section are same order with those of the direct detections (Sec. 3.2.2). However, these constraints are set on the effective cross section (3.12) where the branching fraction is assumed to be 100%. Note that there are differences of the branching ratio factor and the $\tanh^2$ factor between these constraints and the constraints from the direct detections. Thus, these constraints can be weaker than those of the direct detections depending on the branching ratio and the annihilation cross section.

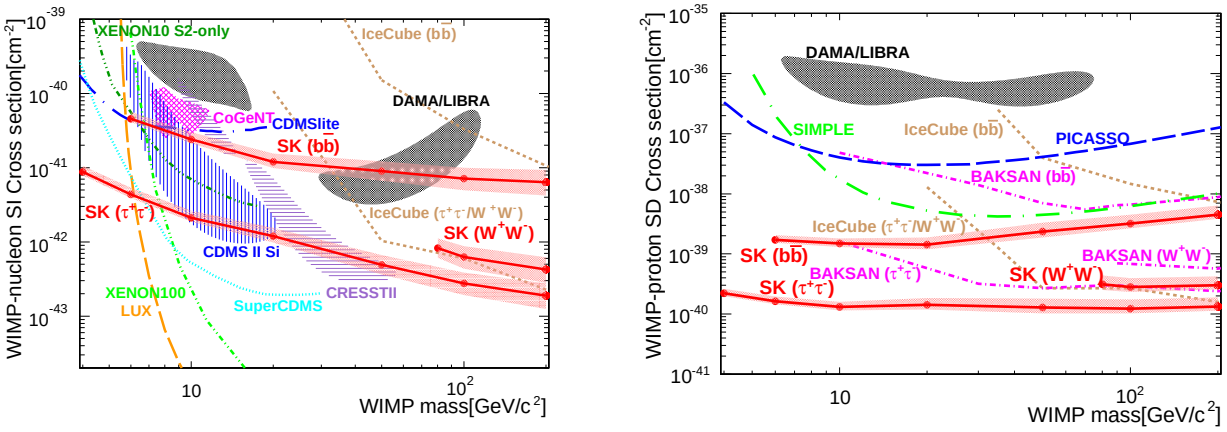

Figure 3.8: The constraints from the Super-Kamiokande which searches the neutrino from the Sun are shown [86]. The left (right) figure shows the result for the SI (SD) effective scattering cross section. The red line SK($b\bar{b}$) (SK($\tau^+\tau-$), SK(W^+W^-)) shows the constraints when the branching fraction of the annihilation to $b\bar{b}$ ($\tau^+\tau^-, W^+W^-$) channel is assumed to be 100%.

Chapter 4

Bino-Higgsino Resonant DM model

In this thesis, we investigate the phenomenology of the Bino-Higgsino resonant DM model. As we see in Sec. 2.2, the heavy sfermion scenario is one of the attractive scenario since it can explain the Higgs boson mass, evade the LHC constraints and improve the FCNC problem. In that case, the Bino-Higgsino resonant DM model is one of the good candidate for the DM models as discussed in Sec. 2.2.6. The current relic abundance is explained by the resonant enhancement of the annihilation cross section. Here, we consider the Bino-Higgsino resonant DM model as one of the heavy sfermion scenarios. We assume all the sfermions and heavy Higgses are heavy $> \mathcal{O}(1\text{–}10)$ TeV and do not consider their effects.[1] We also assume the gluino and the Winos are heavier than a few TeV which do not affect the phenomenology of the Bino-Higgsino system and we do not consider their effects (Sec. 4.1). Then, these models are determined by only three parameters, the Bino mass M_1, the Higgsino mass μ and $\tan\beta$. Although it is simple, this model gives a variety of phenomena. We investigate this model comprehensively. Our study includes the investigation of the whole parameter space of $(M_1, \mu, \tan\beta)$, the phenomenology of the blind spot and all the possible phenomena and experiments (see Sec. 5).

In Sec. 4.1, we introduce the Bino-Higgsino resonant DM model. The Lagrangian is shown in Sec. 4.2. In Sec. 4.3 and 4.4, the behavior of the masses and the couplings of the DM are shown. The brief description of the DM is also shown in Sec. 4.4. In Sec. 4.5, the behavior of the couplings of the heavy neutralinos and the chargino is discussed which is important in the LHC analyses. The detailed analysis and the results will be discussed in Chapter 5 and 6.

4.1 Matter Content and Conditions

The matter content in the Bino-Higgsino model is shown in Table 4.1. Here, we consider the case where all the sfermions and heavy Higgses are heavy $> \mathcal{O}(1\text{–}10)$ TeV and do not consider their effects. We also assume that the masses of the gluino and the Winos are heavier than a few TeV.

[1] As shown in Sec. 2.1.5, to explain the Higgs mass, the masses and A-terms of heavy particles, especially of the stops, are restricted in some parameter spaces. However, since they are heavy enough, we do not consider their effects and we set the Higgs boson mass 125 GeV.

SM fermions (quarks, leptons)		
SM gauge bosons		
$H_u^0(h_u, A_u)$ $H_d^0(h_d, A_d)$	$\Rightarrow$	$\left.\begin{matrix} H \\ A \end{matrix}\right)\rightarrow$ heavy $> \mathcal{O}(1-10)$TeV h
χ_B $\chi_{H_u^0}$ $\chi_{H_d^0}$	$\Rightarrow$	χ_1^0 χ_2^0 χ_3^0
$\chi_{H_u^+}$ $\chi_{H_d^-}$	$\Rightarrow$	$\chi_1^\pm$

Table 4.1: The matter content of the Bino-Higgsino resonant model. The Higgs fields, the neutralino fields and the chargino fields are diagonalized and the heavy Higgses become heavy.

There are following reasons. First, the gluino does not mix with the Higgsino and the Bino and does not affect the phenomenology of the DM. On the other hand, the Wino mixes with the Bino via the mixing with the Higgsino. However, when the mass of the Wino are heavier than ∼500–700 GeV, the Wino also does not affect the phenomenology of the DM as shown in Appendix B. Second, when the gluino and/or the Winos are light $\mathcal{O}(100)$ GeV, the LHC phenomenology changes. However, it is independent from the DM phenomenology and the existence of these light gluino and Winos enlarges the covered region of the constraints and the future prospects of the LHC SUSY searches. To evade the constraints and to give the conservative future prospects, the masses of the gluino and the Winos are assumed heavier than a few TeV where the gluino/Winos does not change the LHC phenomenology of the Bino/Higgsinos. Thus, we do not consider their effects.

Here, we do not consider the CP-violation terms in the Lagrangian.[2] Then the Lagrangian is determined only by three parameters, the Bino mass $M_1 > 0$, the real Higgsino mass μ and $\tan\beta$ (see the next section Sec. 4.2). As we will see in Sec. 5.1, the current relic abundance can be explained at $m_{\chi_1^0} \sim m_h/2$ or $M_Z/2$ and $|\mu| \lesssim 2500$ GeV. Thus, here we consider the following parameter range,

$$20\text{GeV} \leq M_1 \leq 80\text{GeV}\,, \tag{4.1}$$

$$100\text{GeV} \leq |\mu| \leq 2500\text{GeV}\,, \tag{4.2}$$

$$2 \leq \tan\beta \leq 50\,, \tag{4.3}$$

where the condition for μ is to satisfy the LEP bound for the chargino $m_{\chi_1^\pm} = |\mu|$ [63]. In the outer region of Eq. (4.1) and (4.2), the DM becomes overabundant except the well-tempered

[2]The existence of the CP-violation terms adds the terms like $L \ni \lambda h \bar{\psi}_{\chi_1^0}\gamma^5\psi_{\chi_1^0}$. It changes the phenomenology of the DM. It is interesting to investigate such case but it is beyond this thesis and we simply assume there is no CP-violating terms.

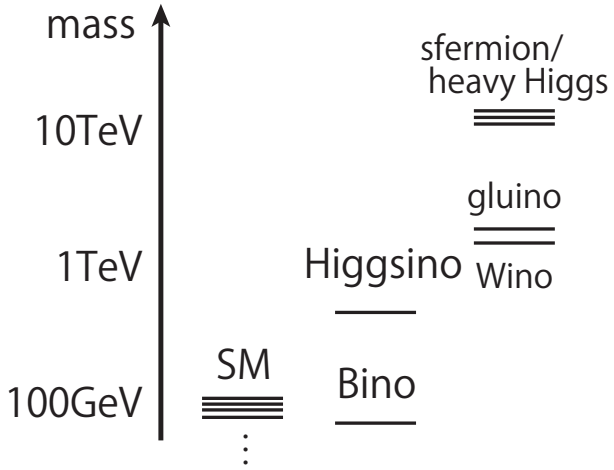

Figure 4.1: The mass spectrum of the Bino-Higgsino resonant model is shown.

region (see Sec. 2.2.6). The mass spectrum of this model is shown in Figure. 4.1. We define z, z_1 as

$$z \equiv \frac{M_Z s_W}{\mu}, \quad z_1 \equiv \frac{M_1}{\mu}\,. \tag{4.4}$$

Note that $|z|, |z_1| < 1$. In the following subsections, we show the expansions of the masses or the couplings by these values.

4.2 Lagrangian

The Lagrangian after the spontaneous symmetry breaking, integrating out the heavy fields and neglecting the gluino/Winos in Eq. (2.7) is written as follows

$$\begin{aligned} L \;=\; & L_{\rm SM} + \sum_X i\overline{\chi}_X \overline{\sigma}^\mu \partial_\mu \chi_X + \left(-\frac{1}{2} M_1 \chi_B \chi_B + \mu \chi_{H_u^0} \chi_{H_d^0} - \mu \chi_{H_u^+} \chi_{H_d^-} + h.c. \right) \\ & - \frac{1}{\sqrt{2}} g' v s_\beta \chi_B \chi_{H_u^0} + \frac{1}{\sqrt{2}} g' v c_\beta \chi_B \chi_{H_d^0} - \frac{1}{2} g' c_\alpha h \chi_B \chi_{H_u^0} - \frac{1}{2} g' s_\alpha h \chi_B \chi_{H_d^0} + h.c. \\ & - e \overline{\chi}_{H_u^+} \overline{\sigma}^\mu \chi_{H_u^+} A_\mu + e \overline{\chi}_{H_d^-} \overline{\sigma}^\mu \chi_{H_d^-} A_\mu \\ & + \left(-\frac{1}{\sqrt{2}} g \overline{\chi}_{H_u^+} \overline{\sigma}^\mu \chi_{H_u^0} W_\mu^+ - \frac{1}{\sqrt{2}} g \overline{\chi}_{H_d^-} \overline{\sigma}^\mu \chi_{H_d^0} W_\mu^- + h.c. \right) \\ & + \frac{e}{s_{2W}} \overline{\chi}_{H_u^0} \overline{\sigma}^\mu \chi_{H_u^0} Z_\mu - \frac{e}{s_{2W}} \overline{\chi}_{H_d^0} \overline{\sigma}^\mu \chi_{H_d^0} Z_\mu - \frac{e}{t_{2W}} \overline{\chi}_{H_u^+} \overline{\sigma}^\mu \chi_{H_u^+} Z_\mu + \frac{e}{t_{2W}} \overline{\chi}_{H_d^-} \overline{\sigma}^\mu \chi_{H_d^-} Z_\mu \,, \end{aligned} \tag{4.5}$$

where $X = B, H_u^+, H_u^0, H_d^0, H_d^-$. When the heavy Higgses are heavy enough, $\alpha \sim \beta - \pi/2$ (i.e. $c_\alpha \sim s_\beta, s_\alpha \sim -c_\beta$) is satisfied (see also Eq. (2.37)).

The mass matrix of the neutralinos (Eq. (2.30)) becomes 3×3 matrix,

$$L \ni -\frac{1}{2}(\chi_B \ \chi_{H_d^0} \ \chi_{H_u^0}) \begin{pmatrix} M_1 & -M_Z s_W c_\beta & M_Z s_W s_\beta \\ -M_Z s_W c_\beta & 0 & -\mu \\ M_Z s_W s_\beta & -\mu & 0 \end{pmatrix} \begin{pmatrix} \chi_B \\ \chi_{H_d^0} \\ \chi_{H_u^0} \end{pmatrix} + h.c.. \tag{4.6}$$

Note that $M_Z s_W = g'v/2$. We diagonalize this matrix M_n with a real orthogonal matrix O_n

$$O_n M_n O_n^T = \begin{pmatrix} \epsilon_1 m_{\chi_1^0} & 0 & 0 \\ 0 & \epsilon_2 m_{\chi_2^0} & 0 \\ 0 & 0 & \epsilon_3 m_{\chi_3^0} \end{pmatrix}, \quad \begin{pmatrix} \chi_1^0 \\ \chi_2^0 \\ \chi_3^0 \end{pmatrix} \equiv O_n \begin{pmatrix} \chi_B \\ \chi_{H_d^0} \\ \chi_{H_u^0} \end{pmatrix}. \tag{4.7}$$

$\epsilon_i = \pm 1$ and the negative mass $\epsilon_i = -1$ is absorbed by the additional rotation of the neutralino fields with a diagonal matrix Ψ_n where $(\Psi_n)_{ij} = \delta_{ij}\eta_i$ and $\eta_i = 1$ for $\epsilon_i = 1$, $\eta_i = i$ for $\epsilon_i = -1$. The chargino is composed only by the Higgsino. The mass of the chargino is $\epsilon_\mu \mu$ where $\epsilon_\mu = \mathrm{sign}(\mu)$.

After diagonalizing the neutralino mass matrix, the Lagrangian is rewritten with the Majorana neutralinos ($\psi_{\chi_i^0}$) and the Dirac chargino ($\psi_{\chi_1^\pm} = \left(\epsilon_\mu i\sigma^2 \overline{\chi}^T_{H_d^-} \ \chi_{H_u^+}\right)^T$) as

$$\begin{aligned} L &= L_{\rm SM} + \frac{1}{2}\sum_{i=1,2,3} i\overline{\psi}_{\chi_i^0}\gamma^\mu \partial_\mu \psi_{\chi_i^0} + i\overline{\psi}_{\chi_1^\pm}\gamma^\mu \partial_\mu \psi_{\chi_1^\pm} - \frac{1}{2}\sum_{i=1,2,3} m_{\chi_i^0}\overline{\psi}_{\chi_i^0}\psi_{\chi_i^0} - \mu\epsilon_\mu \overline{\psi}_{\chi_1^\pm}\psi_{\chi_1^\pm} \\ &\quad + h\sum_{i,j=1,2,3} \overline{\psi}_{\chi_i^0}\left(\lambda^h_{Lij}P_L + \lambda^h_{Rij}P_R\right)\psi_{\chi_j^0} + Z_\mu \sum_{i,j=1,2,3} \overline{\psi}_{\chi_i^0}\gamma^\mu \lambda^Z_{Lij}P_L \psi_{\chi_j^0} \\ &\quad + W^+_\mu \sum_{i=1,2,3} \overline{\psi}_{\chi_1^\pm}\gamma^\mu \left(\lambda^W_{L1i}P_L + \lambda^W_{R1i}P_R\right)\psi_{\chi_i^0} + h.c. \\ &\quad - e\overline{\psi}_{\chi_1^\pm}\gamma^\mu \psi_{\chi_1^\pm} A_\mu - \frac{e}{t_{2W}}\overline{\psi}_{\chi_1^\pm}\gamma^\mu \psi_{\chi_1^\pm} Z_\mu \,, \end{aligned} \tag{4.8}$$

where

$$\lambda^h_{Lij} = -\frac{1}{2}g' (O_n)_{i1}\left(c_\alpha (O_n)_{j3} + s_\alpha (O_n)_{j2}\right)\eta_i^*\eta_j^* \,, \tag{4.9}$$

$$\lambda^h_{Rij} = \left(\lambda^h_{Lji}\right)^* , \tag{4.10}$$

$$\lambda^Z_{Lij} = \frac{e}{s_{2W}}\eta_i\eta_j^*\left((O_n)_{i3}(O_n)_{j3} - (O_n)_{i2}(O_n)_{j2}\right) , \tag{4.11}$$

$$\lambda^W_{L1i} = -\frac{1}{\sqrt{2}}g\eta_i^* (O_n)_{i3} \ , \tag{4.12}$$

$$\lambda^W_{R1i} = \frac{1}{\sqrt{2}}g\epsilon_\mu\eta_i (O_n)_{i2} \ . \tag{4.13}$$

All phenomenology is determined by these couplings and the masses of the neutralinos and the chargino which depend on only M_1, μ and $\tan\beta$.

4.3 Masses

Here, we show the behavior of the masses.

With the expansion by $z = M_Z s_W/\mu$, the eigenvalues of the mass matrix are written as (see Appendix C)

$$\begin{aligned} m_1 &= M_1\left(1 - z^2\frac{1}{1-z_1^2}(1-\frac{1}{z_1}s_{2\beta}) + \mathcal{O}\left(z^4\right)\right), \\ m_2 &= -\mu\left(1 + \frac{1}{2}z^2\frac{1}{1+z_1}(1-s_{2\beta}) + \mathcal{O}\left(z^4\right)\right), \\ m_3 &= \mu\left(1 + \frac{1}{2}z^2\frac{1}{1-z_1}(1+s_{2\beta}) + \mathcal{O}\left(z^4\right)\right). \end{aligned} \tag{4.14}$$

Here, m_i denotes the eigenvalues of the mass matrix M_n (Eq. (4.6)) and it does not equivalent to the mass of χ_i^0, $m_{\chi_i^0}$. The relations between m_i and $m_{\chi_i^0}$ are depending on the parameters. Especially in our parameter regions, for $\mu > 0$, the relation becomes as $m_i = \epsilon_i m_{\chi_i^0}$. On the other hand, for $\mu < 0$, the relation changes as $m_{2,3} = \epsilon_{2,3} m_{\chi^0_{2,3}}$ or $m_{2,3} = \epsilon_{3,2} m_{\chi^0_{3,2}}$ depending on the parameters. For example, in the case of $\mu < 0$, if we change the value of M_1 fixing other parameters, the flip of $|m_2| > |m_3| \to |m_2| < |m_3|$ can occur. The relation between $|m_2|$ and $|m_3|$ is calculated as

$$|m_3| - |m_2| = z^2\frac{1}{1-z_1^2}(z_1 + s_{2\beta}) + \mathcal{O}\left(z^4\right). \tag{4.15}$$

Obviously, the order of $|m_2|$ and $|m_3|$ flips at[3]

$$M_1 \sim -\mu s_{2\beta}\,. \tag{4.16}$$

With this flip, the couplings seems to change discontinuously when one keeps track of the couplings of χ_2^0 (χ_3^0). Now, we define χ_p^0 (χ_m^0) as the heavy neutralino whose ϵ is positive (negative): i.e. $\chi_p^0 = \chi_2^0$ and $\chi_m^0 = \chi_3^0$ when $\epsilon_2 > 0$ and $\epsilon_3 < 0$, $\chi_p^0 = \chi_3^0$ and $\chi_m^0 = \chi_2^0$ when $\epsilon_2 < 0$ and $\epsilon_3 > 0$.[4] Then, if we keep track of the couplings of χ_p^0 (χ_m^0), there is no discontinuous change. This is because the subscript $2, 3$ of χ_2^0, χ_3^0 is only determined by the order of the mass and it is not determined by its component (i.e. more like $\chi_{H_d^0}$ or more like $\chi_{H_u^0}$).

From Eq. (4.14), the mass of the DM becomes $m_{\chi_1^0} \sim M_1$ and the masses of two heavy neutralinos become $m_{\chi_2^0} \sim m_{\chi_3^0} \sim |\mu|$. Note that the mass of the chargino is $\epsilon_\mu \mu$ as shown in Sec. 4.2. Note that, $m_h < 2|m_{\chi^0_{2,3}}| \sim 2m_{\chi_1^\pm}$ and $M_W < m_{\chi_1^0} + m_{\chi_1^\pm}$ are satisfied. Thus, the Higgs boson and the Z boson can not decay to the heavy neutralinos/charginos and the W boson can not decay to the DM and the chargino.

4.4 Dark Matter

In the current set up, the lightest neutralino LSP χ_1^0 can be a candidate for the DM. This DM is mainly composed of the Bino and slightly couples with the Higgsino (see Eq. (4.6)). Thus, we call

[3] This is the same condition of the blind spot which we see in Eq. (4.22).

[4] Note that $\epsilon_1 = 1$ and $\epsilon_2 \times \epsilon_3 = -1$ holds when $|\mu| \gg M_1$.

this model as the Bino-Higgsino DM model. The phenomenologies of this DM are determined only by its mass $m_{\chi_1^0}$ and the two couplings λ^h, λ^Z:

$$L_{\rm DM} = \frac{1}{2} i\overline{\psi}_{\chi_1^0}\gamma^\mu\partial_\mu\psi_{\chi_1^0} - \frac{1}{2} m_{\chi_1^0}\overline{\psi}_{\chi_1^0}\psi_{\chi_1^0} + \frac{1}{2}\lambda^h h\overline{\psi}_{\chi_1^0}\psi_{\chi_1^0} + \lambda^Z Z_\mu\overline{\psi}_{\chi_1^0}\gamma^\mu P_L\psi_{\chi_1^0}\,, \tag{4.17}$$

where

$$\lambda^h \equiv \lambda^h_{L11} + \lambda^h_{R11} = -g'\left(O_n\right)_{11}\left(c_\alpha\left(O_n\right)_{13} + s_\alpha\left(O_n\right)_{12}\right)\,, \tag{4.18}$$

$$\lambda^Z \equiv \lambda^Z_{L11} = \frac{e}{s_{2W}}\left(\left(\left(O_n\right)_{13}\right)^2 - \left(\left(O_n\right)_{12}\right)^2\right)\,. \tag{4.19}$$

Note that $\lambda^h_{L11} = \lambda^h_{R11}, \epsilon_1 = 1$. See also Eq. (4.8) and Eq.(4.9)–(4.13). We can expand these couplings by z as

$$\lambda^h = \frac{1}{2} g' z \frac{1}{1-z_1^2}\left(z_1 + s_{2\beta}\right) + \mathcal{O}\left(z^3\right)\,, \tag{4.20}$$

$$\lambda^Z = \frac{e}{s_{2W}} c_{2\beta} z^2 \frac{1}{1-z_1^2} + \mathcal{O}\left(z^4\right)\,. \tag{4.21}$$

(see also Appendix C). The relic abundance, the SI/SD scattering cross section and the Higgs/Z invisible decay width are all determined only by these mass and couplings.

Let us briefly discuss the thermal relic abundance. Since the pure Bino DM is overabundant, it should mix with the Higgsino and the annihilation cross section should be increased. As we can see from Eq. (4.6), the Bino mixes with the Higgsino with the mixing size $\sim M_Z/\mu$. It makes possible for the DM to couple with the Higgs boson and the Z boson. The DM can annihilate to the SM particles only via these bosons. However, as shown in Eq. (4.20) and (4.21), the couplings are small when $|\mu| \gg M_1, M_Z$ holds and they are not sufficiently large to increase the annihilation cross section. Meanwhile, when the mass of the DM is half of the Higgs boson mass or the Z boson mass, the annihilation cross section can be also increased drastically by the resonant enhancement. With non-zero couplings (Eq. (4.20) and (4.21)), this resonant enhancement works well. This is the main feature of the Bino-Higgsino model with resonant annihilation. We will see the detailed calculations in Sec. 5.1 and the results in Sec. 6.1.

In the region with the Higgs resonance $m_{\chi_1^0} \sim m_h/2$ and the Z resonance $m_{\chi_1^0} \sim M_Z/2$, the current relic abundance can be explained. However, as we can see in Eq. (4.20), the DM-DM-Higgs coupling vanishes when the following relation holds:

$$M_1 \simeq -\mu s_{2\beta}\,. \tag{4.22}$$

This is called as the blind spot [38]. In this region, the annihilation cross section of the DM becomes too small even when the resonant annihilation occurs $m_{\chi_1^0} \sim m_h/2$. Thus the current relic abundance can not be explained when $\mu < 0$, $m_{\chi_1^0} \sim m_h/2$ and Eq. (4.22) hold. This gives very interesting phenomena. Especially, since even in the blind spot region the DM-DM-Z coupling λ^Z does not vanish, the combination of the experiments becomes important to cover these region. We will see these in Chapter 5 and 6.

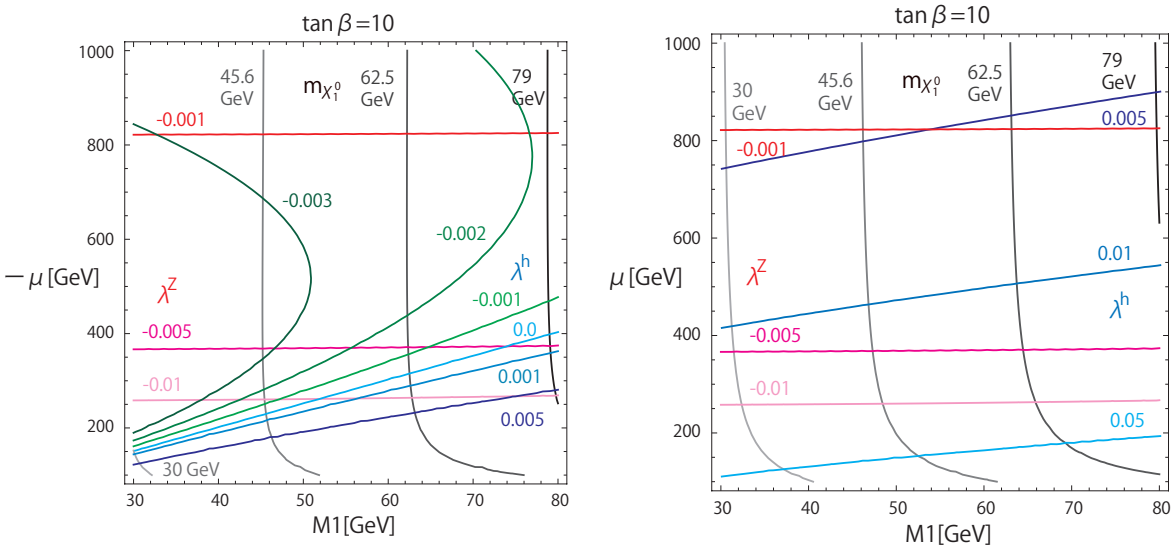

Figure 4.2: The behaviors of the mass and the couplings are shown. The values of $\tan\beta = 10$ are shown with $\mu < 0$ (left) and $\mu >$ (right). The black lines denote the mass of the lightest neutralino or the mass of the DM $m_{\chi_1^0}$. The lines with $m_{\chi_1^0} = 30, 45.6 \simeq M_Z/2, 62.5 \simeq m_h/2, 79$ GeV are shown. The blue and green lines denote the size of the DM-DM-Higgs coupling λ^h. Note that the sign of λ^h changes in $\mu < 0$ region. The size of the DM-DM-Z coupling λ^Z is also shown in the red lines.

We show the behaviors of the mass and the couplings in Figure 4.2. The mass and the couplings are calculated by solving the equations in Sec. 4.2 and we do not assume any approximations like $|\mu| \gg M_1, M_Z$. The black lines denote the mass of the lightest neutralino or the mass of the DM $m_{\chi_1^0}$. The lines with $m_{\chi_1^0} = 45.6$ GeV $\simeq M_Z/2$ and 62.5 GeV $\simeq m_h/2$ are shown. The blue and green lines denote the size of the DM-DM-Higgs coupling λ^h. The size of the DM-DM-Z coupling λ^Z is also shown in the red lines. Although the behavior of the $\tan\beta = 10$ case is shown, other value of $\tan\beta$ gives similar results. Note that in the $\mu < 0$ plane, the blind spot $\lambda^h \sim 0$ is clearly seen. The behavior of λ^h depends on the sign of μ drastically. On the other hand, the behavior of λ^Z does not depend on the sign of μ and M_1. It is easily understood by Eq. (4.21). In addition, λ^Z does not depend on $\tan\beta$ so much as far as $\tan\beta \gtrsim 2$. In our setup, $|\lambda^Z|$ becomes maximum $\lambda^Z = -0.0775$ at $M_1 = 80$ GeV, $\mu = -100$ GeV and $\tan\beta = 2$, i.e.

$$-0.078 < \lambda^Z < 0\,. \tag{4.23}$$

4.5 Heavy Neutralinos and Chargino

Here, we see the branching ratios and the couplings of the heavy neutralinos and the chargino. These are important in the LHC analyses. Especially, since the LHC phenomenology does not

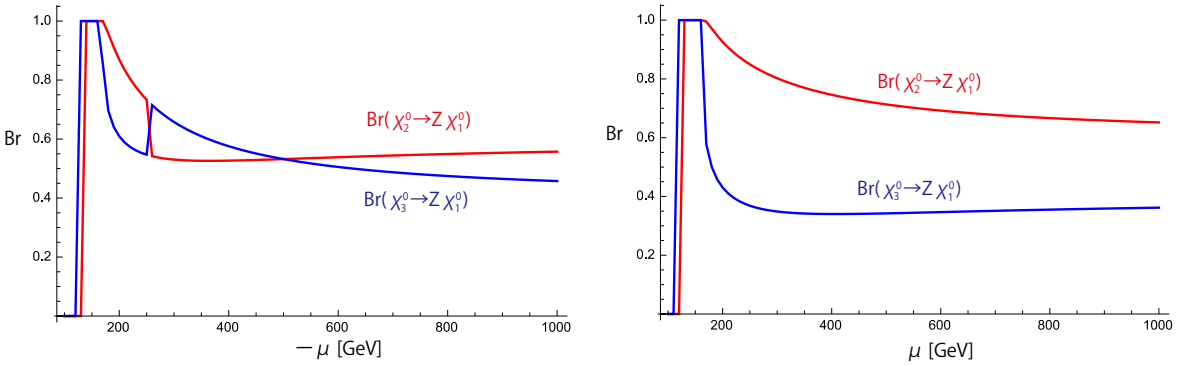

Figure 4.3: The branching ratios of the heavy neutralinos are shown (left: $\mu < 0$, right:$\mu > 0$). The red line shows $\mathrm{Br}(\chi^0_2 \to Z\chi^0_1)$ and the blue line shows $\mathrm{Br}(\chi^0_3 \to Z\chi^0_1)$. Here, we set $M_1 = 50$ GeV and $\tan\beta = 10$ for an example.

depend on λ^h and λ^Z, the LHC can shed a light even on the blind spot.

First, let us see the decays of the heavy neutralinos and the chargino. The chargino decays to the DM and the W boson exclusively when $m_{\chi^\pm_1} > m_{\chi^0_1} + M_W$. On the other hand, the heavy neutralinos can decay with two processes depending on their mass.

$$\chi^0_{2,3} \to Z\chi^0_1\,, \qquad \text{for } m_{\chi^0_{2,3}} > m_{\chi^0_1} + M_Z\,, \tag{4.24}$$

$$\chi^0_{2,3} \to Z\chi^0_1 \text{ and } \chi^0_{2,3} \to h\chi^0_1\,, \quad \text{for } m_{\chi^0_{2,3}} > m_{\chi^0_1} + m_h\,. \tag{4.25}$$

The decay widths of these particles are shown in Appendix C.4. We can see that the widths are narrow.

The branching ratios of the heavy neutralinos are important in the LHC analyses since the results depend on the final states. The branching ratio of the process $\chi^0_{2,3} \to Z\chi^0_1$ becomes as (Appendix C.4)

$$\mathrm{Br}(\chi^0_{2,3} \to Z\chi^0_1) = 1.0\,, \qquad \text{for } m_{\chi^0_1} + m_h > m_{\chi^0_{2,3}} > m_{\chi^0_1} + M_Z\,, \tag{4.26}$$

$$= \frac{1}{2}(1 \pm z_1)^2(1 \pm s_{2\beta})\frac{1}{1 + 2z_1 s_{2\beta} + z_1^2} + \mathcal{O}(z^2)\,, \quad \text{for } m_{\chi^0_{2,3}} > m_{\chi^0_1} + m_h\,. \tag{4.27}$$

Note that the following relation is satisfied

$$\mathrm{Br}(\chi^0_2 \to Z\chi^0_1) + \mathrm{Br}(\chi^0_3 \to Z\chi^0_1) = 1 + \mathcal{O}(z^2)\,, \quad \text{for } m_{\chi^0_{2,3}} > m_{\chi^0_1} + m_h\,. \tag{4.28}$$

The typical behavior of the branching ratio is shown in Figure 4.3. Here, we set $M_1 = 50$ GeV and $\tan\beta = 10$ for an example. We can see that the branching ratio of the process $\chi_{2,3} \to Z\chi^0_1$ is 1 for $m_{\chi^0_1} + m_h > m_{\chi^0_{2,3}} > m_{\chi^0_1} + M_Z$. In the $\mu < 0$ case, the flip occurs at $\mu \sim -225$GeV (see also Sec. 4.4). If we draw the graph with $\chi^0_{p,m}$ instead of $\chi^0_{2,3}$, the lines become continuos.

Next, let us see the couplings. The couplings and their z expansions are shown in Appendix C.3. As we can see in Sec. 3.4.2 and 5.5, the following processes are important.

$$pp \to W^{\pm} \to \chi^0_{2,3}\chi^{\pm}_1 \to Z\chi^0_1 W^{\pm}\chi^0_1 \,. \tag{4.29}$$

The production, $pp \to W^{\pm} \to \chi^0_{2,3}\chi^{\pm}_1$, depends on the couplings λ^W_{L1j}, λ^W_{R1j} where $j = 2, 3$. However, as we can see in Eq. (C.40)–(C.43), these couplings are almost constants. In the decay of the chargino, $\chi^{\pm}_1 \to W^{\pm}\chi^0_1$, the corresponding couplings λ^W_{L11} and λ^W_{R11} can be converted to the decay width $\Gamma_{\chi^{\pm}_1}$ and the ratio $\lambda^W_{L11}/\lambda^W_{R11}$. Although the width depends on mainly μ, the width is already narrow enough and the value does not change the LHC phenomenology. On the other hand, the ratio depend on $\tan\beta$ as we can see from Eq. (C.38) and (C.39). This may change the chirality of the produced W boson. In the decay of the heavy neutralino, $\chi^0_{2,3} \to Z\chi^0_1$, the related couplings are only $\lambda^Z_{L12,L13}$. These couplings can be converted to the decay widths $\Gamma_{\chi^0_{2,3}}$. The width do not affect the LHC phenomenology as same as the chargino case. The chirality of the produced Z boson also does not change since they have only left handed couplings. The detailed analysis is shown in Sec. 5.5.

Chapter 5

Analysis

In this section, we investigate the phenomenology of the Bino-Higgsino resonant DM model introduced in Chapter 4. We consider the thermal relic abundance, the SI scattering cross section, the SD scattering cross section, the invisible decays, the LHC searches, the mono-photon/jet searches and the indirect searches. We show the detailed studies of these phenomena to investigate this model comprehensively. We summarize the analyses and the experimental results considered in this thesis in Table 5.1. The SM values used in our analysis are given in Appendix A. In our analysis, we assume the standard halo model for the DM [88, 89]: the local density ρ_0 =0.3 GeVcm^{-3}, the local velocity $v_0 = 220\text{kms}^{-1}$ and the galactic escape velocity $v_{\text{esc}} = 544\text{kms}^{-1}$.

Before going to the detailed studies, we show the dependences of each phenomenon on the masses and couplings in Table 5.2. Although the relic abundance and the invisible decays seem to depend on both of λ^h and λ^Z in this table, actually they depend on only one of λ^h and λ^Z in each Higgs or Z region: the relic abundance in the Higgs (Z) resonant region depends on only λ^h (λ^Z) and the invisible decay of the Higgs (Z) boson depends on only λ^h (λ^Z). Since each phenomenon depends on different combination of the masses and couplings, study of these phenomenology can reveal this model comprehensively. Especially, the blind spot where $\lambda^h \sim 0$ holds exhibits interesting behaviors.

relic abundance (Sec. 5.1)	
Planck result	Ωh^2 =0.120 [19]
SI scattering cross section (Sec. 5.2)	
LUX constraints	left figure of Figure 3.2 [40]
XENON 1T prospects	right figure of Figure 3.2 [41]
SD scattering cross section (Sec. 5.3)	
XENON100 constraints	left figure of Figure 3.3 [42]
XENON 1T prospects	right figure of Figure 3.3 [43]
Higgs invisible decay (Sec. 5.4)	
global fit constraints	$\mathrm{Br}(h \to \chi_1^0\chi_1^0) < 0.19$ [45]
(HL) LHC prospects	$\mathrm{Br}(h \to \chi_1^0\chi_1^0) < 0.062$ [46]
ILC prospects	$\mathrm{Br}(h \to \chi_1^0\chi_1^0) < 0.004$ [48]
Z invisible decay (Sec. 5.4)	
LEP constraints	$\Gamma(Z \to \chi_1^0\chi_1^0) < 2.0$ MeV [49]
LHC chargino/neutralino search (Sec. 5.5)	
8 TeV constraints	reinterpretation of left figure of Figure 3.6 [50]
14 TeV prospects	reinterpretation of right figure of Figure 3.6 [51]
mono-photon search (Sec. 5.6)	
LEP constraints	Figure 3.4 [81]
mono-jet search (Sec. 5.6)	
CMS constraints	$\lvert\lambda^Z\rvert < 0.2$–$0.6$ [80] (Sec. 3.4.1)
cosmic rays (Sec. 5.6)	
Fermi-LAT constraints	Figure 3.7 [85]
DM annihilation in the Sun (Sec. 5.6)	
Super-Kamiokande constraints	Figure 3.8 [86]

Table 5.1: The analyses and the results used to set the constraints and estimate the future prospects are summarized.

	$m_{\chi_1^0}$	λ^h	λ^Z	heavy neutralinos/charginos
relic abundance (Sec. 5.1)	∘	∘	∘	−
SI scattering (Sec. 5.2)	∘	∘	−	−
SD scattering (Sec. 5.3)	∘	−	∘	−
invisible decays (Sec. 5.4)	∘	∘	∘	−
LHC productions (Sec. 5.5)	∘	−	−	∘

Table 5.2: The dependences of each phenomenon on the masses and couplings are shown. ∘ denotes that the phenomenon depends on the mass or couplings, and − denotes that it does not depend on them. "heavy neutralinos/charginos" includes the masses of the heavy neutralinos and charginos $m_{\chi^0_{2,3}}, m_{\chi^\pm_1}$ and the couplings which related to them like λ^h_{Lij} where $i \geq 2$ or (and) $j \geq 2$ (see also Sec. 4.5).

5.1 Relic Abundance

First, we calculate the thermal relic abundance of the Bino-Higgsino resonant DM. Since the DM couples only with the Higgs boson and the Z boson (see Eq. (4.8) and (4.17)), the DM can annihilate to the SM particles only through the Higgs boson and the Z boson as shown in Figure 5.1. The annihilation cross section of the DM, $\sigma^{\text{ann.}}(s)$, is calculated as

$$\begin{aligned}\sigma^{\text{ann.}}(s) &= \sigma(\chi_1^0\chi_1^0 \to \text{SM particles})(s) \\ &= \sum_f \sigma(\chi_1^0\chi_1^0 \to h \to f)(s) + \sum_f \sigma(\chi_1^0\chi_1^0 \to Z \to f)(s)\,, \end{aligned} \tag{5.1}$$

where f denotes possible final states and

$$\sigma(\chi_1^0\chi_1^0 \to h \to f)(s) \simeq \frac{1}{2}(\lambda^h)^2\sqrt{1-\frac{4m_{\chi_1^0}^2}{s}}\frac{1}{(s-m_h^2)^2+(m_h\Gamma_h)^2}\frac{s}{m_h}\Gamma(h\to f)\,, \tag{5.2}$$

$$\sigma(\chi_1^0\chi_1^0 \to Z \to f)(s) \simeq (\lambda^Z)^2\sqrt{1-\frac{4m_{\chi_1^0}^2}{s}}\frac{1}{(s-M_Z^2)^2+(M_Z\Gamma_Z)^2}\frac{s}{M_Z}\Gamma(Z\to f)\,. \tag{5.3}$$

s denotes the squared center of mass energy. Γ_h (Γ_Z) is the total decay width of the Higgs (Z) boson and $\Gamma(h(Z)\to f)$ is the partial decay width of the process $h(Z)\to f$. Here, we neglect the SM fermion mass terms which is proportional to $(m_f/m_{\chi_1^0})^2 \ll 1$. The detailed calculations are written in Appendix D.1. Note that there is no interference term since the Higgs boson and the Z boson have different spins. Then with summing all the possible final states, the annihilation cross section can be written as

$$\begin{aligned}\sigma^{\text{ann.}}(s) &= \frac{1}{2}(\lambda^h)^2\sqrt{1-\frac{4m_{\chi_1^0}^2}{s}}\frac{1}{(s-m_h^2)^2+(m_h\Gamma_h)^2}\frac{s}{m_h}\Gamma_h \\ &\quad +(\lambda^Z)^2\sqrt{1-\frac{4m_{\chi_1^0}^2}{s}}\frac{1}{(s-M_Z^2)^2+(M_Z\Gamma_Z)^2}\frac{s}{M_Z}\Gamma_Z\,. \end{aligned} \tag{5.4}$$

As described in the previous chapters, the resonant annihilation is important since the DM's couplings with the SM particles are not large enough. That is, typical size of the annihilation cross section $\sigma^{\text{ann.}}(s)$ is small except the resonant region. As we can see from Eq. (5.4), when $s \sim m_h^2$ or $s \sim M_Z^2$ is satisfied, the annihilation cross section is enhanced drastically. We show this behavior in Figure 5.2. The left figure corresponds to the Higgs resonance with $\left(\lambda^h\right)^2 = 2m_h\Gamma_h$ and $\lambda^Z = 0$. The right figure corresponds to the Z resonance with $\left(\lambda^Z\right)^2 = m_Z\Gamma_Z$ and $\lambda^h = 0$. Although the actual annihilation cross section is determined by λ^h and λ^Z, the typical behavior becomes the sum of these resonances. The resonance condition $s \sim m_h^2, M_Z^2$ is satisfied especially for $m_{\chi_1^0} \sim m_h/2, M_Z/2$ respectively.

As we show in Sec. 3.1, the relic abundance of the DM is calculated by solving the Boltzmann equation (3.1). The relic abundance depends on $\langle\sigma v\rangle(T)$ i.e. $\sigma^{\text{ann.}}(s)$ strongly. Here, let us see the typical behavior of the thermal average of the annihilation cross section $\langle\sigma v\rangle(T)$ in the

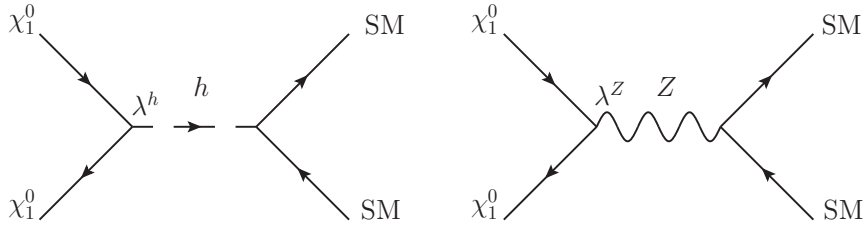

Figure 5.1: The diagrams which contribute to the annihilation cross section are shown. The Higgs boson exchange (left) and the Z boson exchange (right) are the only process where the DM χ_1^0 can annihilate to the SM particles.

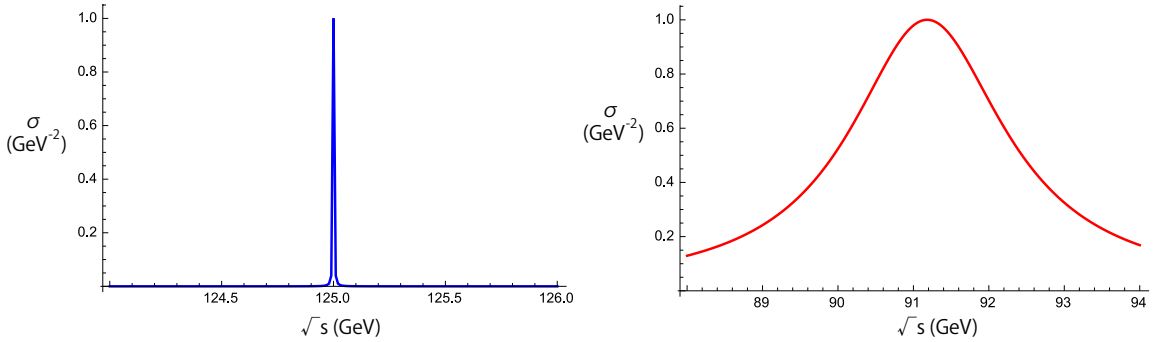

Figure 5.2: The annihilation cross sections with the Higgs resonance (left) and the Z resonance (right) are shown. Here, to exhibit the shape of the resonance, the couplings are set as follows: (left) $\left(\lambda^h\right)^2 = 2m_h\Gamma_h$ and $\lambda^Z = 0$, (right) $\left(\lambda^Z\right)^2 = m_Z\Gamma_Z$ and $\lambda^h = 0$.

resonant region. $\langle\sigma v\rangle(T)$ is calculated by Eq. (3.4) with Eq. (5.4). The behavior of $\langle\sigma v\rangle(T)$ is shown in Figure 5.3. When the mass is 60.0 GeV (the blue line in Figure 5.3) which is a little smaller than the half of the Higgs boson mass, $m_h/2 \simeq 62.5$ GeV, the thermal average of the annihilation cross section is enhanced at small $m/T \sim \mathcal{O}(10)$. This is because $s = 4(m_{\chi_1^0}^2 + p^2)$ can satisfy $s \sim m_h^2$ with sizable $p \sim 18$ GeV for $m_{\chi_1^0} = 60.0$ GeV where p is the DM momentum. When the mass goes near the half of the Higgs boson (the green/black line), $s \sim m_h^2$ can be satisfied only with small momentum. Thus, the temperature when the enhancement occurs goes lower, $m/T \sim \mathcal{O}(100)$. When the mass exceeds $m_h/2$ (the red line), obviously the enhancement disappears since $s \sim m_h^2$ can not be satisfied. The enhancement which occurs at $m/T \sim \mathcal{O}(10)$ is important to explain the current relic abundance.

The final relic abundance of the DM is calculated by solving the Boltzmann equation (3.1) using the annihilation cross section Eq. (5.4).[1] It depends on the mass of the DM, $m_{\chi_1^0}$, and the

[1]We have checked that the values of the relic abundance in our calculation agree with the values using micrOMEGAs [90–92] within a few % (micrOMEGAs is the public program which can calculate the relic abundance, the scattering cross sections, the annihilation cross sections and so on). In the calculation, as the value of the

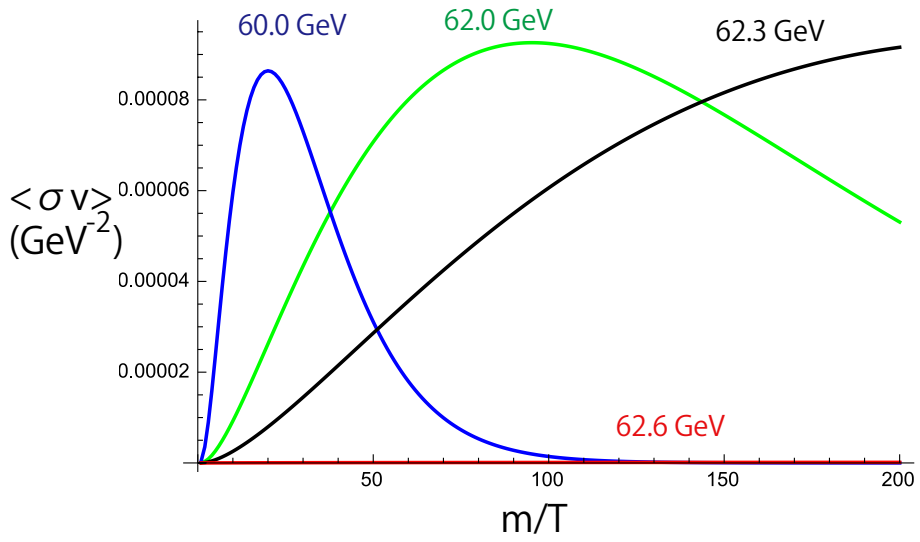

Figure 5.3: The thermal average of the annihilation cross sections is shown with changing the DM mass $m_{\chi_1^0}$. For simplicity, $\left(\lambda^h\right)^2 = 2m_h\Gamma_h$ and $\lambda^Z = 0$ are assumed.

couplings λ^h, λ^Z. We show the results where the current DM relic abundance Ωh^2 =0.120 [19] can be explained in Sec. 6.1.

5.2 Spin Independent Scattering

Here, we calculate the SI scattering cross section. It is constrained now and the future experiments are planed as shown in Sec. 3.2.1. In the Bino-Higgsino resonant model, the SI scattering cross section is determined only by the mass of the DM, $m_{\chi_1^0}$, and the coupling λ^h. This is because the process which contribute to the SI scatteing is only the Higgs boson exchange process which is shown in the left side of Figure 5.4.[2] The DM-DM-N-N coupling λ_N, $L \ni \sum_{N=p,n} \lambda_N \overline{\psi}_{\chi_1^0}\psi_{\chi_1^0}\overline{N}N$, can be calculated with λ^h by integrating out the Higgs boson as

$$\lambda_N = \frac{\lambda^h}{2\sqrt{2}m_h^2 v} m_N f_N \,. \tag{5.5}$$

Here,

$$f_N \;=\; \sum_{q=u,d,s} f_q^N + \frac{2}{9} f_g^N = \frac{2}{9} + \frac{7}{9} \sum_{q=u,d,s} f_q^N \,, \tag{5.6}$$

relativistic degrees of freedom g_s and g_ρ, we use the fitting formula in Ref. [93].

[2]The heavy SUSY particle (heavy Higgs or sfermion) exchange process can contribute to the SI scattering if their masses are relatively light $\sim$ a few TeV. Here, we assume they are heavy enough and do not consider their contributions.

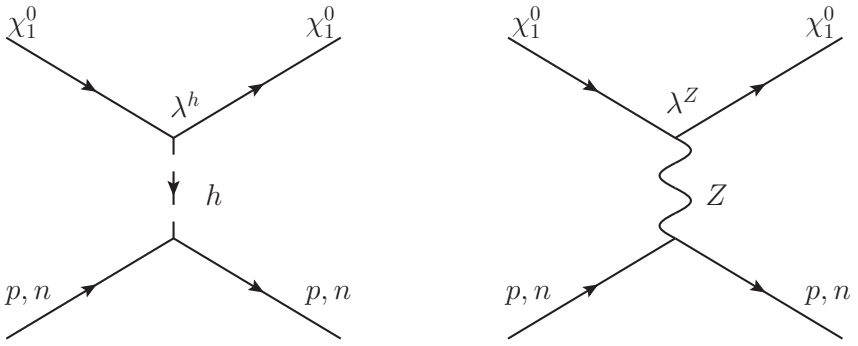

Figure 5.4: The diagrams which contribute to the scattering cross sections are shown. The Higgs boson exchange process (left) is sensitive only to the SI scattering cross section. The Z boson exchange process (right) corresponds only to the SD scattering cross section.

and

$$m_N f_q^N = \langle N|m_q \overline{\psi}_q \psi_q|N\rangle\,, \tag{5.7}$$

$$m_N f_g^N = -\frac{9\alpha_s}{8\pi}\langle N|G_{\mu\nu}G^{\mu\nu}|N\rangle\,. \tag{5.8}$$

See also Appendix D.2 for the detailed calculation.

The SI scattering cross section is calculated by Eq. (3.7) using the coupling Eq. (5.5). In our numerical analysis, we use $f_N = 0.284$. This is the default value used in micrOMEGAs [90–92] where $f_u^p = 0.0153$, $f_d^p = 0.0191$ and $f_s^p = 0.0447$. The value f_N changes a lot by choosing different values of f_s^p which are the results of the lattice simulations and can be $\mathcal{O}(0.1)$. Here, the value $f_s^p = 0.0447$ is the weighted mean value of the lattice results and it is already small. If we use the value $f_s^p \simeq 0.009$ in Ref. [94], f_N becomes $f_N \simeq 0.256$. Thus, the SI cross section may decrease up to 20%. If we use $f_N = 0.284$, the SI cross section becomes as

$$\sigma_N^{\rm SI} = 5.2 \times 10^{-43} \times (\lambda^h)^2 \frac{m_{\chi_1^0}^2}{(m_{\chi_1^0} + m_N)^2}\ [\mathrm{cm}^2]\,. \tag{5.9}$$

It depends on the coupling λ^h and slightly on the mass of the DM $m_{\chi_1^0}$. As a result, the SI scattering searches have no sensitivity in the blind spot region, $\lambda^h \sim 0$.

As the constraints, we use the LUX [40] results which give the strongest constraints now: $\mathcal{O}(10^{-45}$–$10^{-44})$ cm^2 (see left side of Figure 3.2). We also consider the future prospect of the XENON [41] which can reach up to $\mathcal{O}(10^{-47})$ cm^2 (see right side of Figure 3.2). The results are shown in Sec. 6.2.[3]

[3]We have checked that the SI scattering cross sections in our calculation agree with those in using micrOMEGAs [90–92] within a few %.

5.3 Spin Dependent Scattering

In contrast to the SI scattering cross section, the SD scattering cross section depends on the mass of the DM $m_{\chi_1^0}$ and the coupling λ^Z. This is because the process which contribute to the SD scattering is only the Z boson exchange process which is shown in the right side of Figure 5.4.[4] The SD scattering cross section is constrained and the future experiments are planed as shown in Sec. 3.2.2.

The DM-DM-N-N coupling ξ_N in this case, $L = \sum_{N=p,n} \xi_N \overline{\psi}_{\chi_1^0} \gamma^\mu \gamma_5 \psi_{\chi_1^0} \overline{N} \gamma_\mu \gamma_5 N$, can be calculated with λ^Z as

$$\xi_N = \frac{e\lambda^Z}{2 s_{2W} m_Z^2} \sum_{q=u,d,s} T_q^3 \Delta_q^N \,. \tag{5.10}$$

See also Appendix D.3 for the detailed calculation. The SD scattering cross section is calculated by Eq. (3.8) with Eq. (5.10). In our numerical analysis, we use the values used in micrOMEGAs [90–92], $\Delta_u^p = \Delta_d^n = 0.842$, $\Delta_d^p = \Delta_u^n = -0.427$, and $\Delta_s^p = \Delta_s^n = -0.085$. In this case, the sum becomes $\sum_q T_q^3 \Delta_q^{n(p)} = 0.677$ (-0.592). This value of $\Delta_s^p (\Delta_s^n)$ is determined by the HERMES experiments [95]. The value of $\Delta_s^{p,n}$ can be larger if we use the early experimental results of EMC and SMC [96]. In this case $\Delta_u^p = \Delta_d^n = 0.78$, $\Delta_d^p = \Delta_u^n = -0.48$, $\Delta_s^p = \Delta_s^n = -0.15$ [90] and the sum becomes $\sum_q T_q^3 \Delta_q^{n(p)} = 0.705$ (-0.555). Thus, the SD cross section may increase/decrease up to 10% for the proton/neutron respectively. Here, we use the latest values (former values) used in micrOMEGAs which leads to $\sum_q T_q^3 \Delta_q^{n(p)} = 0.677$ (-0.592). Then the cross section becomes as

$$\sigma_{n(p)}^{\rm SD} = 2.3\ (3.0) \times 10^{-37} \times (\lambda^Z)^2 \frac{m_{\chi_1^0}^2}{(m_{\chi_1^0} + m_N)^2}\ [\mathrm{cm}^2] \,. \tag{5.11}$$

Similarly to the SI scattering cross section, it depends on the coupling λ^Z and slightly on the mass of the DM $m_{\chi_1^0}$. However, since this does not depend on λ^h, the search for the SD scattering can cover even in the blind spot region, $\lambda^h \sim 0$.

The current constraints come from the XENON100 [42] and the estimated future prospects of the XENON 1T [43] are taken into account in our analysis. They reach up to $\mathcal{O}(10^{-40})$ cm^2 and $\mathcal{O}(10^{-41})$ cm^2 respectively (see Figure 3.2). The results are shown in Sec. 6.3.[5]

5.4 Invisible Decay

As shown in Sec. 3.3, when the mass of the DM is less than the half of the Higgs boson mass or the Z boson mass, the Higgs boson or (and) the Z boson can decay to the DMs. Especially,

[4] The heavy SUSY particle (heavy Higgs or sfermion) exchange process can contribute to the SD scattering cross section if their masses are relatively light $\sim$ a few TeV. Here, we assume they are heavy enough and do not consider their contributions.

[5] We have checked that the SD cross sections in our calculation agree with those in using micrOMEGAs [90–92] within a few %.

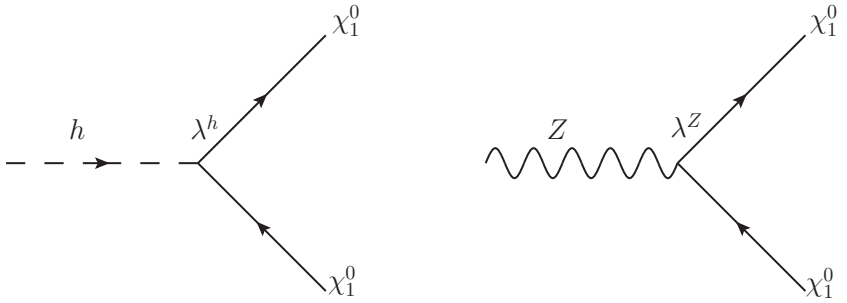

Figure 5.5: The diagrams which contribute to the invisible decays are shown. The Higgs boson decay (left) and the Z boson decay (right) can exist depending on the mass of the DM.

in our case, when $m_{\chi_1^0} \leq m_h/2 \simeq 62.5$ GeV, the Higgs boson can decay to two DMs and when $m_{\chi_1^0} \leq M_Z/2 \simeq 45.6$ GeV, not only the Higgs boson but also the Z boson can decay to two DMs. The diagrams which contribute to these invisible decays are shown in Figure 5.5. Obviously, both of these invisible decays depend on the mass of the DM $m_{\chi_1^0}$ and the Higgs (Z) boson invisible decay also depend on the coupling λ^h (λ^Z) respectively.

The decay width of the Higgs boson to the DMs can be calculated as

$$\Gamma(h \to \chi_1^0\chi_1^0) = \frac{(\lambda^h)^2}{16\pi} m_h \left(1 - \frac{4m_{\chi_1^0}^2}{m_h^2}\right)^{3/2}, \quad \text{for } m_{\chi_1^0} \leq \frac{1}{2} m_h \,. \tag{5.12}$$

The decay width of the process $Z \to \chi_1^0\chi_1^0$ is also calculated as

$$\Gamma(Z \to \chi_1^0\chi_1^0) = \frac{(\lambda^Z)^2}{24\pi} M_Z \left(1 - \frac{4m_{\chi_1^0}^2}{M_Z^2}\right)^{3/2}, \quad \text{for } m_{\chi_1^0} \leq \frac{1}{2} M_Z \,. \tag{5.13}$$

See also Appendix D.4.

For the Higgs boson invisible decay, the constraints and the future prospects are set on the branching ratio Br($h \to$ invisible). This branching ratio can be calculated from Eq. (3.9) with Eq. (5.12). To see the behavior we can write as

$$\begin{aligned} Br(h \to \text{invisible}) &= \frac{X}{1+X}, \quad \text{for } m_{\chi_1^0} \leq \frac{1}{2} m_h \,, \\ X &= \frac{\Gamma(h \to \chi_1^0\chi_1^0)}{\Gamma(h \to \text{SM})} = \left(\frac{1}{Br(h \to \chi_1^0\chi_1^0)} - 1\right)^{-1} \\ &\simeq \left(\frac{\lambda^h}{0.04}\right)^2 \left(1 - \left(\frac{m_{\chi_1^0}}{62.5 \text{ GeV}}\right)^2\right)^{3/2}, \end{aligned} \tag{5.14}$$

where we use $\Gamma(h \to \text{SM}) = 4.07 \times 10^{-3}$ GeV [63]. Here, we neglect the SM contribution $h \to ZZ^* \to \nu\nu\nu\nu$.[6] As the constraints, we use the results from the global fit [45]. In our setup,

[6] It does not change the results of the global fit constraints and the (HL) LHC prospects since Br($h \to ZZ^* \to \nu\nu\nu\nu$) $\simeq 0.001$. Although the result of the ILC prospects may change, we do not include this contribution for simplicity which leads conservative results.

the Higgs couplings to the SM particles become SM like as follows. The Higgs couplings to the gauge bosons normalized by the SM Higgs couplings are $\sin(\beta-\alpha)$. The Higgs couplings to the up (down) type fermions normalized by the SM Higgs couplings are $\cos\alpha/\sin\beta$ $(-\sin\alpha/\cos\beta)$. In our setup, these factors become 1 since the heavy Higgses are heavy enough, i.e. $\alpha \sim \beta - \pi/2$ (see Sec. 4.2). Thus, we use the global fit results $\mathrm{Br}(h \to \text{invisible}) < 0.19$ which is derived by assuming the Higgs couplings are same as the SM values (see also Sec. 3.3.1). This value corresponds to $X \lesssim 0.235$. As the future prospects, we consider the (HL) LHC [46] and the ILC [48]. As the future prospects from the (HL) LHC, we use the value $\mathrm{Br}(h \to \text{invisible}) < 0.062$ which is the "realistic scenario" for the systematic uncertainties. The sensitivity of the ILC is $\mathrm{Br}(h \to \text{invisible}) < 0.004$. These values correspond to $X \lesssim 0.066$ and $X \lesssim 0.004$ respectively. In our numerical analysis, we calculate the branching ratio and set the limits on it (not on X). The results are shown in Sec. 6.4.

For the Z invisible decay, the constraints are set on the decay width as shown in Sec. 3.3.2. From Eq. (5.13), the decay width of the process $Z \to \chi_1^0\chi_1^0$ can be written as

$$\Gamma(Z \to \chi_1^0\chi_1^0) \simeq \left(\frac{\lambda^Z}{0.03}\right)^2 \left(1 - \left(\frac{m_{\chi_1^0}}{45.6\ \mathrm{GeV}}\right)^2\right)^{3/2} \mathrm{MeV}\,, \quad \text{for } m_{\chi_1^0} \leq \frac{1}{2}M_Z\,. \tag{5.15}$$

The constraints on the process $Z \to$ DM DM are calculated by subtracting the decay width to the neutrinos from the Z invisible decay width. The constraint becomes $\Gamma(Z \to \chi_1^0\chi_1^0) < 2.0$ MeV [49]. The results are shown in Sec. 6.4.

5.5 Heavy Neutralinos/Chargino Searches at the LHC

In our model, since the heavy neutralinos and the chargino are $\mathcal{O}(100)$ GeV, they can be produced at the LHC. As we can see in Sec. 3.4.2, the following process give the high sensitivity when all the other SUSY particles are heavy,

$$pp \to \chi_{2,3}^0\chi_1^\pm \to Z\chi_1^0 W^\pm\chi_1^0 \to ll\chi_1^0 l\nu\chi_1^0\,. \tag{5.16}$$

Note that l denotes the SM leptons e, μ, τ and ν denotes the neutrinos ν_e, ν_μ, ν_τ. The relevant diagram is shown in Figure 5.6. As the constraints, we reinterpret the ATLAS 8 TeV analysis which gives the strongest constraints [50]. We analyze the future prospects at 14 TeV given by the ATLAS [51].

As shown in Sec. 3.4.2, these ATLAS analyses assume the pure Bino-Wino model. In the Bino-Higgsino resonant model, there are several different points compared to this pure Bino-Wino model:

(i) There exist the Bino DM χ_1^0, two Higgsino neutralinos $\chi_{2,3}^0$ and the Higgsino chargino $\chi_1^\pm$, and the Bino and the neutral Higgsinos mix slightly.

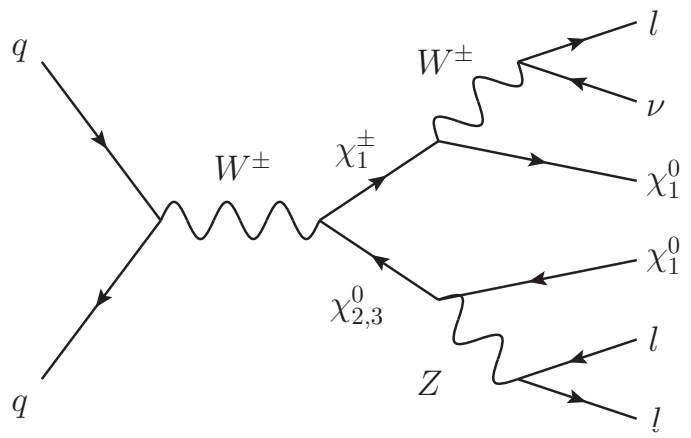

Figure 5.6: The diagrams which contribute to the neutralinos/chargino searches at the LHC are shown.

(ii) The masses of $\chi^0_{2,3}$ and $\chi^\pm_1$ are different, $m_{\chi^\pm_1} < m_{\chi^0_2} < m_{\chi^0_3}$. The differences become large especially when $|\mu|$ is small: e.g. at most 35 GeV for $|\mu|$ =100 GeV and 5 GeV for $|\mu| = 400$ GeV.

(iii) There are two processes of the heavy neutralinos decay, $\chi^0_{2,3} \to Z\chi^0_1$ and $\chi^0_{2,3} \to h\chi^0_1$, while the chargino decays as $\chi^\pm_1 \to W^\pm\chi^0_1$ with 100%, i.e. $\mathrm{Br}(\chi^0_{2,3} \to Z\chi^0_1) = \mathcal{O}(1)$, $\mathrm{Br}(\chi^0_{2,3} \to h\chi^0_1) = \mathcal{O}(1)$ and $\mathrm{Br}(\chi^\pm_1 \to W^\pm\chi^0_1)$=1.

These differences change the LHC phenomenology. First, the cross section σ changes as follows:

(a) The production cross section of the Higgsino is about a fourth of the pure Wino case, i.e. $\sigma(pp \to (\chi^0_2)_{\mathrm{Higgsino}}(\chi^\pm_1)_{\mathrm{Higgsino}}) \sim \frac{1}{4}\sigma(pp \to (\chi^0_2)_{\mathrm{Wino}}(\chi^\pm_1)_{\mathrm{Wino}})$ for the same mass since the Higgsino-W couplings is about half of the Wino-W coupling.

(b) There are two processes $pp \to \chi^0_2\chi^\pm_1$ and $pp \to \chi^0_3\chi^\pm_1$, and the sum of all the production cross sections $\sum_i \sigma(pp \to \chi^0_i\chi^\pm_1)$ becomes roughly a half of the pure Wino case.

(c) The cross section changes by the mass differences of $m_{\chi^\pm_1}, m_{\chi^0_2}, m_{\chi^0_3}$ especially for small $|\mu|$: for example, $\sigma(pp \to \chi^0_2\chi^\pm_1) > \sigma(pp \to \chi^0_3\chi^\pm_1)$ and $\sigma(pp \to \chi^0_2\chi^\pm_1)|_{m_{\chi^0_2}=m_{\chi^\pm_1}} > \sigma(pp \to \chi^0_2\chi^\pm_1)|_{m_{\chi^0_2}>m_{\chi^\pm_1}}$ for the same $m_{\chi^\pm_1}$ and the same couplings.

(d) The branching ratio with $\mathrm{Br}(\chi^0_{2,3} \to Z\chi^0_1) \leq 1$ decreases the relevant cross sections for the process (5.16).

In addition, the acceptance A (the efficiency of the cut, see Eq. (5.18)) also changes:

(e) The acceptance depends on the masses not only $m_{\chi^\pm_1}, m_{\chi^0_2}, m_{\chi^0_3}$ but also $m_{\chi^0_1}$, i.e. in the two parameter points which give the same cross section but the different masses, the acceptances are not the same.

(f) The acceptance changes by the mass differences of $m_{\chi_1^\pm}, m_{\chi_2^0}, m_{\chi_3^0}$ especially for small $|\mu|$: for example $A|_{m_{\chi_2^0}=m_{\chi_1^\pm}} \neq A|_{m_{\chi_2^0}>m_{\chi_1^\pm}}$ for the same $m_{\chi_1^\pm}$ and the same couplings.

(g) The acceptances of $pp \to \chi_2^0\chi_1^\pm$ and $pp \to \chi_3^0\chi_1^\pm$ are different especially for small $|\mu|$ since the masses are different.

The differences (c), (f) and (g) can be seen only in the small $|\mu|$ region since the mass differences (difference (ii)) can be neglected in the large $|\mu|$ region. However, even in the large $|\mu|$ region, the rescale of the ATLAS results by the cross section gives wrong results due to the other differences (a), (b), (d) and (e). Thus, we can not apply the ATLAS results directly and the reinterpretations are necessary. In order to investigate the LHC analysis, we need to perform the simulations.

In the ATLAS analysis [50, 51], several signal regions (SRs) are defined by various kinematical cuts. The expected numbers of events for each SR are simulated in the SM. In the 8 TeV analysis [50], the observed numbers and these expected SM numbers are compared and the constraints are set on the numbers of events which are caused by the additional non-SM processes. For the 14 TeV prospects [51], the expected exclusion/discovery limits on the numbers of the non-SM process events are estimated. Thus, in order to reinterpret the ATLAS analysis, we simulate and obtain the expected numbers of events in the Bino-Higgsino resonant model and compare these numbers with the numbers of the ATLAS constraints and the prospects.

We investigate the process (5.16). Then the expected number of events for the SR X is calculated as

$$\begin{aligned} N_{\rm SRX} &= \sum_{j=2,3}\sum_{\chi^\pm} \sigma(pp \to \chi_j^0\chi_1^\pm) \times {\rm Br}(\chi_1^\pm \to W^{\pm(*)}\chi_1^0 \to l\nu\chi_1^0) \times {\rm Br}(\chi_j^0 \to Z^{(*)}\chi_1^0 \to ll\chi_1^0) \\ &\quad \times A_{\rm SRX} \times \int \mathcal{L}dt\,, \end{aligned} \tag{5.17}$$

where $\int \mathcal{L}dt$ denotes the integrated luminosity. $A_{\rm SRX}$ is the acceptance and defined by

$$A_{\rm SRX} = \frac{\#\text{ of events which pass the cuts of SR-X}}{\#\text{ of generated events in } pp \to \chi_j^0\chi_j^\pm \to W^{\pm(*)}\chi_1^0 Z^{(*)}\chi_1^0 \to l\nu\chi_1^0 ll\chi_1^0}\,. \tag{5.18}$$

Here, we consider only the leptonic decays of the W boson and the Z boson for simplicity since three leptons are needed in each events as we see in the definition of the SR X (see Sec. 5.5.1 and 5.5.2). The branching ratios are given by (when kinematically allowed)

$$\begin{aligned} {\rm Br}(\chi_1^\pm \to W^\pm\chi_1^0 \to l\nu\chi_1^0) &= {\rm Br}(\chi_1^\pm \to W^\pm\chi_1^0) \times {\rm Br}(W^\pm \to l\nu)\,, & (5.19)\\ {\rm Br}(\chi_j^0 \to Z\chi_1^0 \to ll\chi_1^0) &= {\rm Br}(\chi_j^0 \to Z\chi_1^0) \times {\rm Br}(Z \to ll)\,. & (5.20) \end{aligned}$$

Note that ${\rm Br}(\chi_1^\pm \to W^\pm\chi_1^0) = 1$. See also Sec. 4.5 for the branching ratio of the neutralinos and Appendix A for those of the W, Z bosons.

We also include other all possible processes like $pp \to \chi_2^0\chi_3^0, \chi_1^+\chi_1^-$ in the 8 TeV analysis for sample points shown in Sec. 6.5.1. Note that the cross sections with the conditions that the

final state contains more than two leptons, i.e. $\sigma(pp \to \chi\chi \to X)$ where X includes more than two leptons, for these processes are at most 10% of those of the process (5.16). However, since the $\mathcal{O}(10)$% differences are important in the 8 TeV case as shown in Sec. 6.5.1, we include and simulate their effects. In 14 TeV case, since $\mathcal{O}(10)$% differences do not change the result much as shown in Sec. 6.5.2, we do not include these processes due to the limitation of the machine power.

In the numerical calculations, we generate the events with MadGraph5_aMC@NLO 2.2.3 [97] in combination with PYTHIA 6.4 [98] at the leading order (LO). Delphes 3 [99] is used to simulate the detector effects. Then, the acceptance is calculated by applying the cuts. We calculate the cross section at the next-leading order (NLO) by Prospino 2.1 [100, 101] with CTEQ6L1 parton distribution functions [102]. We show the detailed analysis of 8 TeV and 14 TeV in Sec. 5.5.1 and 5.5.2 respectively.

5.5.1 8TeV

In the 8 TeV analysis [50], many SRs are considered depending on the target model. Among them, we consider the SR0τa, which is sensitive to the process (5.16). The SR0τa is composed of 20 disjoint bins, SR0τa1–SR0τa20 defined by different kinematical cuts. In these SRs, the following cuts are applied [50]. First, the candidates for the lepton and the jets are selected with the condition for the pseudorapidity η, azimuthal angle ϕ and the transverse momentum p_T. The electron, muon and hadronic decaying tau candidates are required as $|\eta| < 2.47, 2.5, 2.47$ and $p_T > 10$ GeV respectively. The jets candidates reconstructed with the anti-k_t algorithm [103] with $\Delta R = \sqrt{(\delta\phi)^2 + (\delta\eta)^2} = 0.4$ are required as $|\eta| < 2.5$ and $p_T > 20$ GeV. Here, the jets generated by the bottom quark are identified as bottom-tagged jet with 80% and the jets generated by the light quarks are miss-identified with 4%. The missing energy $E_T^{\rm miss}$ is calculated by the sum of p_T of all candidates and calorimeters. In order to remove double counting of the leptons and jets, the following cuts are performed: discard the smaller p_T electron if two electrons exist within $\Delta R < 0.1$, discard the jet which exists within $\Delta R < 0.2$ from an electron, discard the hadronic decaying tau which exists within $\Delta R < 0.2$ from an electron or a muon, discard the electron (muon) which exists within $\Delta R < 0.4$ from a jet, discard the jet which exists within $\Delta R < 0.2$ from a tau. Then the events are selected as follows:

- Exactly three isolated leptons with no taus are required.
- At least one pair of same flavor opposite sign (SFOS) leptons should exist. Among the SOFS pairs, the SOFS mass which is closest to the Z boson mass should be in the range defined in each SR, for example $m_{\rm SFOS} = 60$–81.2 GeV for SR0τa9–12 and $m_{\rm SFOS} = 81.2$–101.2 GeV for SR0τa13–16 (see Table 5.3).
- Events including the b-tagged jets are vetoed.
- The events are further divided into four bins depending on the missing transverse energy

$E_T^{\rm miss}$ and the transverse mass m_T, where m_T is calculated with missing energy and the lepton which does not form the SFOS lepton pair whose mass is closest to the Z boson mass (see Table 5.3). For example $E_T^{\rm miss}$ $\geq$90 GeV and m_T =0–110 GeV for SR0τa14, $E_T^{\rm miss}$ =50–135 GeV and m_T $\geq$110 GeV for SR0τa15 and $E_T^{\rm miss}$ $\geq$135 GeV and m_T =$\geq$110 GeV for SR0τa16.

- In some SRs (SR0τa5, SR0τa13, SR0τa19), additional requirement on the trilepton mass, $|m_{3l} - M_Z| > 10$ GeV, is applied (see Table 5.3).

Note that $m_T^2 = 2p_T^l E_T(1 - \cos\Delta\phi)$ where $\Delta\phi$ is the angle between the lepton and the missing transverse energy.

SR	$m_{\rm SFOS}$	m_T	$E_T^{\rm miss}$	$3l$ mass
SR0τa1	12–40	0–80	50–90	no
SR0τa2	12–40	0–80	> 90	no
SR0τa3	12–40	> 80	50–75	no
SR0τa4	12–40	> 80	> 75	no
SR0τa5	40–60	0–80	50–75	yes
SR0τa6	40–60	0–80	> 75	no
SR0τa7	40–60	> 80	50–135	no
SR0τa8	40–60	> 80	> 135	no
SR0τa9	60–81.2	0–80	50–75	yes
SR0τa10	60–81.2	> 80	50–75	no
SR0τa11	60–81.2	0–110	> 75	no
SR0τa12	60–81.2	> 110	> 75	no
SR0τa13	81.2–101.2	0–110	50–90	yes
SR0τa14	81.2–101.2	0–110	> 90	no
SR0τa15	81.2–101.2	> 110	50–135	no
SR0τa16	81.2–101.2	> 110	> 135	no
SR0τa17	> 101.2	0–180	50–210	no
SR0τa18	> 101.2	> 180	50–210	no
SR0τa19	> 101.2	0–120	> 210	no
SR0τa20	> 101.2	> 120	> 210	no

Table 5.3: The definition of the SRs for the 8 TeV analysis are shown. In all SRs, the requirement of three isolated leptons with no taus and the veto of including the b-tagged jets are also imposed. The all values are shown in units of GeV.

To analyze these cuts, we use the CheckMATE program [104] in the 8 TeV analysis.[7] The validation of our analysis is shown in Appendix E.1. We simulate this analysis in all the param-

[7] CheckMATE uses Delphes 3 [99], FastJet [105, 106], and the anti-k_T jet algorithm [103].

eter space. However, since the machine power is limited and not enough, we simulate as follows. We calculate the cross sections and the acceptance for $100 \leq |\mu| \leq 400$ GeV since for $|\mu| > 400$ GeV the constraints are not sensitive due to the small cross sections. We take 31 sample points for $|\mu|$ per 10 GeV, i.e. $|\mu| = 100, 110, 120, \cdots, 400$ GeV. For each $|\mu|$, the sample points for other parameters are taken as follows. Cross sections : For each $|\mu| \leq 200$ GeV, we take $6 \times 2 \times 3 = 36$ sample points as the combination of $M_1 = 30, 40, \cdots, 80$ GeV, $\mathrm{sign}(\mu) = \pm$ and $\tan\beta = 2, 5, 50$. For each $|\mu| \geq 200$ GeV, we take 2 sample points as $(M_1, \mathrm{sign}(\mu), \tan\beta) = (80$ GeV, +,2) and (30 GeV,+,50). From these sample points, for each $|\mu|$,we can get two dimensional data sets $\{(m_{\chi_j^0} - m_{\chi_1^\pm}, \sigma)\}$ where $j = 2, 3$.[8] Note that $m_{\chi_1^\pm} = |\mu|$. Next, we calculate the cross sections normalized by the couplings, $\sigma' = \sigma/(|(O_n)_{j2}|^2 + |(O_n)_{j3}|^2)$, and the data sets $\{(m_{\chi_j^0} - m_{\chi_1^\pm}, \sigma')\}$ are obtained (See Figure 5.7.). We make the interpolated function of σ' as the function of $m_{\chi_j^0} - m_{\chi_1^\pm}$ for each $|\mu|$. Then, the cross section σ' for the points with $M_1 = 30, 35, 40, \cdots, 80$ GeV, $\mathrm{sign}(\mu) = \pm$ and $\tan\beta = 2, 3, 4, \cdots, 50$ are calculated with the interpolated function. Then the cross section is obtained by $\sigma = \sigma' \times (|(O_n)_{j2}|^2 + |(O_n)_{j3}|^2)$. Since the normalized cross sections σ' depend almost only on the masses $m_{\chi_{2,3}^0}, m_{\chi_1^\pm}$ as we see in Sec. 4.5, this approximation give good accuracy, at most $\sim 5\%$ errors for small $|\mu|$. Acceptance: we calculate the acceptances with changing the masses $m_{\chi_1^0}, m_{\chi_{2,3}^0}$ while keeping the couplings as the fixed values of $M_1 = 50$ GeV, $\mu = 200$ GeV, $\tan\beta$=5. This is because the acceptances depend almost on the masses as discussed in Sec. 4.5 and the simulation needs much machine power and times. We have checked that actually the differences of the couplings in our current setup does not change the acceptance.[9] Thus, we calculate the acceptances with changing $m_{\chi_1^0}, m_{\chi_{2,3}^0}$. The sample points are taken as $m_{\chi_j^0} - m_{\chi_1^\pm} = 0, 10, \cdots, \max(m_{\chi_j^0} - m_{\chi_1^\pm})$ GeV and $m_{\chi_1^0} = 30, 35, 40, \cdots, 80$ GeV. We make the interpolation function of acceptance as the function of $(m_{\chi_j^0} - m_{\chi_1^\pm}, m_{\chi_1^0})$. Then, the acceptances for the points with $M_1 = 30, 35, 40, \cdots, 80$ GeV, $\mathrm{sign}(\mu) = \pm$ and $\tan\beta = 2, 3, 4, \cdots, 50$ are calculated with the interpolated function. Finally, the number of events are calculated by Eq. (5.17). The results are shown in Sec. 6.5.1.

5.5.2 14TeV

Here, we investigate the future prospects of the LHC at 14 TeV. In the ATLAS analysis [51], there are three (four) SRs for 300 (3000) fb^{-1}, denoted as SRA–SRC (SRA–SRD). The cuts are

[8] The above sample points $(M_1, \mathrm{sign}(\mu), \tan\beta) = (80$ GeV, +, 2), (30 GeV,+,50) are taken because the calculations of these points give the smallest value of $m_{\chi_2^0} - m_{\chi_1^\pm}$ and largest value of $m_{\chi_3^0} - m_{\chi_1^\pm}$ for given $|\mu|$.

[9] We have calculated the acceptance with randomly changing the couplings while the masses are fixed. We have changed the couplings within the values which can be realized in our setup. We have checked with 4×10 sample points where 4 sample points for the fixed masses and 10 sample points for changing the couplings are taken into account. As a result, the acceptances for each fixed mass point agree within the statistical uncertainties of the Monte-Carlo events. Note that although the acceptance does not change when we change the couplings within the values realized in our setup, if we take the extreme value of the ratio $\lambda^W_{L11}/\lambda^W_{R11}$ such as $\ll -1$ or $\gg 1$, the acceptances changes a lot (in our case, $\lambda^W_{L11}/\lambda^W_{R11} \sim \mathcal{O}(0.1)$). Thus, the chirality of the chargino decay is important and we should include the spin correlations for the decays properly (we did in our simulation).

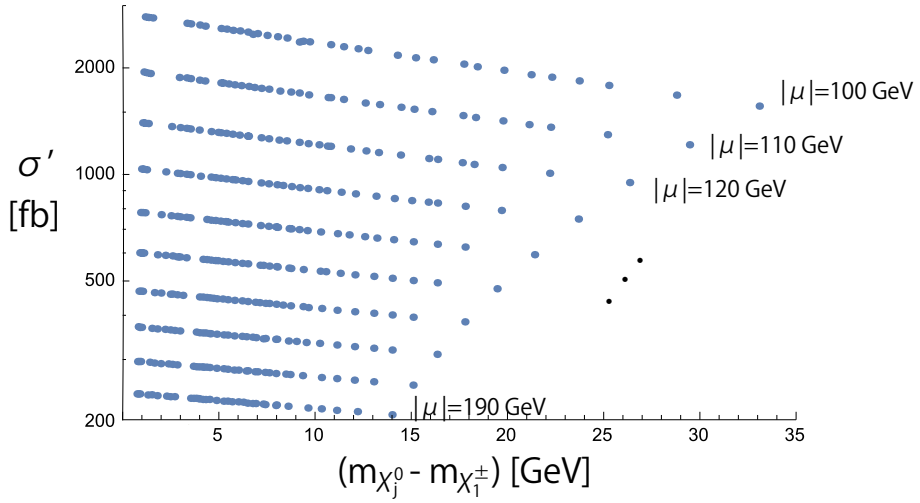

Figure 5.7: The cross sections normalized by the couplings for the heavy neutralinos/chargino productions are shown. The cross sections is normalized by the couplings, $\sigma' = \sigma/(|(O_n)_{j2}|^2 + |(O_n)_{j3}|^2)$. Each set of the alined points denotes the results with fixing the value of $|\mu|$. Here, for simplicity we show the results with $|\mu| = 100, 110, \cdots, 190$ GeV.

similar with the 8 TeV analysis. First, the candidates for the electrons (muons) are selected as $|\eta| < 2.47(2.4)$ and $p_T > 10$ GeV. The jets reconstructed with the anti-k_t algorithm with $\Delta R = \sqrt{(\delta\phi)^2 + (\delta\eta)^2} = 0.4$ are required as $|\eta| < 2.5$ and $p_T > 20$ GeV. The bottom tagging efficiency is 80% and the miss-identification rate is 1% for the light quarks. In order to remove double counting of the leptons and jets, the following cuts are imposed: discard the jet which exists within $\Delta R < 0.2$ from an electron, discard the leptons which form SFOS mass $m_{\rm SFOS} < 12$ GeV, discard the lepton if it is not isolated i.e. the sum of the transverse momentum of the track within $\Delta R < 0.3$ around the lepton should be < 15 %, discard the two leptons which exist within $\Delta R < 0.1$ from each other, discard the lepton which exists within $\Delta R < 0.4$ from a jet. Then the following cuts are applied.

- There should be exactly three leptons in each event, and at least one SFOS lepton pair is required to have invariant mass $|m_{\rm SFOS} - M_Z| < 10$ GeV.
- Events with b-tagged jets are discarded.
- The p_T of three leptons should be larger than 50 GeV.
- Then, the events are divided into SRs depending on the missing transverse energy $E_T^{\rm miss}$ and the transverse mass m_T, where m_T is calculated with the missing transverse energy and the lepton which does not form the SFOS lepton pair whose mass is closest to the Z boson mass (see Table. 5.4).

We analyze these cuts by our original code. The validation of our analysis is shown in Appendix E.2.

cut	SRA	SRB	SRC	SRD
$m_{\rm SFOS}$	81.2–101.2			
# of b-tagged jets	0			
lepton p_T	> 50			
$E_T^{\rm miss}$	> 250	> 300	> 400	> 500
m_T	> 150	> 200	> 200	> 200

Table 5.4: The definition of the SRs for the 14 TeV analysis are shown. The lepton p_T cut is imposed on all three leptons. The all values except the number (#) of b-tagged jets are shown in units of GeV. SRD is considered only in 3000 fb^{-1} analysis.

In the ATLAS analysis [51], the expected 95% exclusion limit is calculated by combining the disjoint SRs. The disjoint SRs (we denote this as SR dis. X) are defined in order to make each SR independent:

$$\begin{aligned} \text{SR dis. D} &= \text{SR D}\,, \\ \text{SR dis. C} &= \text{SR C} - \text{SR D}\,, \\ \text{SR dis. B} &= \text{SR B} - \text{SR C}\,, \\ \text{SR dis. A} &= \text{SR A} - \text{SR B}\,. \end{aligned} \tag{5.21}$$

Here subtraction is in the sense of the set theory. In our analysis, we simulate the expected exclusion limit as follows. (i) For each disjoint SR X, we calculate the expected upper limit on the number of non-SM events N^X from the number of the background events given in Ref. [51]. (ii) At each model point, the expected number of the signal events in each SR is calculated. (iii) The model point is excluded if and only if it is excluded in at least one of the SRs. First, we calculate (i). In Ref. [51], the Monte-Carlo simulation data of the number of the SM background events for SR X, N_b^X, is given as

$$N_b^{\rm dis.A} = 163\,,\ N_b^{\rm dis.B} = 47.9\,,\ N_b^{\rm dis.C} = 17.4\,,\ N_b^{\rm dis.D} = 10.3\,, \tag{5.22}$$

for 3000 fb^{-1} and

$$N_b^{dA} = 6.51\,,\ N_b^{dB} = 3.54\,,\ N_b^{dC} = 2.35\,, \tag{5.23}$$

for 300 fb^{-1} . In addition, the error of these numbers, δ_b^X, are estimated as $\delta_b^X = N_b^X \times 0.3$. With the number of the non-SM signal events of the SR X, N^X, the significance-like variable

Z_N^X can be defined as [107]

$$
\begin{aligned}
Z_N^X &= \Phi^{-1}(1-p^X),\ \Phi(z) = \frac{1}{\sqrt{2\pi}}\int_{-\infty}^{z} e^{-t^2/2}dt\,, \\
p^X &= \int_0^\infty \frac{\Gamma(N^X+b,0,b)}{\Gamma(N^X+b)}\frac{1}{\sqrt{2\pi}\delta_b^X}e^{-\frac{(b-N_b^X)^2}{2(\delta_b^X)^2}}\,db\,,
\end{aligned}
\tag{5.24}
$$

where $\Gamma(a,b) = \int_b^\infty t^{a-1}e^{-t}dt$ is the incomplete gamma function and $\Gamma(a) = \Gamma(a,0),\ \Gamma(a,b,c) = \Gamma(a,b) - \Gamma(a,c)$. From this expression (5.24), the expected number N^X which results the given significance Z_N^X can be obtained. We denote the number as $N^X(Z_N^X = z)$ for the given significant z. The expected exclusion limit on N^X at 95% CL is derived by solving Eq. (5.24) with $Z_N^X = 1.64$ in Ref. [51]. Thus, we calculate these numbers. The results become as

$$
\begin{aligned}
N^{\rm dis.A}(Z_N^{\rm dis.A} = 1.64) &= 21.7\,, &(5.25)\\
N^{\rm dis.B}(Z_N^{\rm dis.B} = 1.64) &= 12.2\,, &(5.26)\\
N^{\rm dis.C}(Z_N^{\rm dis.C} = 1.64) &= 7.70\,, &(5.27)\\
N^{\rm dis.D}(Z_N^{\rm dis.D} = 1.64) &= 6.12\,, &(5.28)
\end{aligned}
$$

for 3000 fb^{-1} and

$$
\begin{aligned}
N^{\rm dis.A}(Z_N^{\rm dis.A} = 1.64) &= 4.92\,, &(5.29)\\
N^{\rm dis.B}(Z_N^{\rm dis.B} = 1.64) &= 3.81\,, &(5.30)\\
N^{\rm dis.C}(Z_N^{\rm dis.C} = 1.64) &= 3.23\,, &(5.31)
\end{aligned}
$$

for 300 fb^{-1}. Using these number, we set on the expected exclusion limit with the calculation (ii), (iii).

We calculate the cross sections and the acceptance for $100 \leq |\mu| \leq 1000$ GeV. We take 91 sample points for $|\mu|$ per 10 GeV, i.e. $|\mu| = 100, 110, 120, \cdots, 1000$ GeV. For each $|\mu|$, the sample points for other parameters are taken as follows. Cross sections : We take 2 sample points as $(M_1, \mathrm{sign}(\mu), \tan\beta) = (80\ \mathrm{GeV}, +, 2)$ and (30 GeV,+,50). From these sample points, in the same way written in Sec. 5.5.1, we can get the data sets $\{(m_{\chi_j^0} - m_{\chi_1^\pm}, \sigma')\}$ where $\sigma' = \sigma/(|(O_n)_{j2}|^2 + |(O_n)_{j3}|^2)$. Then, interpolating σ' as the function of $m_{\chi_j^0} - m_{\chi_1^\pm}$, the cross section σ' for the points with $M_1 = 30, 35, 40, \cdots, 80$ GeV, $\mathrm{sign}(\mu) = \pm$ and $\tan\beta = 2, 3, 4, \cdots, 50$ are calculated. Then the cross section is obtained by $\sigma = \sigma' \times (|(O_n)_{j2}|^2 + |(O_n)_{j3}|^2)$. Acceptance: we calculate the acceptances changing the masses $m_{\chi_1^0}, m_{\chi_{2,3}^0}$ while keeping the couplings as the fixed values of $M_1 = 50$ GeV, $\mu = 200$ GeV, $\tan\beta$=5. This is the same reason written in Sec. 5.5.1. We have checked that actually the differences of the couplings in our current setup does not change the acceptance.[10] The sample points are taken as $m_{\chi_j^0} - m_{\chi_1^\pm} = 0, 10, \cdots, \max(m_{\chi_j^0} - m_{\chi_1^\pm})$ GeV and

[10] We have checked in the same way written in Sec. 5.5.1 with 4×8 sample points where 4 sample points for the fixed masses and 8 sample points for changing the couplings are taken into account. As a result, the acceptances for each fixed mass point agree within the statistical uncertainties of the Monte-Carlo events.

$m_{\chi_1^0} = 30, 35, 40, \cdots, 80$ GeV for each $|\mu| \leq 300$ GeV and $m_{\chi_1^0} = 30, 40, 50, \cdots, 80$ GeV for each $|\mu| > 300$ GeV. Interpolating the acceptance as the function of $(m_{\chi_j^0} - m_{\chi_1^\pm}, m_{\chi_1^0})$, the acceptances for the points with $M_1 = 30, 35, 40, \cdots, 80$ GeV, $\mathrm{sign}(\mu) = \pm$ and $\tan\beta = 2, 3, 4, \cdots, 50$ are calculated. Finally, the number of events are calculated by Eq. (5.17). Here, we do not consider the region of $m_{\chi_j^0} - m_{\chi_1^0} < m_Z$, for simplicity. The results are shown in Sec. 6.5.2.

5.6 Mono-photon/jet Searches and Indirect Detections

We analyze the mono-photon/jet process and the indirect detections. Here, we briefly discuss the calculations.

5.6.1 Mono-photon and Mono-jet

The mono-photon search is performed by the LEP [81]. In our model, only the process $e^+e^- \to Z \to \chi_1^0\chi_1^0\gamma$ contributes to the mono-photon process. To compare the results from the LEP [81], we calculate the cross section of this process at $\sqrt{s} = 205$ GeV. In the calculation, we use the MadGraph5_aMC@NLO 2.2.3 [97]. As the constraints, we use the results for the unknown process $e^+e^- \to X\gamma$ which give $\sigma(e^+e^- \to X\gamma) \lesssim 0.05$–$0.2$ pb depending on the missing energy 60–200 GeV (see Figure 3.4). The results are shown in Sec. 6.6.

The mono-jet search is performed by the LHC [84]. The constraints from the CMS [84] are translated to the generic vector mediator model in Ref. [80]. In our model, only the process $pp \to Z \to \chi_1^0\chi_1^0 j$ contributes. In Sec. 3.4.1, we reinterpret the constraints on the Z boson mediated process. With rough estimation, $|\lambda^Z| < 0.2$–0.6 is obtained. Although this estimation is rough, our model seems not to be sensitive to this constraint (see Eq. (4.23)). We calculate λ^Z in all points and compare with the constraint. The results are shown in Sec. 6.6.

5.6.2 Cosmic Rays

As we can see in Sec. 3.5.1, the DM can annihilate in the present Universe. In our model, the annihilation occurs in only two ways: $\chi_1^0\chi_1^0 \to h \to$SMs and $\chi_1^0\chi_1^0 \to Z \to$ SMs. However, these process are mainly the p-wave process, i.e. the cross section is proportional to the velocity v (see Eq. (5.2) and (5.3)). Only the terms Eq. (D.11) which are neglected in Eq. (5.3) and proportional to the SM fermion masses m_f give the s-wave process, i.e. the cross section is not proportional to the velocity. Since the annihilation in the present Universe occurs in the limit $v \to 0$, only the process which is the Z boson exchange process and is proportional to the SM fermion masses contribute to this phenomenology. Especially, since the dominant masses of the SM fermions which the Z boson can decay to are m_b and m_τ, we consider the process

$\chi_1^0\chi_1^0 \to Z \to b\bar{b}, \tau^-\tau^+$. The annihilation cross section is calculated as

$$\begin{aligned}
\langle\sigma v\rangle^b\,|_{v\to 0} &\equiv \left\langle \sigma v(\chi_1^0\chi_1^0 \to Z \to b\bar{b})\right\rangle |_{v\to 0} \\
&= \frac{1}{8\pi}\frac{e^2}{s_{2W}^2}(\lambda^Z)^2\frac{3m_b^2}{m_Z^4} \\
&\simeq 2.5\times 10^{-26}\cdot(\lambda^Z)^2\ \mathrm{cm^3 s^{-1}}\,, \qquad (5.32)\\
\langle\sigma v\rangle^\tau\,|_{v\to 0} &\equiv \left\langle \sigma v(\chi_1^0\chi_1^0 \to Z \to \tau^+\tau^-)\right\rangle |_{v\to 0} \\
&= \frac{1}{8\pi}\frac{e^2}{s_{2W}^2}(\lambda^Z)^2\frac{m_\tau^2}{m_Z^4} \\
&\simeq 2.9\times 10^{-27}\cdot(\lambda^Z)^2\ \mathrm{cm^3 s^{-1}}\,. \qquad (5.33)
\end{aligned}$$

We use the mass of the tau lepton $m_\tau = 1.777\mathrm{GeV}$ [63] and the running mass for the bottom quark $\bar{m}_b^{\overline{\mathrm{MS}}} \simeq 3\mathrm{GeV}$ [108].[11] The constraints are given by the Fermi-LAT [85]. The constraints are set by comparing the above annihilation cross sections and the Fermi-LAT constraints Figure 3.7 for each channel $b\bar{b}$ and $\tau^+\tau^-$. The results are shown in Sec. 6.6.

5.6.3 DM Annihilation in the Sun

The DM annihilation in the Sun is also constrained now from the Super-Kamiokande [86] (see Sec. 3.5.2). It is the same as the cosmic rays that only the s-wave process $\chi_1^0\chi_1^0 \to Z \to b\bar{b}, \tau^-\tau^+$ contribute to this phenomenology. Thus, only the spin dependent process contributes and the constraints are set on $\sigma_p^{\mathrm{SD(eff)}}$ (see Eq. (3.12)). Note that since the constraints from the Super-Kamiokande are obtained by assuming 100% branching ratio, we need multiply the branching ratio. Thus we calculate the following effective cross sections $(\sigma_p^{\mathrm{SD(eff)}})^{b,\tau} = \sigma_p^{\mathrm{SD(eff)}} \times \mathrm{Br}(b,\tau)$ where $\mathrm{Br}(b,\tau) \simeq \frac{\langle\sigma v\rangle^{b,\tau}|_{v\to 0}}{\langle\sigma v\rangle^b|_{v\to 0}+\langle\sigma v\rangle^\tau|_{v\to 0}}$. Here, $\mathrm{Br}(b) \simeq 3m_b^2/(3m_b^2+m_\tau^2) \simeq 0.90$, and $\mathrm{Br}(\tau) \simeq m_\tau^2/(3m_b^2+m_\tau^2) \simeq 0.10$. The effective cross sections multiplied these branching ratios are compared to the constraints set by the Super-Kamiokande for each channel $b\bar{b}, \tau^+\tau^-$ [86] (Figure 3.8). Note that not only the above branching ratios but also the $\tanh^2$ factors in Eq. (3.12) are taken into account. The results are shown in Sec. 6.6.

[11] We have checked that the cross sections in our calculation agree with those in using micrOMEGAs [90–92] within $\mathcal{O}(1)$% for $\tau^-\tau^+$ channel and $\mathcal{O}(10)$% for $b\bar{b}$ channel.

Chapter 6

Results

Here, we show the results of our analysis. Main results are shown in Figures 6.1–6.5. Here we present the results in the $(m_{\chi_1^0}, m_{\chi_1^\pm})$-planes for $2 \leq \tan\beta \leq 50$. In the outer region of the shown region, the DM becomes overabundant. In the figures, each line corresponds to each experimental constraints/prospects as follows:

black line	:	relic abundance, $\Omega h^2 = 0.120$ (Sec. 6.1)
gray shaded region	:	excluded region by the current constraints as below
– **blue dashed line**	:	the LUX constraints on the SI scattering cross section (Sec. 6.2)
– **green dashed line**	:	the XENON100 constraints on the SD scattering cross section (Sec. 6.3)
– **magenta dashed line**	:	the global fit constraints on the Higgs invisible decay (Sec. 6.4)
light yellow region	:	region which can be probed by the future experiments as below
– **blue solid line**	:	the XENON 1T prospects on the SI scattering cross section (Sec. 6.2)
– **green solid line**	:	the XENON 1T prospects on the SD scattering cross section (Sec. 6.3)
– **magenta dot-dashed line**	:	the (HL) LHC prospects on the Higgs invisible decay (Sec. 6.4)
– **magenta solid line**	:	the ILC prospects on the Higgs invisible decay (Sec. 6.4)
– **red dotted line**	:	the 14 TeV LHC prospects with 300 fb^{-1} (Sec. 6.5.2)
– **red solid line**	:	the 14 TeV LHC prospects with 3000 fb^{-1} (Sec. 6.5.2)
– **light orange region**	:	region which can be probed by the 14 TeV LHC with 300 fb^{-1} (Sec. 6.5.2)

The blind spot, $\lambda^h = 0$, is also shown with a brown dotted line for $\mu < 0$. There are no constraints from the Z boson invisible decay (Sec. 6.4), the LHC 8TeV analysis (Sec. 6.5.1), the mono-photon/jet searches and the indirect searches (Sec. 6.6). In the following sections, we

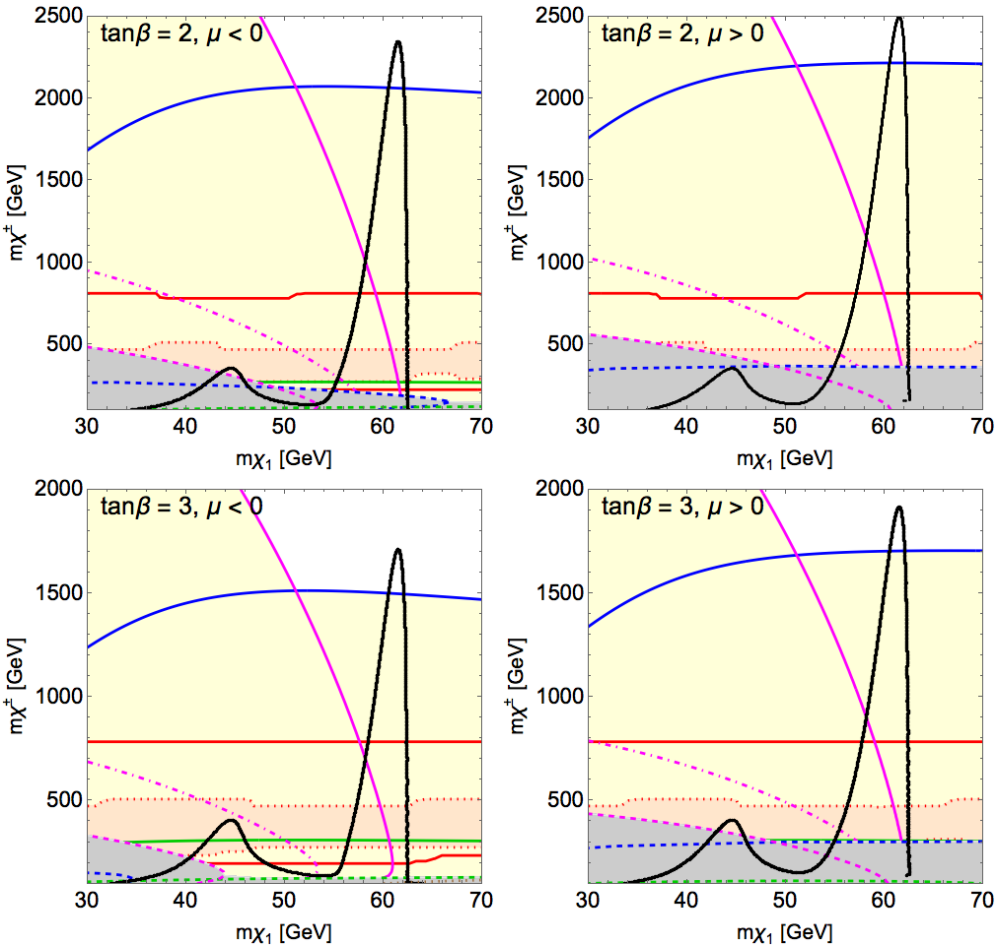

Figure 6.1: Main results of $\tan\beta = 2$ and 3, and of $\mu < 0$ (left) and $\mu > 0$ (right). The explanation of the lines are written in the text.

show the results in detail.

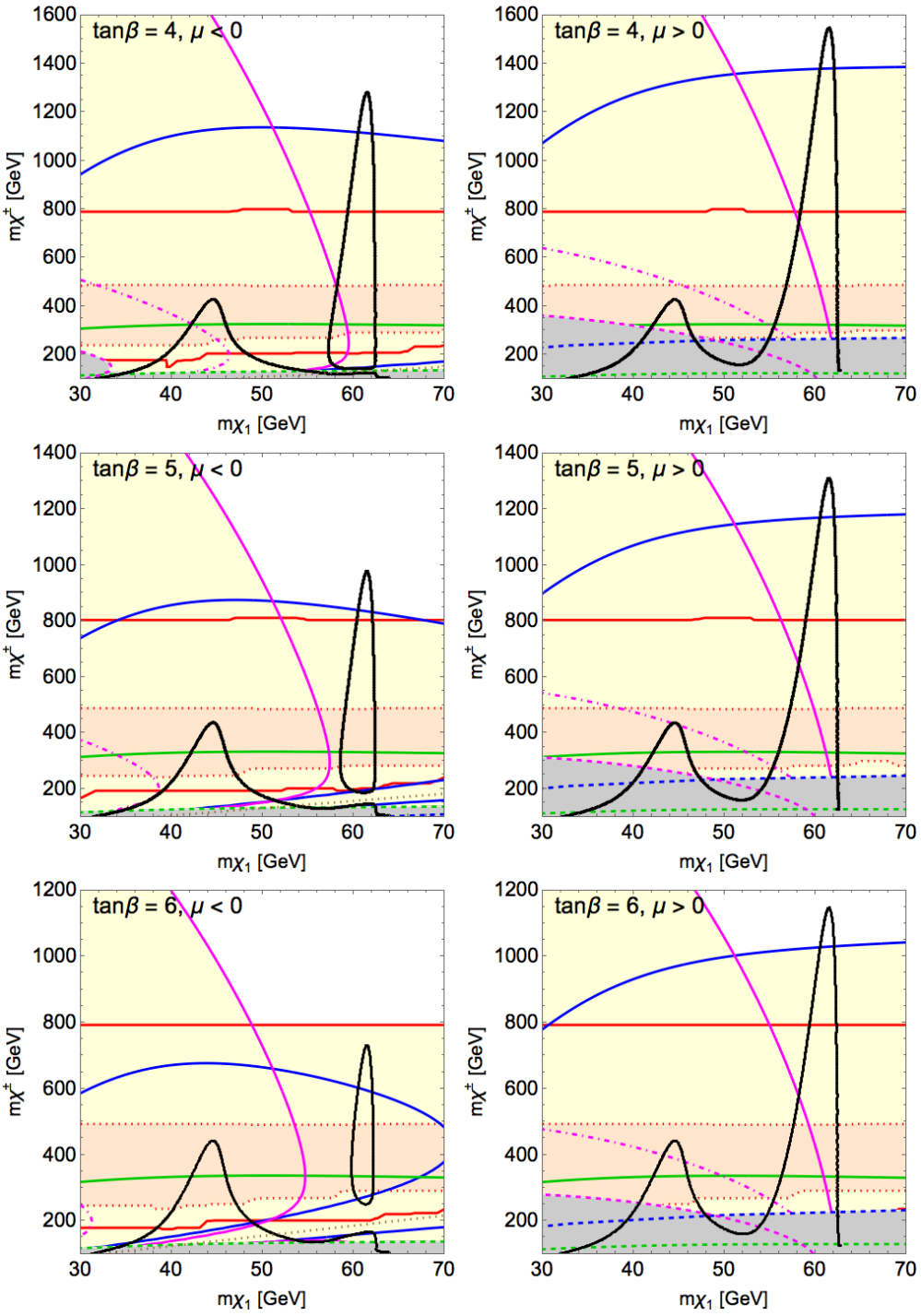

Figure 6.2: Results of $\tan\beta = 4$, 5 and 6. For $\mu < 0$, the blind spot $\lambda^h = 0$ is shown with the brown dotted line. Other lines are the same as Figure 6.1.

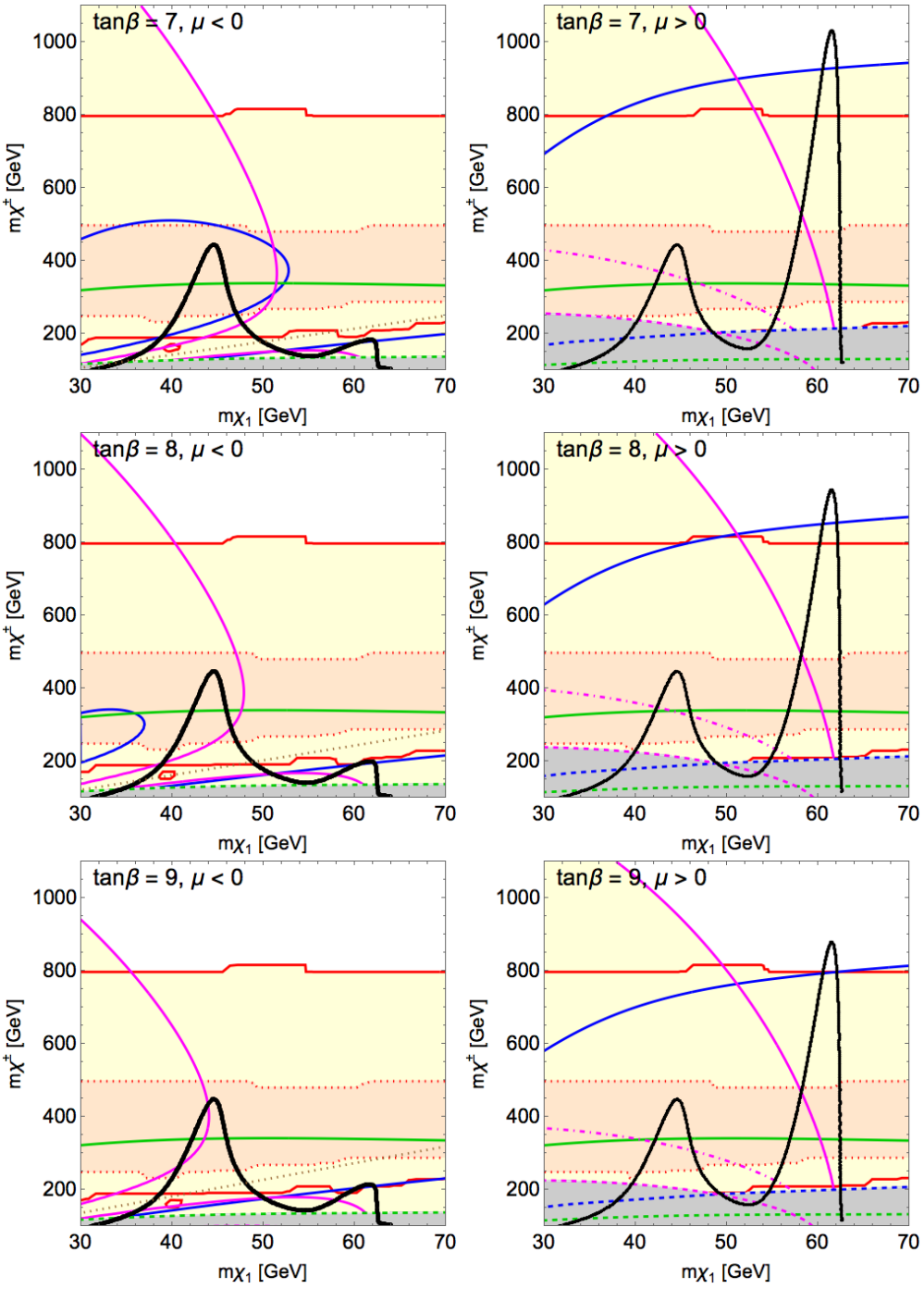

Figure 6.3: Results of $\tan\beta = 7$, 8 and 9. The same as Figure 6.1.

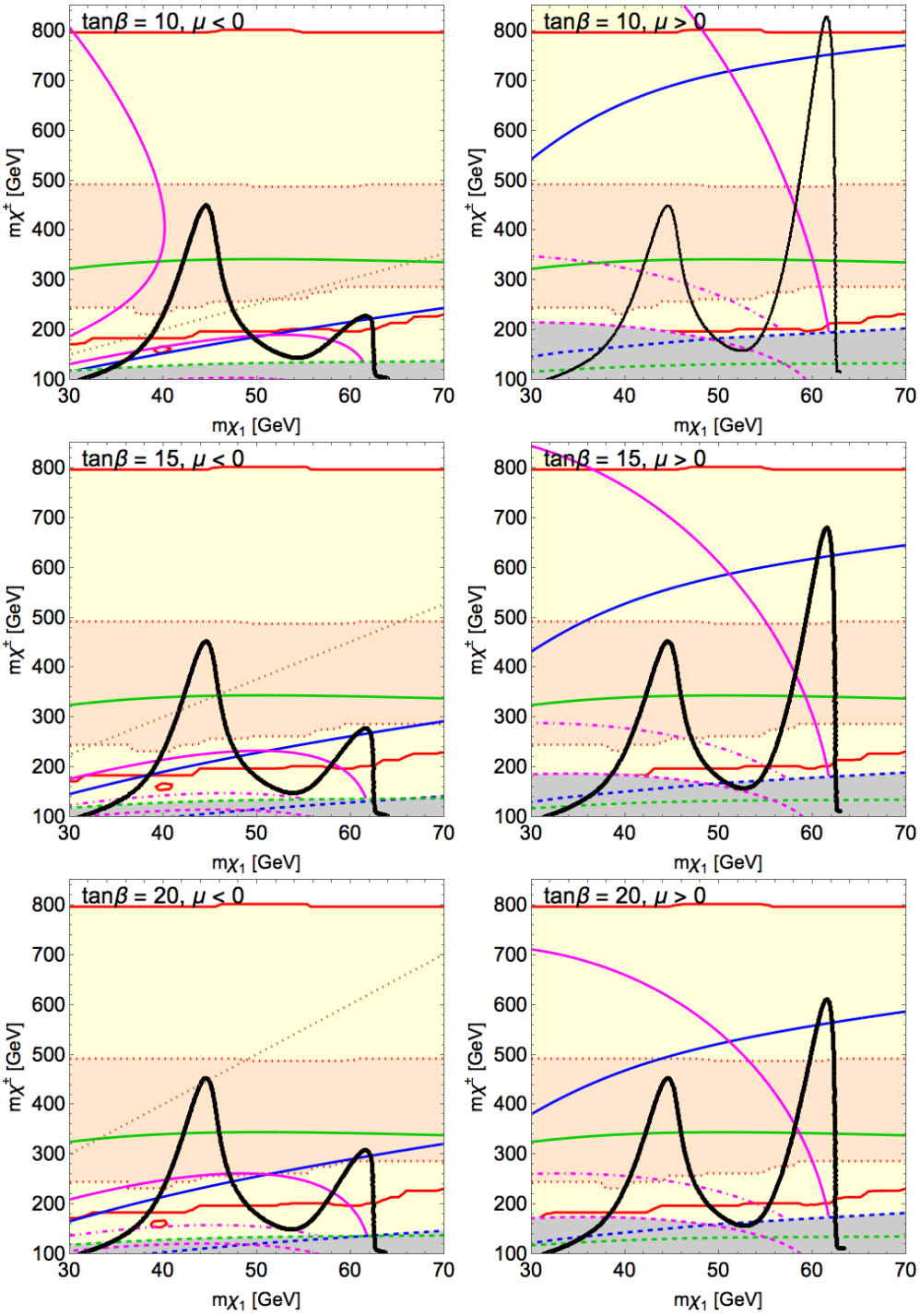

Figure 6.4: Results of $\tan\beta = 10$, 15 and 20. The same as Figure 6.1.

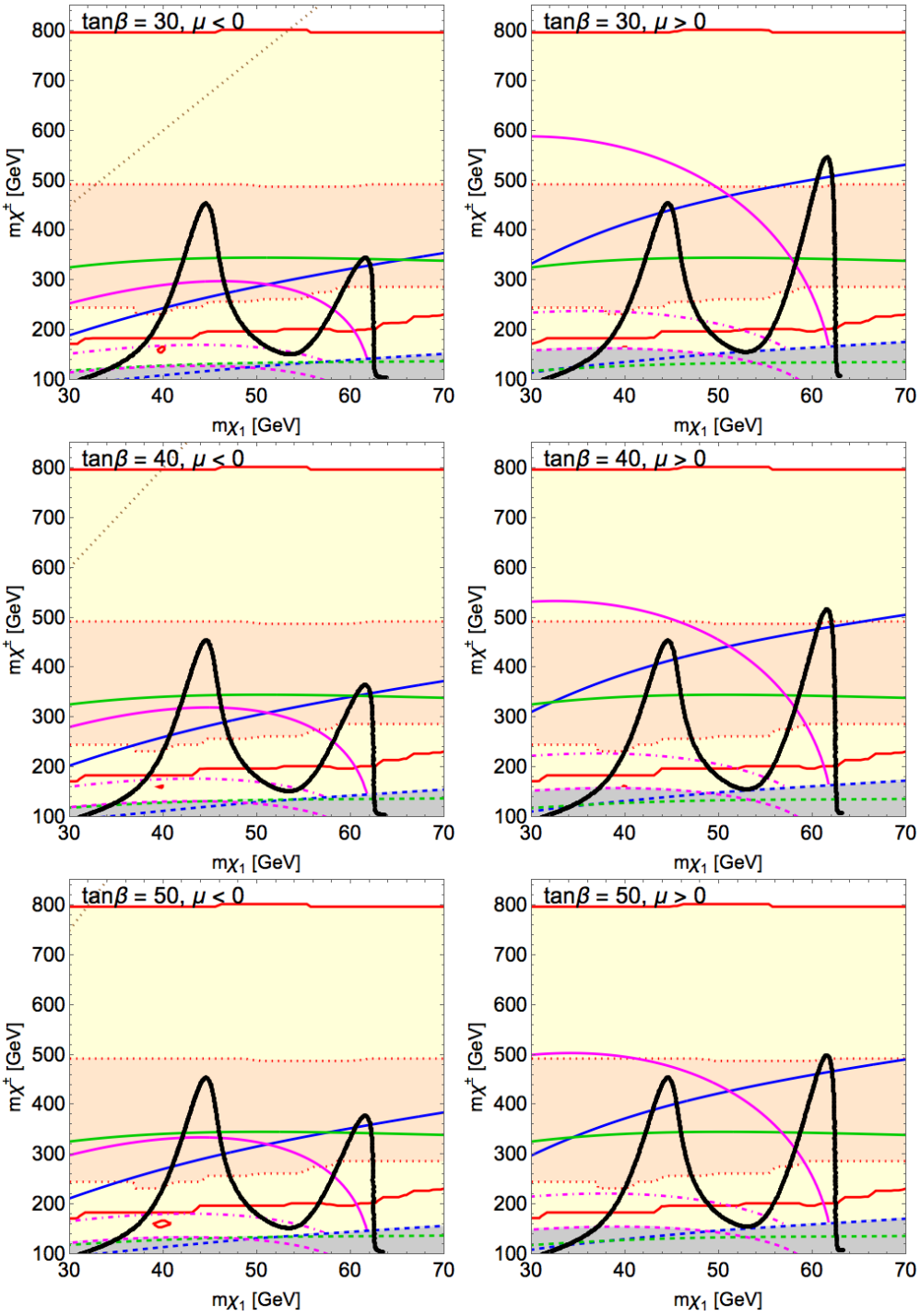

Figure 6.5: Results of $\tan\beta = 30$, 40 and 50. The same as Figure 6.1.

6.1 Relic Abundance

The contours of the relic abundance with $\Omega h^2 = 0.120$ are shown with the black lines in Figures 6.1–6.5. As we can see, clearly there are the regions where the Z boson resonance or the Higgs boson resonance occur, $m_{\chi_1^0} \sim M_Z/2 \simeq 45.6$ GeV and $m_{\chi_1^0} \sim m_h/2 \simeq 62.5$ GeV. In these regions, the annihilation cross sections become large as shown in Sec. 5.1, and the couplings λ^Z and λ^h can be small. It results that the current relic abundance can be explained with the large value of the chargino mass, $m_{\chi_1^\pm} = |\mu|$. The upper bounds of the chargino mass to explain the relic abundance are about 500 GeV for the Z resonance and 2500 GeV for the Higgs resonance. Since the chargino and the heavy neutralinos with the masses $\mathcal{O}(100)$ GeV can be produced within the LHC, the LHC searches for the heavy neutralinos/chargino become important.

In the Z resonant region, the relic abundance shows the universal behavior for all $\tan\beta \gg 1$. This is because the DM-DM-Z coupling λ^Z is almost independent of $\tan\beta$ for $\tan\beta \gg 1$, as shown in Eq. (4.21). In this region, the coupling is about $|\lambda^Z| \gtrsim 0.0034$.

In the Higgs resonant region, the behavior of the relic abundance strongly depends on $\tan\beta$ as well as sign(μ). This is also understood in terms of the DM-DM-Higgs coupling λ^h (see Eq. (4.20)). As shown in Figure 6.2, for $\mu < 0$ and $4 \leq \tan\beta \leq 6$, we can clearly see the blind spot, $\lambda^h = 0$, corresponding to Eq. (4.22) which is denoted with the brown dotted line. There are two regions corresponding to $\Omega h^2 \leq 0.120$ above and below this line. The coupling λ^h has opposite signs in the two separate regions. For $\mu < 0$ and $\tan\beta \gtrsim 7$, the region of large $m_{\chi_1^\pm}$ disappears because a sufficiently large $|\lambda^h|$ can no longer be obtained there. For both $\mu < 0$ and $\mu > 0$ and for all $\tan\beta$, the coupling is about $|\lambda^h| \simeq 0.0052$ at the tip of the Higgs resonant region. For $\tan\beta \gtrsim 10$, the upper bound on the chargino mass to explain the current relic abundance is as small as $m_{\chi_1^\pm} \lesssim 400$ GeV for $\mu < 0$ and $m_{\chi_1^\pm} \lesssim 500$–$800$ GeV for $\mu > 0$. It is the same as the Z resonance case that the LHC searches become important in these regions. For small $\tan\beta$, however, a much larger chargino mass is allowed: for example at most $m_{\chi_1^\pm} \lesssim 2500$ GeV for $\tan\beta = 2$ and $\mu > 0$. Although such a heavy chargino is out of the 14 TeV LHC reach, the direct detection can cover most of the region, as we see in Sec. 6.2.

6.2 SI Scattering

The direct detection constraints/prospects for the SI scattering cross section can cover large region. The constraints from the LUX [40] and the future prospects of XENON 1T [41] are shown in the blue dashed and solid lines respectively in Figures 6.1–6.5. Since the SI scattering cross section depends only on the mass of the DM, $m_{\chi_1^0}$, and the coupling λ^h (see also Sec. 5.2), the results are understood in terms of the coupling λ^h.

As shown in the figures, for $\mu > 0$, the region with $m_{\chi_1^\pm} \lesssim 120$–$400$ GeV (150–400 GeV) are already excluded by the LUX for the Z resonance and the Higgs resonance respectively. The XENON 1T can cover most of the viable parameter space for $\mu > 0$, except for the tip of the Higgs resonance and the tip of the Z resonance for $\tan\beta \gtrsim 30$. Here, the couplings become as

$\lambda^h \simeq 0.0052$ (see Sec. 6.1) and the cross section becomes $\sigma_N^{\rm SI} \simeq 1.4 \times 10^{-47}{\rm cm}^2$. Note that the SI scattering cross sections in these regions are just below the sensitivity shown in Ref. [41]. Therefore, it is expected that future experiments with higher sensitivity [109] can cover the whole parameter region for $\mu > 0$.

For $\mu < 0$, because of the blind spot, the constraint and the sensitivity are significantly reduced. As we can see in Figure 6.2, for $\mu < 0$ and $4 \leq \tan\beta \leq 6$, the blind spot can not be probed by the XENON 1T while the Higgs resonant region can still be mostly covered. This is because both of the relic abundance and the SI scattering cross section are determined by the same coupling λ^h. However, in the Z resonant region, the relic abundance and the SI scattering cross section are determined by the different couplings, λ^Z and λ^h, respectively. This results in a large parameter region which gives the correct relic abundance but very small SI scattering cross section, as can be seen in Figures. 6.3–6.5. Thus, the Z resonant region in the blind spot can not be probed by the SI scattering. To explore these region, we should consider the experiments which do not depend on λ^h such as the SD scattering (Sec. 6.3) and the LHC searches (Sec. 6.5).

6.3 SD scattering

Next, let us show the direct detection constraints/prospects for the SD scattering cross section. The constraints from the XENON100 [42] and the future prospects of XENON 1T [43] are shown in the green dashed and solid lines respectively in Figures 6.1–6.5.

As shown in Sec. 5.3, the SD scattering cross section depends only on the mass of the DM, $m_{\chi_1^0}$, and the coupling λ^Z. Since the coupling λ^Z is almost independent of $\tan\beta$ as shown in Eq. (4.21), the results are similar in all $\tan\beta$. The constraints and the future prospects are less sensitive than the SI scattering for $\mu > 0$. However, in the blind spot region with small $m_{\chi_1^\pm}$ for $\mu < 0$, these gives strongest constraints $m_{\chi_1^\pm} \lesssim 100$–$140$ GeV. The prospects are also more sensitive than the SI scattering and the Higgs invisible decay: $m_{\chi_1^\pm} \lesssim 280$–$350$ GeV. These are understood by the blind spot behavior as discussed in Sec. 6.2. Since there is the blind spot, these region can not be probed by the SI scattering and the Higgs invisible decay. On the other hand, since the SD scattering depends on λ^Z and not on λ^h, the constraints and prospects are not suppressed with $\lambda^h \sim 0$. Thus, although the constraints and the prospects are weak for $\mu > 0$, the searches for the SD scattering plays a complementary role to probe the blind spot for $\mu < 0$.

6.4 Invisible Decay

Here, we show the constraints and the future prospects by the searches for the Higgs boson invisible decays. The constraints from the global fit ${\rm Br}(h \to \text{invisible}) < 0.19$ [45], and the future prospects of the (HL) LHC ${\rm Br}(h \to \text{invisible}) < 0.062$ [46] and the ILC ${\rm Br}(h \to \text{invisible}) < 0.004$ [48] are shown with magenta dashed, dot-dashed and solid lines respectively in Figures 6.1–

6.5.

As we can see in the figures, a large parameter space is covered by the Higgs invisible decay search. For $\mu > 0$, in the part of the Z resonant region, the constraints from the global fits give the strongest constraints. In addition, the whole Z resonant region will be covered by the ILC even though the XENON 1T searches for the SI scattering can not probe. The tip of the Higgs resonant can not be probed since the decay width for $m_{\chi_1^0} \sim m_h/2$ is suppressed kinematically (see Eq. (5.12)).

For $\mu < 0$, the blind spots are again clearly seen. As is the same case with the SI scattering, the Higgs boson invisible decays can not probe the blind spot as clearly shown in Figure 6.2. Thus, the combination of the searches for the SD scattering and the heavy neutralinos/chargino at the LHC is necessary.

The constraints from the Z boson invisible decays result no constraints. This is because simply the constraints from the LEP [49] are weak in the present scenario. We can calculate from Eq. (5.15) that the Z boson decay width to the DMs is $\Gamma(Z \to \chi_1^0\chi_1^0) \simeq 0.43 \times (\lambda^Z/0.03)^2$ MeV for $m_{\chi_1^0} = 30$ GeV and $\Gamma(Z \to \chi_1^0\chi_1^0) \simeq 0.11 \times (\lambda^Z/0.03)^2$ MeV for $m_{\chi_1^0} = 40$ GeV. Although λ^Z can be at most $|\lambda^Z| = 0.078$ in our setup (see Eq. (4.23)), this value is obtained at $m_{\chi_1^0} \simeq 80$ GeV and it can not be satisfied in the present case $m_{\chi_1^0} < M_Z/2 = 45.6$ GeV. In the mass range where the Z boson invisible decay occurs, the maximal value of $|\lambda^Z|$ becomes smaller. For example, for $m_{\chi_1^0} \simeq 30$ GeV, $|\lambda^Z|$ can be maximum $|\lambda^Z| = 0.063$ at $M_1 = 35$ GeV, $\mu = -100$ GeV, $\tan\beta = 20$ which leads to $\Gamma(Z \to \chi_1^0\chi_1^0) = 1.9$ MeV. For $m_{\chi_1^0} \simeq 40$ GeV, $|\lambda^Z|$ can be maximum $|\lambda^Z| = 0.067$ at $M_1 = 45$ GeV, $\mu = -100$ GeV, $\tan\beta = 10$ which leads to $\Gamma(Z \to \chi_1^0\chi_1^0) = 0.53$ MeV. The larger $|\mu|$ becomes, the smaller $|\lambda^Z|$ becomes as shown in Figure 4.2. Note that for $m_{\chi_1^0} < 45.6$ GeV and $|\mu| = 110$ GeV, the maximal value of $|\lambda^Z|$ becomes $|\lambda^Z| = 0.057$ at $M_1 = 50$ GeV, $\tan\beta = 10$. Thus, $\Gamma(Z \to \chi_1^0\chi_1^0)$ in our model is always smaller than the LEP constraint $\Gamma(Z \to \chi_1^0\chi_1^0) < 2$ MeV.

6.5 Heavy Neutralinos/Chargino Searches at the LHC

Here, we show the results of the heavy neutralinos/chargino searches at the LHC. There are no constrains from the 8 TeV analysis while the future prospects of the 14 TeV analysis cover wider range. We see this in Sec. 6.5.1 and 6.5.2 respectively.

6.5.1 8TeV

The heavy neutralinos/chargino searches at the LHC 8 TeV with the ATLAS analysis give no constraints on the Bino-Higgsino resonant model. Here, we check this results in detail.

In order to investigate carefully, we show the detailed results in Table 6.1 for the following

12 model points

$$(m_{\chi_1^\pm}, m_{\chi_1}) = (200, 50), (200, 25), (150, 37.5)\ \text{GeV}\,,$$
$$\tan\beta = 5, 40\,, \qquad \text{sign}(\mu) = \pm\,. \tag{6.1}$$

In this table, the masses of heavy neutralinos $m_{\chi^0_{2,3}}$, the NLO production cross sections $\sum_{\chi_1^\pm} \sigma(pp \to \chi_1^\pm \chi_j^0)$, the branching ratio of the WZ mode $\text{Br}(WZ) = \text{Br}(\chi_j^0 \to Z\chi_1^0)$,[1] the acceptance $A_{\text{SR0}\tau\text{a16}}$ of SR0τa16 and the expected number of signal events $N_{\text{SR0}\tau\text{a16}}$ in SR0τa16 are shown. Note that SR0τa16 gives the strongest constraints in our set up. For comparison, we also show the case of pure Bino-Wino model (pBW) with $\text{Br}(\chi_2^0 \to Z\chi_1^0) = 1$. As we can see, the acceptance in the present scenario is slightly better than the pure Bino-Wino case. Note that larger $m_{\chi^0_{2,3}}$ lead to larger acceptance. On the other hand, the production cross section, $\sum_{j=2,3} \sigma(pp \to \chi_1^\pm \chi_j^0)$, is about a half of the pure Bino-Wino case as we see in Sec. 5.5. The branching fraction of the WZ mode is also smaller for $(m_{\chi_1^\pm}, m_{\chi_1^0}) = (200, 50)$ and (200,25) GeV. As a result, the expected number of events in SR0τa16, $N_{\text{SR0}\tau\text{a16}}$, becomes less than about 40% and 65% of the pure Bino-Wino case for $(m_{\chi_1^\pm}, m_{\chi_1^0}) = (200, 50/25)$ GeV and (150, 37.5) GeV, respectively.

So far, we have considered only the process (5.16). In order to check the contributions from the other channels, we have generated all the possible processes: all the possible pair production processes, $pp \to \chi_i^0\chi_j^0, \chi_i^0\chi_1^\pm, \chi_1^+\chi_1^-$, $(i, j = 1, 2, 3)$, the decay into the Higgs boson, $\chi^0_{2,3} \to h\chi_1^0$, and the hadronic decays of the W boson and the Z boson. The expected number of events in SR0τa16 including all these processes, $N^{\text{All}}_{\text{SR0}\tau\text{a16}}$, are shown in the last column of Table 6.1.[2] They are at most about 15% larger than $N_{\text{SR0}\tau\text{a16}}$. We have checked that the additional contributions mainly come from the production channel $pp \to \chi_2^0\chi_3^0$.

In Table 6.2, we show the expected number of events in SR0τa14, 15, and 16. Here, we have included all the processes discussed above. We compare them with the upper limit constraints at 95% CL on the number of non-SM events for each signal region, N^{95}_{obs} [50]. In the other signal regions, i.e. SR0τa1–13 and 17–20, the signal events are less than about 10% and 25% of the upper limits for $(m_{\chi_1^\pm}, m_{\chi_1^0}) = (200, 50/25)$ GeV and (150, 37.5) GeV, respectively. We find that none of these model points are excluded. In order to check the difference of the simulation programs, we have also simulated with Herwig++ 2.7 [110] in all the parameter points written above. The results by using Herwig++ agree with the above results by using MadGraph and PYTHIA within the statistical uncertainties of the Monte-Carlo events.

Note that as shown in Appendix E.1 our results for the pure Bino-Wino model are about 20% weaker than those of the ATLAS. It may be due to the differences of the hadronic tau identification efficiencies since it is considered difficult to simulate the identification in the fast simulations and the latest efficiency is not available in Ref. [50]. Anyway, we should consider the effects of the $\mathcal{O}(10)$% uncertainties. If we change the result with $\mathcal{O}(10)$%, the result for

[1] Note that $\text{Br}(\chi_1^\pm \to W^\pm \chi_1^0) = 1$.

[2] We have generated 3,000,000 events for each model point to calculate $N^{\text{All}}_{\text{SR0}\tau\text{a16}}$.

$m_{\chi_1^\pm}$, m_{χ_1}	t_β, ϵ_μ	χ_j^0	$m_{\chi_j^0}$	$\sigma(\chi_1^\pm \chi_j^0)$	Br(WZ)	$A_{\mathrm{SR0}\tau\mathrm{a16}} \times 10^3$	$N_{\mathrm{SR0}\tau\mathrm{a16}}$	$N^{\mathrm{All}}_{\mathrm{SR0}\tau\mathrm{a16}}$
200, 50	5, +	χ_2^0	202.3	192	0.958	16.9 ± 0.2	2.08 ± 0.02	
		χ_3^0	208.8	171	0.328	18.7 ± 0.2	0.70 ± 0.01	2.91 ± 0.10
	5, −	χ_2^0	203.9	185	0.697	18.0 ± 0.2	1.55 ± 0.02	
		χ_3^0	205.3	183	0.819	18.2 ± 0.2	1.82 ± 0.02	3.75 ± 0.12
	40, +	χ_2^0	203.6	188	0.919	17.7 ± 0.2	2.05 ± 0.02	
		χ_3^0	206.7	177	0.490	18.1 ± 0.2	1.05 ± 0.01	3.25 ± 0.11
	40, −	χ_2^0	204.0	186	0.902	18.0 ± 0.2	2.01 ± 0.02	
		χ_3^0	206.0	179	0.538	18.5 ± 0.2	1.19 ± 0.01	3.53 ± 0.12
	pBW	χ_2^0	200	788	1.0	15.5 ± 0.2	8.15 ± 0.09	
200, 25	5, +	χ_2^0	202.6	191	0.902	22.4± 0.2	2.58 ± 0.02	
		χ_3^0	207.6	176	0.405	24.1± 0.2	1.14 ± 0.01	3.84 ± 0.12
	5, −	χ_2^0	203.3	188	0.761	23.3 ± 0.2	2.23 ± 0.02	
		χ_3^0	205.9	182	0.657	23.7 ± 0.2	1.89 ± 0.02	4.49 ± 0.13
	40, +	χ_2^0	204.0	186	0.822	23.1 ± 0.2	2.35 ± 0.02	
		χ_3^0	205.7	180	0.572	23.4 ± 0.2	1.61 ± 0.01	4.18 ± 0.13
	40, −	χ_2^0	204.4	186	0.792	22.8 ± 0.2	2.24 ± 0.02	
		χ_3^0	205.2	182	0.618	23.1 ± 0.2	1.74 ± 0.02	4.47 ± 0.13
	pBW	χ_2^0	200	788	1.0	20.3 ± 0.1	10.7 ± 0.1	
150, 37.5	5, +	χ_2^0	153.0	575	1.0	2.76 ± 0.07	1.06 ± 0.03	
		χ_3^0	161.7	474	1.0	3.67 ± 0.09	1.16 ± 0.03	2.41 ± 0.16
	5, −	χ_2^0	155.1	545	1.0	3.06 ± 0.08	1.11 ± 0.03	
		χ_3^0	157.0	536	1.0	3.15 ± 0.08	1.13 ± 0.03	2.46 ± 0.17
	40, +	χ_2^0	154.7	558	1.0	3.08 ± 0.08	1.15 ± 0.03	
		χ_3^0	158.8	503	1.0	3.42 ± 0.08	1.15 ± 0.03	2.68 ± 0.17
	40, −	χ_2^0	155.2	553	1.0	3.23 ± 0.08	1.19 ± 0.03	
		χ_3^0	158.0	513	1.0	3.49 ± 0.08	1.19 ± 0.03	2.43 ± 0.16
	pBW	χ_2^0	150	2427	1.0	2.26 ± 0.07	3.66 ± 0.11	

Table 6.1: The detailed results of the 8 TeV analysis are shown. The masses of heavy neutralinos $m_{\chi^0_{2,3}}$, the NLO production cross sections $\sigma(\chi_1^\pm \chi_j^0) = \sum_{\chi_1^\pm} \sigma^{\mathrm{NLO}}(pp \to \chi_1^\pm \chi_j^0)$, the branching ratio of the WZ mode $\mathrm{Br}(WZ) = \mathrm{Br}(\chi_j^0 \to Z\chi_1^0)$, the acceptance $A_{\mathrm{SR0}\tau\mathrm{a16}}$ of SR0τa16, and the expected number of signal events $N_{\mathrm{SR0}\tau\mathrm{a16}}$ in SR0τa16 are shown. For comparison, we also show the results for the pure Bino-Wino model (pBW). The errors of $A_{\mathrm{SR0}\tau\mathrm{a16}}$ are the statistical errors of Monte-Carlo events only. $N_{\mathrm{SR0}\tau\mathrm{a16}}$ is calculated by using Eq. (5.17). $N^{\mathrm{All}}_{\mathrm{SR0}\tau\mathrm{a16}}$ is the expected number including all the production and decay channels. The masses and the cross sections are in units of [GeV] and [fb], respectively.

$(m_{\chi_1^\pm}, m_{\chi_1^0})$	(200, 50) [GeV]				(200, 25) [GeV]				(150, 37.5) [GeV]				
$\tan\beta$	5	5	40	40	5	5	40	40	5	5	40	40	
$\mathrm{sign}(\mu)$	+	−	+	−	+	−	+	−	+	−	+	−	$N_{\rm obs}^{95}$ [50]
$N_{\rm SR0\tau a14}^{\rm All}$	7.2	7.7	7.9	8.1	7.7	8.2	8.2	8.1	21.9	22.9	22.2	22.4	65
$N_{\rm SR0\tau a15}^{\rm All}$	6.9	8.2	7.5	7.9	7.2	7.8	7.4	8.0	19.2	21.0	21.2	21.0	27.6
$N_{\rm SR0\tau a16}^{\rm All}$	2.9	3.8	3.3	3.5	3.8	4.5	4.2	4.5	2.4	2.5	2.7	2.4	5.2

Table 6.2: The expected numbers of events including all processes for the 8 TeV analysis are shown. $N_{\rm obs}^{95}$ is the upper limit constraints at 95% CL on the number of non-SM events for each signal region given in Ref. [50].

$\tan\beta = 5$ becomes as Figure 6.6. Here, we include all the possible processes and the numbers of signal events are multiplied by 1.3 (blue line), 1.5 (red line) and 1.7 (green line). As we can see, in this mass range, the expected number of signal events are same order for all parameter points and the difference of $\mathcal{O}(10)$% changes the results drastically. Thus, when we set the limit, we should deal with $\mathcal{O}(10)$% differences carefully. However, even including these uncertainties, our results do not change since our results are already conservative which do not set the exclusion limits.

This result does not agree with the previous work [35] where $m_{\chi_1^\pm} \lesssim 250$ GeV is excluded depending on $\tan\beta$ and $m_{\chi_1^0}$. Our analysis would lead to the similar bounds in Ref. [35] if the event numbers are increased by about 50%. As shown above, we simulate including all possible processes $pp \to \chi\chi$, the hadronic decay of gauge bosons and the decay $\chi_{2,3}^0 \to h\chi_1^0$. In addition, we also simulate with Herwig++. Although this setup is same [111] for our analysis and Ref. [35], our analysis results no exclusion. The detailed date like the cross sections, the branching ratios, the acceptances and so on is not available [111] and we can not compare with them. Thus, we can not identify the origin of the difference. However, as noted above, since $\mathcal{O}(10)$% uncertainties change the results drastically, we should be careful to give the constraints.

6.5.2 14TeV

The future prospects of the 14 TeV LHC analysis at 3000 fb^{-1} are shown with the red lines in Figure 6.1–6.5. The expected exclusion region at 300 fb^{-1} is also shown in the light orange region with the red dotted lines. We can see that the tip of the Z resonance in the whole parameter space can be probed at 300 fb^{-1} even in the blind spot. For $\tan\beta \geq 30$, the Higgs tip can also be covered. The small $m_{\chi_1^\pm}$ region is not covered because of the small mass differences between $\chi_{2,3}^0, \chi_1^\pm$ and χ_1^0.

At 3000 fb^{-1}, much larger parameter space will be probed, up to $m_{\chi_1^\pm} \sim 800$ GeV. The Higgs resonant regions are covered for $\tan\beta \gtrsim 15$ ($\tan\beta \geq 6$) for $\mu > 0$ ($\mu < 0$). Although the small $m_{\chi_1^\pm}$ region can not be covered even at 3000 fb^{-1}, combination with other experiments

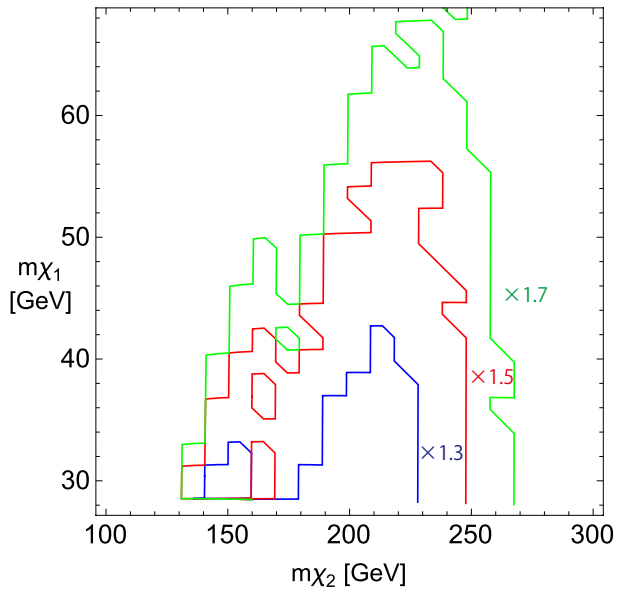

Figure 6.6: The exclusion limits with the number of signal events multiplied by a factor 1.3 (blue line), 1.5 (red line) and 1.7 (green line) for $\tan\beta = 5$ are shown. See text for details.

such as the direct detections can probe almost all the parameter region of the present scenario.

As can be seen in the figures, the expected reach at 3000 fb^{-1} for the chargino mass, $m_{\chi_1^\pm} \sim$ 800 GeV, is almost independent of $\tan\beta$ and $m_{\chi_1^0}$. This can be understood as follows. In the large $m_{\chi_1^\pm}$ region, the cross section is mainly determined by $|\mu|$ because the mass difference among $\chi_{2,3}^0, \chi_1^\pm$ are small $m_{\chi_2^0} \simeq m_{\chi_3^0} \simeq m_{\chi_1^\pm} = |\mu|$. The coupling which corresponds to the production of $\chi_{2,3}^0 \chi_1^\pm$ is also almost constant as shown in Sec. 4.5. In addition, because of the large mass hierarchy $m_{\chi_{2,3}^0} \simeq m_{\chi_1^\pm} \gg m_{\chi_1^0}, M_Z, M_W$, the acceptance is determined almost only by $|\mu|$. Thus, from Eq. (5.17), the number of events for the SR X, $N_{\rm SRX}$, can be written as

$$\begin{aligned} N_{\rm SRX} \simeq & \sum_{\chi_1^\pm} \sigma(pp \to \chi_1^\pm \chi_2) \times {\rm Br}(\chi_1^\pm \to W^\pm \chi_1^0) \times {\rm Br}(W^\pm \to l\nu) \times A_{\rm SRX} \times \int \mathcal{L} dt \\ & \times \left(\sum_{j=2,3} {\rm Br}(\chi_j^0 \to Z \chi_1^0) \right) \times {\rm Br}(Z \to ll) \,. \end{aligned} \tag{6.2}$$

The first line of this equation is determined almost only by $|\mu|$. The first term of the second line can be expanded in terms of $\mathcal{O}(M_Z s_W/\mu)$ as ${\rm Br}(\chi_2^0 \to Z\chi_1^0) + {\rm Br}(\chi_3^0 \to Z\chi_1^0) = 1 + \mathcal{O}((M_Z s_W/\mu)^2)$ (see Eq. 4.28). Thus $N_{\rm SRX}$ is almost independent of $\tan\beta$ and $m_{\chi_1^0}$, and the results become similar for all $\tan\beta$ and $m_{\chi_1^0}$.

As shown in Appendix E.2, it is different from the 8 TeV analysis that our results for the pure Bino-Wino model agree well with those of the ATLAS. This may be due to that the tau identification is not used in 14 TeV analysis. In addition, even if we include $\mathcal{O}(10)\%$ uncertainties, the results for the Bino-Higgsino resonant model do not change much since the numbers of the

signal events are much different for different mass points.

Finally, we comment on the importance of the simulation to reinterpret the ATLAS analysis. If we simply set the future prospects by rescaling the ATLAS results with the cross sections, the expected exclusion limit becomes $m_{\chi_1^\pm} \lesssim 900$ GeV for 3000 fb^{-1} and $m_{\chi_1^\pm} \lesssim 650$ GeV for 300 fb^{-1}. These results are much different from our results $m_{\chi_1^\pm} \lesssim 800$ GeV for 3000 fb^{-1} and $m_{\chi_1^\pm} \lesssim 500$ GeV for 300 fb^{-1}. Thus, taking account of the differences between our model and the pure Bino-Wino model written in Sec. 5.5 is very important and the detailed simulations are necessary.

6.6 Mono-photon/jet Searches and Indirect Detections

There are no constraints from the mono-photon/jet searches and the indirect detections. For the mono-photon process, we calculate the cross section $e^+e^- \to Z \to \chi_1^0\chi_1^0\gamma$ at $\sqrt{s} = 205$ GeV as shown in Sec. 5.6.1. The cross section decreases as $|\mu|$ increases since the mass $m_{\chi_1^0}$ increases and the coupling λ^Z decrease as $|\mu|$ increases. Thus, the cross section becomes maximum at $|\mu| = 100$ GeV in our setup. We show the cross sections for $|\mu| = 100$ GeV in Figure 6.7. Here, we take the $7 \times 2 \times 2 = 28$ sample points with the combination of $M_1 = 20, 30, \cdots, 80$ GeV, $\mathrm{sign}(\mu) = \pm$ and $\tan\beta = 2, 50$. Since these sample points are at the edge of our parameter region, the cross sections for other parameters with $|\mu| = 100$ GeV result within the range between the smallest value 0.03 fb and the largest value 21 fb in Figure 6.7. Note that for $m_{\chi_1^0} < 30$ GeV, the DM become overabundant. As a result, the cross section is at most 15 fb for $m_{\chi_1^0} > 30$ GeV. Thus, the upper bound 0.05–0.2 pb (Figure 3.4) is too weak and there is no constraints.

The mono-jet process also gives no constraints. As estimated in Sec. 5.6.1, the constraints $|\lambda^Z| <$0.2–0.6 are much weak in our setup where $|\lambda^Z| < 0.078$ is satisfied (see Eq. (4.23)).

The cosmic rays from the DM annihilation in the present Universe is constrained from the Fermi-LAT [85] as shown in Sec. 5.6.2. Since $|\lambda^Z|$ is at most 0.078 in our setup (see Eq. (4.23)), the annihilation cross sections become at most $\langle\sigma v\rangle^b|_{v\to 0} \sim \mathcal{O}(10^{-29})$ cm^{3}s^{-1} and $\langle\sigma v\rangle^\tau|_{v\to 0} \sim \mathcal{O}(10^{-30})$ cm^{3}s^{-1} (see Eq. (5.32) and (5.33)). The constraints are $\mathcal{O}(10^{-27}$–$10^{-26})$ cm^{3}s^{-1} (Figure 3.7) and very weak compared to the annihilation cross section in our parameter space.

Finally, we see the constraint come from the DM annihilation in the Sun. As we can calculate from Eq. (3.13), in the present case, the annihilation rate is not saturated by the scattering rate, $\sqrt{\Gamma_{\mathrm{cap.}}\Gamma_{\mathrm{ann.}}}t_\odot \lesssim 1$. Note that σ_p^{SD} is at most 10^{-40} cm^2 in our model. Thus the effective cross sections become at most $(\sigma_p^{\mathrm{SD(eff)}})^b \sim 10^{-40}$cm^2 and $(\sigma_p^{\mathrm{SD(eff)}})^\tau \sim 10^{-41}$cm^2 which are smaller than the constraints $(\sigma_p^{\mathrm{SD(eff)}})^b \leq$2–3$\times 10^{-39}$cm^2 and $(\sigma_p^{\mathrm{SD(eff)}})^\tau \leq$1–2$\times 10^{-40}$cm^2 (Figure 3.8).

These results are understood as follows. The mono-photon/jet constraints are simply weak due to the difficulties of the experiments. In the indirect detections, cosmic rays and the DM annihilation in the Sun, the point is that the annihilation cross section is mainly p-wave suppressed. The only contributions from the s-wave processes are proportional to the SM fermion masses and tend to be small. Thus, these constraints become weak.

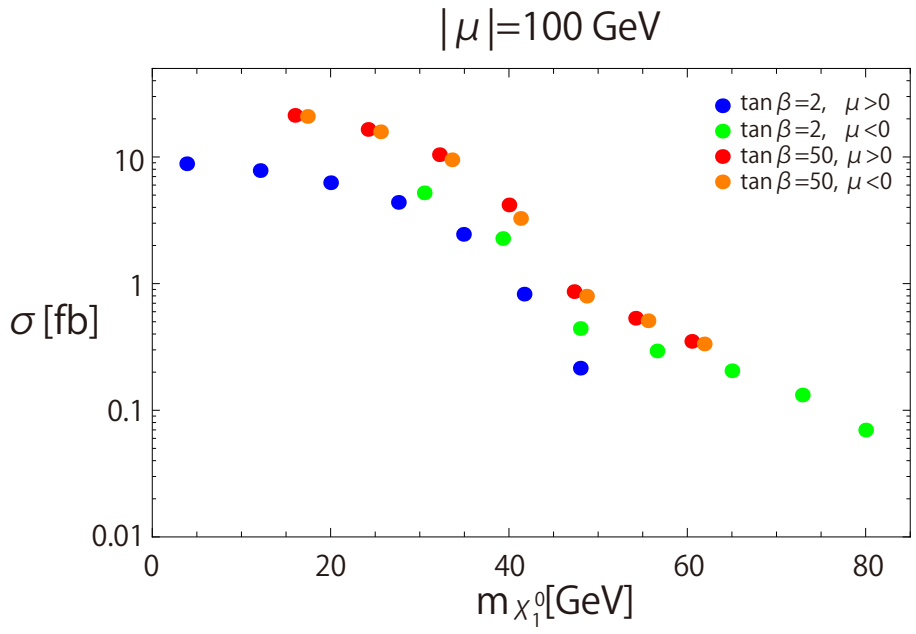

Figure 6.7: The cross sections of the mono-photon process $e^+e^- \to Z \to \chi_1^0\chi_1^0\gamma$ for $|\mu| = 100$ GeV are shown. Sample points are taken as the combination of $M_1 = 20, 30, \cdots, 80$ GeV, $\mathrm{sign}(\mu) = \pm$ and $\tan\beta = 2, 50$. The blue (green) points denote the cross sections for $\tan\beta = 2$ and $\mathrm{sign}(\mu) = +\ (-)$ while the red (orange) points denote the cross sections for $\tan\beta = 50$ and $\mathrm{sign}(\mu) = +\ (-)$.

Chapter 7

Conclusion

In this thesis, we have investigated the Bino-Higgsino resonant DM model. The Bino-Higgsino resonant DM model is one of the attractive DM models when all the sfermions are heavy $> \mathcal{O}(1$–$10)$ TeV. In this model, the Bino LSP mixes with the Higgsino slightly and can be the candidate for the DM. When the mass of the DM is half of the Higgs boson mass or the Z boson mass, $m_{\chi_1^0} \sim m_h/2, M_Z/2$, the current relic abundance can be explained with the resonant annihilation. Since the annihilation cross section is enhanced resonantly, the mixing between the Bino and the Higgsino can be small, i.e. Higgsino can be heavy as $\mathcal{O}(100$–$1000)$ GeV. Thus, this model contains $\mathcal{O}(10)$ GeV light Bino DM, two heavy neutralinos and the chargino with the masses $\mathcal{O}(100$–$1000)$ GeV. This mass spectrum gives rich phenomena in many experiments. We have investigated all the possible phenomenology and the experiments comprehensively.

We assumed that all the sfermions are heavy enough $> \mathcal{O}(1$–$10)$ TeV. The masses of the gluino and winos are assumed to be heavier than a few TeV which do not affect the phenomenology of the Bino/Higgsino system and we do not consider their effects. Then, the phenomenology of this model is determined only by three parameters, the Bino mass M_1, the Higgsino mass μ and $\tan\beta$. We have investigated the current constraints and the future prospects comprehensively for essentially all the parameter space. We have included the following phenomena: the relic abundance, the direct detection for the SI scattering, the direct detection for the SD scattering, the Higgs boson invisible decay and the heavy neutralinos/charginos productions at the 14 TeV LHC. We have also considered the Z boson invisible decay, the mono-photon/jet searches, the 8 TeV LHC searches and the indirect detections. However, these results no constraints in our parameter space.

It was shown that there is still a large viable parameter space, and almost all the parameter space of the scenario will be covered complementarily by the direct detection experiments, the Higgs invisible decay searches and the LHC searches. It is interesting that, depending on the parameters, M_1, μ and $\tan\beta$, different combinations of positive and negative signals from different experiments may appear. Especially, the blind spot is rich in the phenomenology. In this thesis, it was shown that the current constraints come from all of the SI scattering, the SD

scattering and the invisible decay. The combination of these experiments is important not only for the current constraints but also for the future prospects. The experiment which can probe the given parameter point depends on its parameter. The direct detection for the SI scattering can probe the large region except the tip of the Higgs resonant region and the blind spot. The direct detection for the SD scattering is sensitive in the lighter Higgsino region $|\mu| < 300$ GeV even in the blind spot. The Higgs invisible decay can cover the Z resonant region except the blind spot. The 14 TeV LHC searches can reveal almost all region for $200 < |\mu| < 800$ GeV. Thus, exploring these experiments is important to investigate this model.

In this thesis, we have investigated the phenomenology of the Bino-Higgsino resonant DM model and found that the comprehensive analyses is necessary. The combination of the future experiments can reveal the Bino-Higgsino resonant DM model.

Acknowledgments

The author would like to thank his supervisor Koichi Hamaguchi for the collaborations, the advices and the supports on his PhD student research life. Especially, in the collaboration on the paper on which this thesis is based, the author appreciates the longtime discussions and suggestions. The author shows his appreciations to Motoi Endo for the discussions and suggestions during all the time of his PhD course. He also thanks to Takeo Moroi, Mihoko M. Nojiri and Yoshitaro Takaesu for the useful discussions and comments. The author is grateful to Takeo Moroi, Yasuhiro Kishimoto, Masahiro Ibe, Taizan Watari and Kentaro Hori for reading and commenting this thesis. He also thanks all the member of the High Energy Physics Theory Group at University of Tokyo. Finally, the author would like to thank his family and friends for the supports.

Appendix A

Physical Values

Here, we show the physical values which we use in this thesis. We use the values in Ref. [63] if it is not mentioned with other references. The parentheses denote the error of the value.

Gauge Couplings

$$\alpha^{-1}(M_Z) = 127.944(14)\,, \quad s^2_W(M_Z) = 0.23126(5)\,, \tag{A.1}$$

where $\alpha = e^2/4\pi$. From these values, we can calculate as

$$g'(M_Z) = 0.35744(2)\,, \quad g(M_Z) = 0.65169(7)\,, \quad \frac{e}{s_{2W}}(M_Z) = 0.37164(3)\,. \tag{A.2}$$

Masses and Widths

$$M_W = 80.385(15)\ \text{GeV}\,, \quad M_Z = 91.1876(21)\ \text{GeV}\,, \tag{A.3}$$

$$\Gamma_W = 2.085(42)\ \text{GeV}\,, \quad \Gamma_Z = 2.4952(23)\ \text{GeV}\,. \tag{A.4}$$

The Higgs boson mass has been determined by the ATLAS and the CMS [58]

$$m_h = 125.09 \pm 0.21(\text{stat.}) \pm 0.11(\text{syst.})\text{GeV}\,. \tag{A.5}$$

As the width of the Higgs boson, we use $\Gamma_h = 4.07 \times 10^{-3}$ GeV which is the theoretical SM value for $m_h = 125$ GeV in this thesis.

The Branching ratio is also important in the LHC analyses. We use the following values where l denotes e, μ, τ,

$$\text{Br}(W \to l\nu) = 0.3258(27)\,, \quad \text{Br}(Z \to ll) = 0.100974(69)\,. \tag{A.6}$$

Astrophysical Constants The DM abundance of the Universe is given by Ref. [19]

$$\Omega_{\text{DM}}h^2 = 0.1199(27)\,, \quad h = 0.673(12)\,. \tag{A.7}$$

We use the following critical density of the Universe

$$\rho_{\rm crit} = 1.05375(13) \times 10^{-5} h^2 \text{ GeV cm}^{-3} \,. \tag{A.8}$$

The present temperature of the Universe T_0 is

$$T_0 = 2.755(6) \text{ K} \,. \tag{A.9}$$

These values are written in GeV units as $\rho_{\rm crit} = 8.06 \times 10^{-47} h^2 \text{ GeV}^4$, $T_0 = 2.35 \times 10^{-13}$ GeV. The gravitational constants G is given as

$$G = 6.70837(80) \times 10^{-39} \text{GeV}^{-2} \,. \tag{A.10}$$

SI/SD Scattering The masses of the proton and the neutron are

$$m_p = 0.938272046(21) \text{ GeV} \,, \quad m_n = 0.939565379(21) \text{ GeV} \,. \tag{A.11}$$

As the nucleon quark form factors, the following values which are the default values in micrOMEGAs [91] are used

$$f_u^p = 0.0153 \,, \quad f_d^p = 0.0191 \,, \quad f_s^p = 0.0447 \,, \tag{A.12}$$

$$\Delta_u^p = \Delta_d^n = 0.842 \,, \quad \Delta_d^p = \Delta_u^n = -0.427 \,, \quad \Delta_s^p = \Delta_s^n = -0.085 \,. \tag{A.13}$$

Appendix B

Wino Contribution to the DM Phenomenology

Here, we consider the contributions from the Wino to the DM phenomenology in the Bino-Higgsino resonant DM model introduced in Sec. 4. The DM phenomenology is determined by the mass of the DM $m_{\chi_1^0}$ and the DM couplings to the Higgs boson and the Z boson λ^h, λ^Z as shown in Sec. 4.4. We show the Wino dependence for these parameters.

If we take the Wino into account, the mass matrix for the neutralinos in the Bino-Higgsino system Eq. (4.6) becomes as Eq. (2.30). Thus, first, the mass of the DM χ_1^0 which is the lightest eigenvalue of the mass matrix changes. In addition, the diagonalization matrix changes. We denote the 4×4 diagonalization matrix in this case O'_n. Then, the DM couplings in the Lagrangian (4.17) becomes as

$$\lambda^h = -\left(g' \left(O'_n\right)_{11} - g \left(O'_n\right)_{12}\right)\left(c_\alpha \left(O'_n\right)_{14} + s_\alpha \left(O'_n\right)_{13}\right) , \tag{B.1}$$

$$\lambda^Z = \frac{e}{s_{2W}}\left(\left(\left(O'_n\right)_{14}\right)^2 - \left(\left(O'_n\right)_{13}\right)^2\right) . \tag{B.2}$$

Note that the subscripts of the diagonalization matrix change from Eq. (4.18) and (4.19) since the basis of the mass matrix changes as $(\chi_B\ \chi_{H_d^0}\ \chi_{H_u^0}) \to (\chi_B\ \chi_W^3\ \chi_{H_d^0}\ \chi_{H_u^0})$.

Here, we show the dependence of M_2 to $m_{\chi_1^0}, \lambda^h, \lambda^Z$. Note that for $\tan\beta \geq 2$, c_β becomes maximum $c_\beta = 0.45$ at $\tan\beta = 2$ and c_β decreases as $\tan\beta$ increases while $s_\beta \simeq 1$. Thus, in the case of $\tan\beta = 2$, the Wino contributions become maximum since the Wino and the Bino mixes with not only $\chi_{H_u^0}$ but also $\chi_{H_d^0}$ with sizable c_β. For M_1, in the case of $M_1 = 80$ GeV, the Wino contributions become maximum since the mass differences between the Bino and the Wino becomes the smallest and the mixing become the largest. Although $M_1 = 80$ GeV results $m_{\chi_1^0} \sim 80$ GeV and it results overabundant DM, we show the results with $M_1 = 80$ GeV, $\tan\beta = 2$ since for other cases the M_2 dependences become weaker.

The M_2 dependences on $m_{\chi_1^0}, \lambda^h, \lambda^Z$ are shown in Figure B.1, B.2, B.3 respectively. In all cases, if $M_2 > 500$–700 GeV, the dependences of the Wino become negligible. From these results, it is shown that the phenomenology of the DM is not affected by the Winos for $M_2 > 500$–700

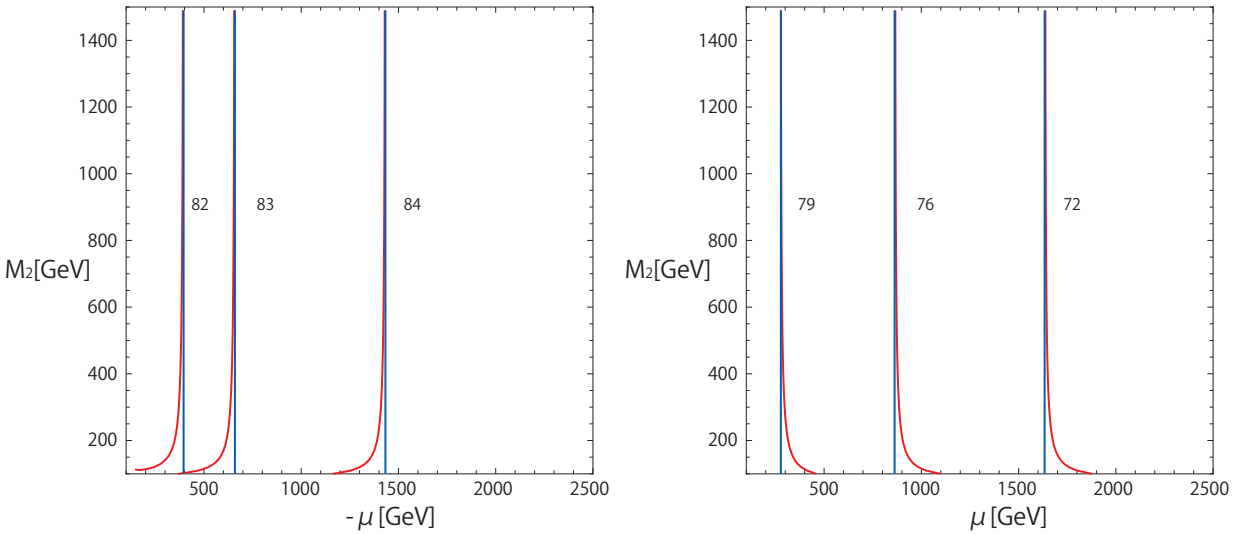

Figure B.1: The contributions from the Wino to the DM mass are shown. The lines denote the contour of the DM mass $m_{\chi_1^0}$ in the units of GeV. The red (blue) lines are the results (not) including the Wino contributions. The left (right) figure is the case of $\mu < 0$ ($\mu > 0$).

GeV.

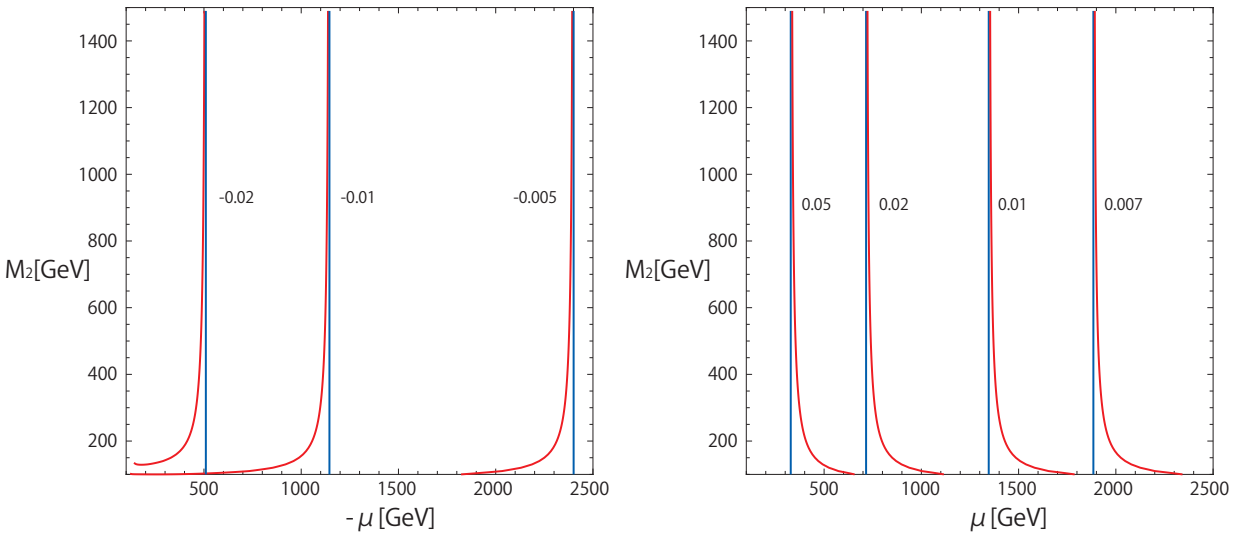

Figure B.2: The contributions from the Wino to the DM-DM-Higgs coupling are shown. The lines denote the contour of the coupling λ^h. The red (blue) lines are the results (not) including the Wino contributions. The left (right) figure is the case of $\mu < 0$ ($\mu > 0$).

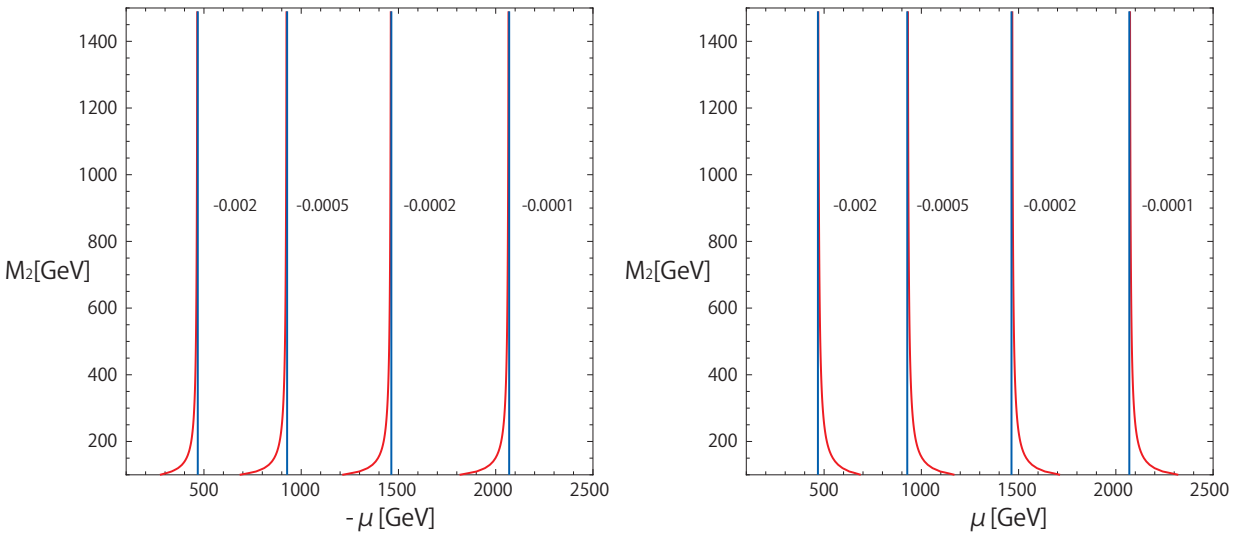

Figure B.3: The contributions from the Wino to the DM-DM-Z coupling are shown. The lines denote the contour of the coupling λ^Z. The red (blue) lines are the results (not) including the Wino contributions. The left (right) figure is the case of $\mu < 0$ ($\mu > 0$).

Appendix C

Analytical Calculations in the Bino-Higgsino Resonant model

The analytical calculations of the masses and the couplings in the Bino-Higgsino resonant model are written here. See also Sec. 4.

First, we see the mass eigenvalues of Eq. (4.6) in Appendix C.1. Then, in Appendix C.2, the calculations of the diagonalization matrix are shown. We also show the behavior of the couplings with the expansion of $\mathcal{O}(M_Z/\mu)$ in Appendix C.3. Finally, we calculate the decay widths of the heavy neutralinos and the chargino in Appendix C.4.

C.1 Masses

Here, we calculate the mass eigenvalues of Eq. (4.6).

The mass matrix is written as

$$M_n = \begin{pmatrix} M_1 & -M_Z s_W c_\beta & M_Z s_W s_\beta \\ -M_Z s_W c_\beta & 0 & -\mu \\ M_Z s_W s_\beta & -\mu & 0 \end{pmatrix} . \tag{C.1}$$

The eigenvalues of this matrix, λ, are calculated by solving the following equation,

$$\begin{vmatrix} \lambda - A & -B & -C \\ -B & \lambda & -D \\ -C & -D & \lambda \end{vmatrix} = 0 , \tag{C.2}$$
$$A = M_1,\ B = -M_Z s_W c_\beta,\ C = M_Z s_W s_\beta,\ D = -\mu ,$$

i.e. solving the next equation,

$$\lambda^3 - A\lambda^2 - (B^2 + C^2 + D^2)\lambda + AD^2 - 2BCD = 0 . \tag{C.3}$$

Here, the three solutions of the cubic equation,

$$x^3 + a_2 x^2 + a_1 x + a_0 = 0 , \tag{C.4}$$

can be written as

$$x = u+v-\frac{a_2}{3}\,,\ u\omega_1+v\omega_2-\frac{a_2}{3}\,,\ u\omega_2+v\omega_1-\frac{a_2}{3}\,, \tag{C.5}$$

where

$$\begin{array}{ll} \omega_1=\frac{-1+\sqrt{3}i}{2}\,, & \omega_2=\omega_1^2=\frac{-1-\sqrt{3}i}{2}\,, \\ u=(Q+\sqrt{Q^2+P^3})^{1/3}\,, & v=(Q-\sqrt{Q^2+P^3})^{1/3}\,, \\ Q=-\frac{1}{2}a_0+\frac{1}{6}a_1a_2-\frac{1}{27}a_2^3\,, & P=\frac{1}{3}a_1-\frac{1}{9}a_2^2\,. \end{array} \tag{C.6}$$

Now, the following relations are satisfied,

$$a_2=-M_1\,,\quad a_1=-\mu^2-M_Z^2s_W^2\,,\quad a_0=M_1\mu^2-\mu M_Z^2s_W^2s_{2\beta}\,. \tag{C.7}$$

Thus, from Eq. (C.6), u and v are calculated as

$$\begin{aligned} u^3(v^3) &= -\frac{1}{3}\mu^2M_1+\frac{1}{2}\mu M_Z^2s_W^2s_{2\beta}+\frac{1}{54}M_1\left(2M_1^2+9M_Z^2s_W^2\right) \\ &\quad \pm\frac{1}{3\sqrt{3}}\Big[-\mu^6+\mu^4\left(2M_1^2-3M_Z^2s_W^2\right)-9\mu^3M_1M_Z^2s_W^2s_{2\beta} \\ &\quad -\mu^2\left(M_1^4+5M_1^2M_Z^2s_W^2+3M_Z^4s_W^4\left(1-\frac{9}{4}s_{2\beta}^2\right)\right) \\ &\quad +\mu M_1M_Z^2s_W^2s_{2\beta}\left(M_1^2+\frac{9}{2}M_Z^2s_W^2\right)-\frac{1}{4}M_Z^4s_W^4\left(M_1^2+4M_Z^2s_W^2\right)\Big]^{1/2}. \end{aligned} \tag{C.8}$$

If we expand this solution by M_Zs_W/μ, $u(v)$ becomes as

$$\begin{aligned} u(v) &= \frac{1}{2}\mu\Big[1-\frac{1}{3}z_1\pm i\frac{1}{\sqrt{3}}\left(1+z_1\right) \\ &\quad +\frac{1}{2}z^2\frac{1}{1-z_1}\left(\left(1+s_{2\beta}\right)\pm i\frac{1}{\sqrt{3}}\frac{1}{1+z_1}\left(1-3s_{2\beta}+z_1\left(-3+s_{2\beta}\right)\right)\right)+\mathcal{O}\left(z^4\right)\Big]\,, \end{aligned} \tag{C.9}$$

where

$$z\equiv\frac{M_Zs_W}{\mu},\quad z_1\equiv\frac{M_1}{\mu}\,. \tag{C.10}$$

Then the mass eigenvalues can be written as

$$\begin{aligned} m_1 &= u\omega_2+v\omega_1+\frac{1}{3}M_1 \\ &= M_1\left(1-z^2\frac{1}{1-z_1^2}(1-\frac{1}{z_1}s_{2\beta})+\mathcal{O}\left(z^4\right)\right)\,, \\ m_2 &= u\omega_1+v\omega_2+\frac{1}{3}M_1 \\ &= -\mu\left(1+\frac{1}{2}z^2\frac{1}{1+z_1}(1-s_{2\beta})+\mathcal{O}\left(z^4\right)\right)\,, \\ m_3 &= u+v+\frac{1}{3}M_1 \\ &= \mu\left(1+\frac{1}{2}z^2\frac{1}{1-z_1}(1+s_{2\beta})+\mathcal{O}\left(z^4\right)\right)\,. \end{aligned} \tag{C.11}$$

The relation between $m_{\chi_i^0}$ and these eigenvalues m_i are written in Sec. 4.3 in detail. Note that $|m_i| = m_{\chi_i^0}$ satisfies for $\mu > 0$ and $\mu > M_1$. However, the relation changes as $|m_{2,3}| = m_{\chi^0_{2,3}}$ or $|m_{2,3}| = m_{\chi^0_{3,2}}$ depending on the parameters for $\mu < 0$ and $|\mu| > M_1$: i.e. $|m_2| > |m_3|$ can occur. See also Sec. 4.3 for details.

C.2 Diagonalization Matrix

The diagonalization matrix, a real orthogonal matrix O_n (Eq. (4.7)) with

$$O_n M_n O_n^T = \begin{pmatrix} \epsilon_1 m_{\chi_1^0} & 0 & 0 \\ 0 & \epsilon_2 m_{\chi_2^0} & 0 \\ 0 & 0 & \epsilon_3 m_{\chi_3^0} \end{pmatrix}, \tag{C.12}$$

can be obtained by the following calculations. First, let us define O_n as

$$O_n^T = \begin{pmatrix} a_1^1 & a_1^2 & a_1^3 \\ a_2^1 & a_2^2 & a_2^3 \\ a_3^1 & a_3^2 & a_3^3 \end{pmatrix}. \tag{C.13}$$

Then the three equations can be obtained by Eq. (C.12) as

$$\begin{pmatrix} A & B & C \\ B & 0 & D \\ C & D & 0 \end{pmatrix} \begin{pmatrix} a_1^i \\ a_2^i \\ a_3^i \end{pmatrix} = \epsilon_i m_{\chi_i^0} \begin{pmatrix} a_1^i \\ a_2^i \\ a_3^i \end{pmatrix}. \tag{C.14}$$

We can solve these equations and get the solutions as

$$\begin{pmatrix} a_1^i \\ a_2^i \\ a_3^i \end{pmatrix} = K^i \begin{pmatrix} 1 \\ \frac{\epsilon_i m_{\chi_i^0} B + CD}{m^2_{\chi_i^0} - D^2} \\ \frac{\epsilon_i m_{\chi_i^0} C + BD}{m^2_{\chi_i^0} - D^2} \end{pmatrix} = K^i \begin{pmatrix} 1 \\ \frac{M_Z s_W}{\mu} \frac{y_i c_\beta + s_\beta}{1 - y_i^2} \\ \frac{M_Z s_W}{\mu} \frac{y_i s_\beta + c_\beta}{y_i^2 - 1} \end{pmatrix}, \tag{C.15}$$

where $y_i = \epsilon_i m_{\chi_i^0}/\mu$ and

$$K^i = \frac{|y_i^2 - 1|}{\sqrt{(z_1^2 - 1 + 2z^2) y_i^2 + z^2(z_1 + 3s_{2\beta}) y_i + 1 - z_1^2 + z^2 + z_1 z^2 s_{2\beta}}} \equiv \frac{|y_i^2 - 1|}{X^i}. \tag{C.16}$$

Thus, the solutions can be written as

$$\begin{pmatrix} a_1^i \\ a_2^i \\ a_3^i \end{pmatrix} = \begin{pmatrix} \frac{|y_i^2 - 1|}{X^i} \\ -\mathrm{sign}(y_i^2 - 1) z \frac{y_i c_\beta + s_\beta}{X^i} \\ \mathrm{sign}(y_i^2 - 1) z \frac{y_i s_\beta + c_\beta}{X^i} \end{pmatrix}. \tag{C.17}$$

In the case that $|\mu| > M_1$ and $|\mu| > M_Z$, $y_1^2 < 1$ and $y_2^2, y_3^2 > 1$ are satisfied from Eq. (C.11). In this case, with Eq. (C.11) and the expansion by z, the diagonalizing matrix is shown as

$$
O_n^T = \begin{pmatrix}
1 - \frac{1}{2}z^2 \frac{1}{(1-z_1^2)^2} & z\sqrt{\frac{1-s_{2\beta}}{2}} \frac{1}{1+z_1} & z\sqrt{\frac{1+s_{2\beta}}{2}} \frac{1}{1-z_1} \\
\quad \times \left(1 + 2z_1 s_{2\beta} + z_1^2\right) & & \\
z \frac{1}{1-z_1^2} \left(s_\beta + z_1 c_\beta\right) & -\frac{1}{\sqrt{2}} + \frac{1}{4\sqrt{2}} z^2 \frac{\sqrt{1-s_{2\beta}}}{(1+z_1)^2} & -\frac{1}{\sqrt{2}} + \frac{1}{4\sqrt{2}} z^2 \frac{\sqrt{1+s_{2\beta}}}{(1-z_1)^2} \\
& \quad \times (2s_\beta + z_1(c_\beta + s_\beta)) & \quad \times (2s_\beta + z_1(c_\beta - s_\beta)) \\
-z \frac{1}{1-z_1^2} \left(c_\beta + z_1 s_\beta\right) & -\frac{1}{\sqrt{2}} - \frac{1}{4\sqrt{2}} z^2 \frac{\sqrt{1-s_{2\beta}}}{(1+z_1)^2} & \frac{1}{\sqrt{2}} + \frac{1}{4\sqrt{2}} z^2 \frac{\sqrt{1+s_{2\beta}}}{(1-z_1)^2} \\
& \quad \times (2c_\beta + z_1(c_\beta + s_\beta)) & \quad \times (-2c_\beta + z_1(c_\beta - s_\beta))
\end{pmatrix} \\
+ \mathcal{O}\left(z^3\right) , \tag{C.18}
$$

Here, we choose the relation $|m_{2,3}| = m_{\chi^0_{2,3}}$. When the order of $|m_2|, |m_3|$ changes as $|m_{2,3}| = m_{\chi^0_{3,2}}$, the above expression of O_n^T should be changed as $\left(O_n^T\right)_{i2} \leftrightarrow \left(O_n^T\right)_{i3}$ (see also Sec. 4.3).

C.3 Couplings

Here, we show all the couplings in Eq. (4.9) $\sim$ (4.13) with the expansion by z using the results of Appendix C.1 and C.2. See also the Lagrangian (4.8). The couplings are shown in the relation $|m_{2,3}| = m_{\chi^0_{2,3}}$. When the order of $|m_2|, |m_3|$ changes as $|m_{2,3}| = m_{\chi^0_{3,2}}$, these expression should be read as $\lambda^X_{Y12} \leftrightarrow \lambda^X_{Y13}$ and $\lambda^X_{Y22} \leftrightarrow \lambda^X_{Y33}$ (see also Sec. 4.3).

h couplings

$$\lambda^h_{Lij} = -\frac{1}{2}g'\left(O_n\right)_{i1}\left(c_\alpha\left(O_n\right)_{j3} + s_\alpha\left(O_n\right)_{j2}\right)\eta_i^*\eta_j^*, \tag{C.19}$$

$$\lambda^h_{L11} = \frac{1}{2}g'z\frac{1}{1-z_1^2}\left(z_1 + s_{2\beta}\right) + \mathcal{O}\left(z^3\right), \tag{C.20}$$

$$\lambda^h_{L22} = \frac{1}{4}g'z\epsilon_2\frac{1}{1+z_1}\left(1 - s_{2\beta}\right) + \mathcal{O}\left(z^3\right), \tag{C.21}$$

$$\lambda^h_{L33} = -\frac{1}{4}g'z\epsilon_3\frac{1}{1-z_1}\left(1 + s_{2\beta}\right) + \mathcal{O}\left(z^3\right), \tag{C.22}$$

$$\lambda^h_{L12} = \frac{1}{2}g'\eta_2^*\sqrt{\frac{1-s_{2\beta}}{2}} + \mathcal{O}\left(z^2\right), \tag{C.23}$$

$$\lambda^h_{L13} = -\frac{1}{2}g'\eta_3^*\sqrt{\frac{1+s_{2\beta}}{2}} + \mathcal{O}\left(z^2\right), \tag{C.24}$$

$$\lambda^h_{L21} = \frac{1}{2}g'\eta_2^*\sqrt{\frac{1-s_{2\beta}}{2}}z^2\frac{1}{(1-z_1^2)(1+z_1)}(z_1 + s_{2\beta}) + \mathcal{O}\left(z^4\right), \tag{C.25}$$

$$\lambda^h_{L31} = -\frac{1}{2}g'\eta_3^*\sqrt{\frac{1+s_{2\beta}}{2}}z^2\frac{1}{(1-z_1^2)(1-z_1)}(z_1 + s_{2\beta}) + \mathcal{O}\left(z^4\right), \tag{C.26}$$

$$\lambda^h_{L23} = \frac{1}{4}ig'|c_{2\beta}|z\frac{1}{1+z_1} + \mathcal{O}\left(z^3\right), \tag{C.27}$$

$$\lambda^h_{L32} = -\frac{1}{4}ig'|c_{2\beta}|z\frac{1}{1-z_1} + \mathcal{O}\left(z^3\right). \tag{C.28}$$

Note that $\lambda^h_{Rij} = \left(\lambda^h_{Lji}\right)^*$ and $c_{2\beta} \leq 0$ for $1 \leq \tan\beta$.

Z couplings

$$\lambda^Z_{Lij} = \frac{e}{s_{2W}}\eta_i\eta_j^*\left(\left(O_n\right)_{i3}\left(O_n\right)_{j3} - \left(O_n\right)_{i2}\left(O_n\right)_{j2}\right), \tag{C.29}$$

$$\lambda^Z_{L11} = \frac{e}{s_{2W}}c_{2\beta}z^2\frac{1}{1-z_1^2} + \mathcal{O}\left(z^4\right), \tag{C.30}$$

$$\lambda^Z_{L22} = -\frac{e}{2s_{2W}}c_{2\beta}z^2\frac{1}{1+z_1} + \mathcal{O}\left(z^4\right), \tag{C.31}$$

$$\lambda^Z_{L33} = -\frac{e}{2s_{2W}}c_{2\beta}z^2\frac{1}{1-z_1} + \mathcal{O}\left(z^4\right), \tag{C.32}$$

$$\lambda^Z_{L12} = \frac{e}{s_{2W}}\eta_2^*\sqrt{\frac{1+s_{2\beta}}{2}}z\frac{1}{1-z_1} + \mathcal{O}\left(z^3\right), \tag{C.33}$$

$$\lambda^Z_{L13} = \frac{e}{s_{2W}}\eta_3^*\sqrt{\frac{1+s_{2\beta}}{2}}z\frac{1}{1+z_1} + \mathcal{O}\left(z^3\right), \tag{C.34}$$

$$\lambda^Z_{L23} = \frac{e}{s_{2W}}\eta_2\eta_3^* + \mathcal{O}\left(z^2\right). \tag{C.35}$$

Note that $\lambda^Z_{Lij} = \left(\lambda^Z_{Lji}\right)^*$.

W couplings

$$\lambda^W_{L1i} = -\frac{1}{\sqrt{2}} g \eta_i^* \left(O_n\right)_{i3} , \tag{C.36}$$

$$\lambda^W_{R1i} = \frac{1}{\sqrt{2}} g \epsilon_\mu \eta_i \left(O_n\right)_{i2} , \tag{C.37}$$

$$\lambda^W_{L11} = \frac{1}{\sqrt{2}} g z \frac{1}{1-z_1^2} \left(c_\beta + z_1 s_\beta\right) + \mathcal{O}\left(z^3\right) , \tag{C.38}$$

$$\lambda^W_{R11} = \frac{1}{\sqrt{2}} g \epsilon_\mu z \frac{1}{1-z_1^2} \left(s_\beta + z_1 c_\beta\right) + \mathcal{O}\left(z^3\right) , \tag{C.39}$$

$$\lambda^W_{L12} = \frac{1}{2} g \eta_2^* + \mathcal{O}\left(z^2\right) , \tag{C.40}$$

$$\lambda^W_{R12} = -\frac{1}{2} g \eta_2 \epsilon_\mu + \mathcal{O}\left(z^2\right) , \tag{C.41}$$

$$\lambda^W_{L13} = -\frac{1}{2} g \eta_3^* + \mathcal{O}\left(z^2\right) , \tag{C.42}$$

$$\lambda^W_{R13} = -\frac{1}{2} g \eta_3 \epsilon_\mu + \mathcal{O}\left(z^2\right) . \tag{C.43}$$

C.4 Decay Width

The decay widths of the heavy neutralinos $\chi^0_{2,3}$ and the chargino $\chi^\pm_1$ can be calculated from the Lagrangian (4.8). Here, we assume the relation $|m_{2,3}| = m_{\chi^0_{2,3}}$. When the flip occurs, change the couplings as $\lambda^X_{Y12} \leftrightarrow \lambda^X_{Y13}$ (see also Appendix C.3 and Sec. 4.3).

The decay width of the chargino which decays to the DM and the W boson only is calculated as

$$\begin{aligned} \Gamma_{\chi^\pm_1} &= \Gamma(\chi^\pm_1 \to W^\pm \chi^0_1) = \frac{1}{32\pi} m_{\chi^\pm_1} \left(1-(y_1-w)^2\right)^{1/2} \left(1-(y_1+w)^2\right)^{1/2} \\ &\times \left(\left(|\lambda^W_{L11}|^2 + |\lambda^W_{R11}|^2\right) \left(1 + y_1^2 - 2w^2 + \frac{(1-y_1^2)^2}{w^2}\right) - 6 y_1 \left(\lambda^W_{L11} \left(\lambda^W_{R11}\right)^\dagger + \left(\lambda^W_{L11}\right)^\dagger \lambda^W_{R11}\right) \right) , \end{aligned} \tag{C.44}$$

where $y_1 = m_{\chi^0_1}/m_{\chi^\pm_1}, w = M_W/m_{\chi^\pm_1}$ (see also Appendix D.4). Note that $m_{\chi^\pm_1} = \epsilon_\mu \mu$ and we assume $m_{\chi^\pm_1} > m_{\chi^0_1} + M_W$. The heavy neutralinos can decay in two ways, $\chi^0_{2,3} \to Z\chi^0_1$ and

$\chi^0_{2,3} \to h\chi^0_1$. Each partial decay width can be calculated as

$$\begin{aligned}
\Gamma(\chi^0_{2,3} \to Z\chi^0_1) &= \frac{\left|\lambda^Z_{L12,L13}\right|^2}{16\pi} m_{\chi^0_{2,3}} \left(1-(r^1_{2,3}-r^z_{2,3})^2\right)^{1/2} \left(1-(r^1_{2,3}+r^z_{2,3})^2\right)^{1/2} \\
&\quad \times \left(1+6\epsilon_{2,3}r^1_{2,3}+(r^1_{2,3})^2-2(r^z_{2,3})^2+\frac{(1-(r^1_{2,3})^2)^2}{(r^z_{2,3})^2}\right), \qquad \text{(C.45)} \\
&\quad \text{for } m_{\chi^0_{2,3}} > m_{\chi^0_1}+M_Z\,, \\
\Gamma(\chi^0_{2,3} \to h\chi^0_1) &= \frac{\left|\lambda^h_{L12,L13}+\left(\lambda^h_{R12,R13}\right)^\dagger\right|^2}{16\pi} m_{\chi^0_{2,3}} \left(1-(r^1_{2,3}-r^h_{2,3})^2\right)^{1/2} \\
&\quad \times \left(1-(r^1_{2,3}+r^h_{2,3})^2\right)^{1/2} \left((1+\epsilon_{2,3}r^1_{2,3})^2-(r^h_{2,3})^2\right), \qquad \text{(C.46)} \\
&\quad \text{for } m_{\chi^0_{2,3}} > m_{\chi^0_1}+m_h\,,
\end{aligned}$$

where $r^1_{2,3} = m_{\chi^0_1}/m_{\chi^0_{2,3}}, r^z_{2,3} = m_Z/m_{\chi^0_{2,3}}, r^h_{2,3} = m_h/m_{\chi^0_{2,3}}$. The total decay width depends on whether the decay can occur or not,

$$\begin{aligned}
\Gamma_{\chi^0_{2,3}} &= \Gamma(\chi^0_{2,3} \to Z\chi^0_1)\,, \qquad \text{for } m_{\chi^0_1}+m_h > m_{\chi^0_{2,3}} > m_{\chi^0_1}+M_Z\,, \qquad \text{(C.47)} \\
&= \Gamma(\chi^0_{2,3} \to Z\chi^0_1)+\Gamma(\chi^0_{2,3} \to h\chi^0_1)\,, \quad \text{for } m_{\chi^0_{2,3}} > m_{\chi^0_1}+m_h\,. \qquad \text{(C.48)}
\end{aligned}$$

The z expansions for the decay widths in the case $\mu > 0$ with using the results of Appendix C.1 and C.3 become as

$$\begin{aligned}
\Gamma_{\chi^\pm_1} &= \frac{1}{64\pi} g^2 t_W^2 |\mu| (1-z_1^2)(1+2z_1 s_{2\beta}+z_1^2) + \mathcal{O}(z^2)\,, \qquad \text{(C.49)} \\
\Gamma(\chi^0_{2,3} \to Z\chi^0_1) &= \frac{1}{128\pi} g'^2 |\mu| (1\pm 2s_{2\beta})(1\mp z_1)(1\pm z_1)^3 + \mathcal{O}(z^2)\,, \qquad \text{(C.50)} \\
\Gamma(\chi^0_{2,3} \to h\chi^0_1) &= \frac{1}{128\pi} g'^2 |\mu| (1\mp 2s_{2\beta})(1\pm z_1)(1\mp z_1)^3 + \mathcal{O}(z^2)\,, \qquad \text{(C.51)} \\
\Gamma(\chi^0_{2,3} \to Z\chi^0_1) &+ \Gamma(\chi^0_{2,3} \to h\chi^0_1) \\
&= \frac{1}{64\pi} g'^2 |\mu| (1-z_1^2)(1+2z_1 s_{2\beta}+z_1^2) + \mathcal{O}(z^2)\,. \qquad \text{(C.52)}
\end{aligned}$$

The results for the case $\mu < 0$ are similar to these expressions.

The branching ratio of the process $\chi^0_{2,3} \to Z\chi^0_1$ can be obtained as follows.

$$\begin{aligned}
\mathrm{Br}(\chi^0_{2,3} \to Z\chi^0_1) &= \frac{\Gamma(\chi^0_{2,3} \to Z\chi^0_1)}{\Gamma_{\chi^0_{2,3}}} \\
&= 1.0\,, \qquad \text{for } m_{\chi^0_1}+m_h > m_{\chi^0_{2,3}} > m_{\chi^0_1}+M_Z\,, \qquad \text{(C.53)} \\
&= \frac{1}{2}(1\pm z_1)^2(1\pm s_{2\beta})\frac{1}{1+2z_1 s_{2\beta}+z_1^2} + \mathcal{O}(z^2)\,, \\
&\qquad \text{for } m_{\chi^0_{2,3}} > m_{\chi^0_1}+m_h\,. \qquad \text{(C.54)}
\end{aligned}$$

Appendix D

Calculations

Here, we show the detailed calculations whose results are used in the text. The annihilation cross section used in Sec. 5.1 is calculated in Appendix D.1. The calculations for the spin independent and spin dependent scattering cross sections (used in Sec. 5.2 and 5.3) are shown in Appendix D.2 and D.3. The decay width used in Sec. 5.4 and Appendix C.4 is also calculated in Appendix D.4.

D.1 Annihilation Cross Section

We show the calculations of the annihilation cross sections which are used in Sec. 5.1. First, we calculate the annihilation cross section for the process $\chi_1^0\chi_1^0 \to h \to$ SMs. Here, we use the optical theorem,

$$\sum_f \sigma\left(\chi_1^0\chi_1^0 \to h \to f\right) = \frac{\text{Im } M(\chi_1^0\chi_1^0 \to h \to \chi_1^0\chi_1^0)}{2E_{\text{CM}}p_{\text{CM}}}\,, \tag{D.1}$$

where f denotes all possible states and M is the amplitude of the forward scattering. Note that E_{CM} and p_{CM} are the energy and the momentum of the DM in the center of the mass frame,

$$s = 4\left(m_{\chi_1^0}^2 + p_{CM}^2\right) = E_{CM}^2\,, \tag{D.2}$$

$$2E_{CM}p_{CM} = \sqrt{s}\sqrt{s - 4m_{\chi_1^0}^2}\,. \tag{D.3}$$

The spin averaged amplitude of the forward scattering $M(\chi_1^0(p_1)\chi_1^0(p_2) \to h \to \chi_1^0(p_1)\chi_1^0(p_2))$ can be calculated with the Lagrangian $L \ni \frac{1}{2}h\lambda^h\bar{\psi}_{\chi_1^0}\psi_{\chi_1^0}$ as

$$\begin{aligned}&\frac{1}{2}\frac{1}{2}\sum_{spin} M(\chi_1^0(p_1)\chi_1^0(p_2) \to h \to \chi_1^0(p_1)\chi_1^0(p_2))\\ &= \frac{(\lambda^h)^2}{2}\left(s - 4m_{\chi_1^0}^2\right)\frac{-(s - m_h^2) + is\Gamma_h/m_h}{\left(s - m_h^2\right)^2 + s^2\Gamma_h^2/m_h^2}\,,\end{aligned} \tag{D.4}$$

where Γ_h is the total width of the Higgs boson. Thus, the annihilation cross section for the Higgs boson exchange process can be calculated as

$$\sum_f \sigma\left(\chi_1^0\chi_1^0 \to h \to f\right) = \frac{(\lambda_1^h)^2}{2}\sqrt{1-\frac{4m_{N1}^2}{s}}\frac{s\Gamma_h/m_h}{\left(s-m_h^2\right)^2+s^2\Gamma_h^2/m_h^2}\,. \tag{D.5}$$

Note that since the term $s^2\Gamma_h^2/m_h^2$ in the denominator is effective only when $s \sim m_h^2$, the approximation of $s^2\Gamma_h^2/m_h^2 \to m_h^2\Gamma_h^2$ in the denominator does not change the cross section.

Next, let us calculate the Z boson exchange process $\chi_1^0\chi_1^0 \to Z \to$ SMs. Here, we can write the Lagrangian as

$$L \ni \lambda^Z \bar{\psi}_{\chi_1^0}\gamma^\mu P_L \psi_{\chi_1^0} Z_\mu + \sum_f \bar{\psi}_f \gamma^\mu \left(C_V^f - C_A^f\gamma_5\right)\psi_f Z_\mu\,, \tag{D.6}$$

where ψ_f denotes the SM fermions and C_V^f, C_A^f are couplings with $C_V^f = -\frac{g}{2c_W}(T_{3f} - 2s_W^2 Q_f)$, $C_A^f = -\frac{g}{2c_W}T_{3f}$. T_{3f} is $\frac{1}{2}$ $(-\frac{1}{2})$ for up (down) type fermions and Q_f is the electric charge for the particle f. Then the cross section of the process $\chi_1^0\chi_1^0 \to Z \to$ SMs can be calculated as

$$\begin{aligned}
\sum_f \sigma(\chi_1^0\chi_1^0 \to Z \to f\bar{f}) &= \frac{1}{16\pi}\frac{1}{s}\left(1-\frac{4m_{\chi_1^0}^2}{s}\right)^{-1/2}\sum_f N_{c,f}\sqrt{1-\frac{4m_f^2}{s}}F_f(s)\,, \\
F_f(s) &= \frac{4}{3}\frac{(\lambda^Z)^2}{(s-M_Z^2)^2+M_Z^2\Gamma_Z^2}\Big[12|C_A^f|^2\frac{m_{\chi_1^0}^2 m_f^2}{M_Z^4}(s-M_Z^2)^2 \\
&\quad + \left(|C_V^f|^2(s+2m_f^2)+|C_A^f|^2(s-4m_f^2)\right)(s-4m_{\chi_1^0}^2)\Big]\,.
\end{aligned} \tag{D.7}$$

Here, $N_{c,f} = 1, 3$ for the leptons and the quarks. If we neglect the term proportional to m_f^2, the cross section becomes

$$\begin{aligned}
&\sum_f \sigma(\chi_1^0\chi_1^0 \to Z \to f\bar{f}) \\
&\quad = (\lambda^Z)^2\sqrt{1-\frac{4m_{\chi_1^0}^2}{s}}\frac{s\Gamma_Z/M_Z}{(s-m_Z^2)^2+M_Z^2\Gamma_Z^2}\frac{1}{\Gamma_Z}\frac{1}{12\pi}M_Z\sum_f N_{c,f}\left(|C_V^f|^2+|C_A^f|^2\right)\,.
\end{aligned} \tag{D.8}$$

Then we use the relation of the total decay width of the Z boson,

$$\Gamma_Z = \frac{1}{12\pi}M_Z\sum_f N_{c,f}\left(|C_V^f|^2+|C_A^f|^2\right)\,, \tag{D.9}$$

and the cross section becomes

$$\sum_f \sigma(\chi_1^0\chi_1^0 \to Z \to f\bar{f}) = (\lambda^Z)^2\sqrt{1-\frac{4m_{\chi_1^0}^2}{s}}\frac{s\Gamma_Z/M_Z}{(s-M_Z^2)^2+M_Z^2\Gamma_Z^2}\,. \tag{D.10}$$

The non vanishing terms in the limit $v \to 0$ ($s \to 4m^2_{\chi^0_1}$) which are proportional to m_f^2 and neglected above are also calculated as

$$\begin{aligned}\sigma_{v\to 0} &= \frac{1}{\pi}(\lambda^Z)^2 \frac{(s-M_Z^2)^2}{(s-M_Z^2)^2+M_Z^2\Gamma_Z^2}\frac{m^2_{\chi^0_1}}{M_Z^4}\frac{1}{s}\left(1-\frac{4m^2_{\chi^0_1}}{s}\right)^{-1/2} \\ &\quad \times \sum_f N_{c,f}|C_A^f|^2 m_f^2 \sqrt{1-\frac{4m_f^2}{s}}\,. \end{aligned} \tag{D.11}$$

D.2 Spin Independent Scattering Cross Section

We calculate the spin independent scattering cross section in the Higgs boson exchange process (see Sec. 5.2). After integrating out the top quark, the relevant terms are given as

$$L \ni -\frac{1}{2}m_h^2 h^2 - \frac{1}{\sqrt{2}}\sum_i Y_i h\bar{\psi}_{q_i}\psi_{q_i} + \frac{\alpha_s}{12\sqrt{2}\pi v}hG_{\mu\nu}G^{\mu\nu} + \frac{1}{2}\lambda^h h\bar{\psi}_{\chi^0_1}\psi_{\chi^0_1}\,, \tag{D.12}$$

where q_i denotes the quark except the top and $G^{\mu\nu}$ is the field strength of the gluon. If we integrate out the Higgs boson, this Lagrangian becomes

$$\begin{aligned} L &\ni -\frac{\lambda^h}{2\sqrt{2}m_h^2}\bar{\psi}_{\chi^0_1}\psi_{\chi^0_1}\sum_i\left(Y_i\bar{\psi}_{q_i}\psi_{q_i}\right) + \frac{\alpha_s\lambda^h}{24\sqrt{2}\pi v m_h^2}\bar{\psi}_{\chi^0_1}\psi_{\chi^0_1}G_{\mu\nu}G^{\mu\nu} \\ &= c_N\bar{\psi}_{\chi^0_1}\psi_{\chi^0_1}\left(\sum_i\left(m_{q_i}\bar{\psi}_{q_i}\psi_{q_i}\right) - \frac{\alpha_s}{12\pi}G_{\mu\nu}G^{\mu\nu}\right), \quad c_N = -\frac{\lambda^h}{2\sqrt{2}m_h^2 v}\,. \end{aligned} \tag{D.13}$$

We used the relation $m_{q_i} = Y_i v$. To calculate the scattering with the nucleon, we consider the quark/gluon contribution to the nucleon state

$$\langle N|m_{q_i}\bar{\psi}_{q_i}\psi_{q_i}|N\rangle = m_N f_q\,, \tag{D.14}$$

$$-\frac{9\alpha_s}{8\pi}\langle N|G_{\mu\nu}G^{\mu\nu}|N\rangle = m_N f_g\,. \tag{D.15}$$

From the trace anomaly, the following relation is satisfied [112]

$$\begin{aligned} m_N &= \langle N|T^\mu_\mu|N\rangle = -\frac{9\alpha_s}{8\pi}\langle N|G_{\mu\nu}G^{\mu\nu}|N\rangle + \sum_{q=u,d,s}\langle N|m_{q_i}\bar{\psi}_{q_i}\psi_{q_i}|N\rangle\,, \\ &\to 1 = f_g + \sum_{q=u,d,s} f_q\,. \end{aligned} \tag{D.16}$$

Here, we define f_N as

$$\begin{aligned} f_N &\equiv \langle N|\sum_i\left(m_{q_i}\bar{\psi}_{q_i}\psi_{q_i}\right) - \frac{\alpha_s}{12\pi}G_{\mu\nu}G^{\mu\nu}|N\rangle/m_N \\ &= \langle N|\sum_{q=u,d,s}\left(m_{q_i}\bar{\psi}_{q_i}\psi_{q_i}\right) - \frac{\alpha_s}{4\pi}G_{\mu\nu}G^{\mu\nu}|N\rangle/m_N \\ &= \sum_{q=u,d,s} f_q + \frac{2}{9}f_g = \frac{2}{9} + \frac{7}{9}\sum_{q=u,d,s} f_q\,. \end{aligned} \tag{D.17}$$

We used the relation $\langle N|m_q\bar{\psi}_{q_i}\psi_{q_i}|N\rangle = -\frac{\alpha_s}{12\pi}\langle N|G_{\mu\nu}G^{\mu\nu}|N\rangle$ for $q_i = c, b$ [112]. Note that Eq. (D.13) is a Lagrangian at the scale $\sim m_h$ (~ 125 GeV) and Eq. (D.17) is the relation at the scale $\sim m_N$ (~ 1 GeV). The value of α_s depends on the scale strongly, e.g. $\alpha_s(M_Z) \simeq 0.12$ and $\alpha_s(m_\tau) \simeq 0.33$ [63] where $M_Z \simeq 91.2$ GeV and $m_\tau \simeq 1.78$ GeV [63]. However, the operator $\alpha_s G_{\mu\nu}G^{\mu\nu}$ is scale independent at the leading order [113]. Thus, the scale dependence of Eq. (D.13) seems not to be large and we do not include the effects of the renormalization group running. Then the cross section for the process $\chi_1^0(p_A)N(p_B) \to \chi_1^0(p_1)N(p_2)$ can be calculated as follows,

$$d\sigma = \frac{(2\pi)^4\delta^4(\sum_k p_k - p_A - p_B)}{2E_A 2E_B|v_A - v_B|}\prod_{k=1}^{n}\frac{d^3p_k}{(2\pi)^3 2E_k}|M_{fi}|^2\,, \tag{D.18}$$

where

$$|M|^2 \;=\; 16c_N^2 f_N^2 m_N^2\left(p_1\cdot p_A + m_{\chi_1^0}^2\right)\left(p_2\cdot p_B + m_N^2\right)\,. \tag{D.19}$$

The cross section becomes

$$\sigma \;=\; \int d\sigma = \frac{c_N^2 f_N^2 m_N^2(2m_{\chi_1^0}^2 + |p|^2)(2m_N^2 + |p|^2)}{\pi(E_A + E_B)^2}\,, \tag{D.20}$$

where we consider in the center of mass frame ($p_A = (E_A, 0, 0, p)$). Now, since the velocity of the DM is small $v \sim 0.001c$, we neglect the momentum and the cross section can be written as

$$\sigma \;=\; \frac{4c_N^2 f_N^2 m_N^4 m_{\chi_1^0}^2}{\pi(m_{\chi_1^0} + m_N)^2}\,. \tag{D.21}$$

D.3 Spin Dependent Scattering Cross Section

Next, we calculate the spin dependent scattering cross section in the Z boson exchange process (see Sec. 5.3). We assume the following Lagrangian,

$$L \;\ni\; \frac{1}{2}M_Z^2 Z_\mu Z^\mu - \frac{e}{s_{2W}}\sum_i \bar{\psi}_{q_i}\gamma^\mu\left(2T_{qi}^3 P_L - 2s_W^2 Q_{qi}\right)\psi_{q_i}Z_\mu + \lambda^Z\bar{\psi}_{\chi_1^0}\gamma^\mu P_L\psi_{\chi_1^0}Z_\mu\,. \tag{D.22}$$

After integrating out the Z boson, this Lagrangian becomes

$$\begin{aligned} L \;&\ni\; \frac{e\lambda^Z}{s_{2W}M_Z^2}\bar{\psi}_{\chi_1^0}\gamma^\mu P_L\psi_{\chi_1^0}\sum_i\bar{\psi}_{q_i}\gamma_\mu\left(2T_{qi}^3P_L - 2s_W^2Q_{qi}\right)\psi_{q_i} \\ &\ni\; d_N\bar{\psi}_{\chi_1^0}\gamma^\mu\gamma_5\psi_{\chi_1^0}\sum_i\bar{\psi}_{q_i}\gamma_\mu\gamma_5 T_{qi}^3\psi_{q_i}\,,\quad d_N = \frac{e\lambda^Z}{2s_{2W}M_Z^2}\,. \end{aligned} \tag{D.23}$$

Note that $\bar{\psi}_{\chi_1^0}\gamma^\mu\psi_{\chi_1^0} = 0$ for the Majorana fermions. We neglected the terms $\bar{\psi}_{\chi_1^0}\gamma^\mu\gamma_5\psi_{\chi_1^0}\bar{\psi}_{q_i}\gamma_\mu\psi_{q_i}$ since they vanish in the limit of the zero momentum transfer. As is the same case of the SI scattering cross section, we consider the quark/gluon spin contribution to the neutron state

$$\langle N|\bar{\psi}_{q_i}\gamma_\mu\gamma_5\psi_{q_i}|N\rangle \;=\; 2s_\mu\Delta_q^N\,, \tag{D.24}$$

where s_μ is the spin vector of the nucleon and Δ_q^N is the quark contribution to the nucleon spin. Then the cross section is calculated as

$$\sigma^{SD} = \frac{12\xi_N^2 m_N^2}{\pi} \frac{m_{\chi_1^0}^2}{(m_{\chi_1^0} + m_N)^2}, \quad \xi_N = d_N \sum_{u,d,s} T_q^3 \Delta_q^N \,, \tag{D.25}$$

in the zero momentum limit. Here, we neglect the contributions from the heavy quarks (c, b, t) since they are small enough [114].

D.4 Decay Width

Here, we briefly calculate the decay rates in generic expressions. These results are used in Sec. 5.4 and Appendix C.4.

The differential decay rate (at the rest frame) of particle A to n particles (k=1,$\cdots$ n) can be written as

$$d\Gamma = \frac{(2\pi)^4 \delta^4(\sum_k p_k - p_A)}{2m_A} \prod_{k=1}^{n} \frac{d^3 p_k}{(2\pi)^3 2E_k} |M|^2 \,, \tag{D.26}$$

where M is the transition amplitude.
Here, we assume that the scalars have no color and the fermions have N_c color ($N_c = 1$ for non-colored particle.)

- $\phi \to \psi_M \psi_M$
  First, let us consider the process that the particle A (real scalar) decays to two Bs (Majorana fermions). We assume $m_A > 2m_B$ and the interacting term as

  $$L_{int} = \frac{1}{2} \lambda \phi_A \bar{\psi}_B \psi_B \,. \tag{D.27}$$

  From this Lagrangian, the squared matrix element (spin summed) can be calculated as

  $$|M|^2 \;=\; 2N_C \lambda^2 \left(m_A^2 - 4m_B^2\right) \,. \tag{D.28}$$

  Note that this is the same results as the one with the Dirac fermions. However, the decay rate Γ should be divided by two since two final state particle is identical,

  $$\begin{aligned} \Gamma &= \frac{1}{2} \int d\Gamma = \frac{1}{2} \int \frac{(2\pi)^4 \delta^4(\sum_k p_k - p_A)}{2m_A} \frac{2N_C \lambda^2 \left(m_A^2 - 4m_B^2\right)}{(2\pi)^6 2E_1 2E_2} d^3 p_1 d^3 p_2 \\ &= \frac{N_C \lambda^2}{16\pi} m_A \left(1 - 4b^2\right)^{3/2} \,, \end{aligned} \tag{D.29}$$

  where $b = m_B / m_A$.

- $Z_\mu \to \psi_M \psi_M$
  Next, let us consider the process that particle Z (real vector boson) decays to two Bs (Majorana fermions). We assume $m_Z > 2m_B$ and the interacting term as

  $$L_{int} = \lambda \bar{\psi}_B \gamma^\mu P_L \psi_B Z_\mu \,. \tag{D.30}$$

The squared matrix element (spin summed) can be calculated as

$$|M|^2 = \frac{4}{3}N_C\lambda^2\left(m_Z^2 - 4m_B^2\right) . \tag{D.31}$$

The decay rate Γ is

$$\Gamma = \frac{1}{2}\int d\Gamma = \frac{N_C\lambda^2}{24\pi}m_Z\left(1-4b^2\right)^{3/2} , \tag{D.32}$$

where $b = m_B/m_A$ and note that the division by two is necessary.

- $\psi_{DA} \to \psi_{MB}W$

  Next, let us consider the process that particle A (Dirac fermion) decays to particle B (Majorana fermion) and particle W (charged vector boson). We assume $m_A > m_B + m_W$ and the interacting term as

$$L_{int} = \bar{\psi}_{MB}\gamma^\mu\left(\lambda_L P_L + \lambda_R P_R\right)\psi_{DA}W_\mu^- + h.c.. \tag{D.33}$$

  The squared matrix element (spin summed) is calculated as

$$\begin{aligned} |M|^2 &= \frac{1}{2}\left(|\lambda_L|^2 + |\lambda_R|^2\right)\left(m_A^2 + m_B^2 - 2m_W^2 + \frac{(m_A^2 - m_B^2)^2}{m_W^2}\right) \\ &\quad -3m_A m_B\left(\lambda_L\lambda_R^\dagger + \lambda_R\lambda_L^\dagger\right) . \end{aligned} \tag{D.34}$$

  The decay rate Γ is

$$\begin{aligned} \Gamma &= \int d\Gamma = \frac{1}{32\pi}m_A\left(1-(b-w)^2\right)^{1/2}\left(1-(b+w)^2\right)^{1/2} \\ &\quad \times\left(\left(|\lambda_L|^2 + |\lambda_R|^2\right)\left(1 + b^2 - 2w^2 + \frac{(1-b^2)^2}{w^2}\right) - 6b\left(\lambda_L\lambda_R^\dagger + \lambda_R\lambda_L^\dagger\right)\right) , \end{aligned} \tag{D.35}$$

  where $b = m_B/m_A, w = m_W/m_A$.

- $\psi_{MA} \to \psi_{MB}Z$

  Next, let us consider the process that particle A (Majorana fermion) decays to particle B (Majorana fermion) and particle Z (real vector boson). We assume $m_A > m_B + m_Z$ and the interacting term as

$$L_{int} = \lambda\bar{\psi}_{MB}\gamma^\mu P_L\psi_{MA}Z_\mu + h.c.. \tag{D.36}$$

  The squared matrix element (spin summed) is calculated as

$$|M|^2 = |\lambda|^2\left(m_A^2 + m_B^2 - 2m_Z^2 + \frac{(m_A^2 - m_B^2)^2}{m_Z^2}\right) + 3(\lambda^2 + (\lambda^\dagger)^2)m_A m_B . \tag{D.37}$$

  The decay rate Γ is

$$\begin{aligned} \Gamma &= \int d\Gamma = \frac{1}{16\pi}m_A\left(1-(b-z)^2\right)^{1/2}\left(1-(b+z)^2\right)^{1/2} \\ &\quad \times\left(|\lambda|^2\left(1 + b^2 - 2z^2 + \frac{(1-b^2)^2}{z^2}\right) + 3b(\lambda^2 + (\lambda^\dagger)^2)\right) , \end{aligned} \tag{D.38}$$

  where $b = m_B/m_A, z = m_Z/m_A$.

- $\psi_{MA} \to \psi_{MB} h$

  Finally, let us consider the process that particle A (Majorana fermion) decays to particle B (Majorana fermion) and particle h (real boson). We assume $m_A > m_B + m_h$ and the interacting term as

$$L_{int} = h\bar{\psi}_{MB}(\lambda_L P_L + \lambda_R P_R)\psi_{MA} + h.c.\,. \tag{D.39}$$

  The squared matrix element (spin summed) can be calculated as

$$\begin{aligned} |M|^2 &= \left(|\lambda_L|^2 + |\lambda_R|^2 + \lambda_L\lambda_R + \lambda_L^\dagger\lambda_R^\dagger\right)(m_A^2 + m_B^2 - m_h^2) \\ &\quad + m_A m_B\left((\lambda_L)^2 + (\lambda_R)^2 + (\lambda_L^\dagger)^2 + (\lambda_R^\dagger)^2 + 2\lambda_L^\dagger\lambda_R + 2\lambda_L\lambda_R^\dagger\right). \end{aligned} \tag{D.40}$$

  The decay rate Γ is

$$\begin{aligned} \Gamma &= \int d\Gamma = \frac{1}{16\pi} m_A \left(1 - (b-h)^2\right)^{1/2}\left(1 - (b+h)^2\right)^{1/2} \\ &\quad \times\Big[\left(|\lambda_L|^2 + |\lambda_R|^2 + \lambda_L\lambda_R + \lambda_L^\dagger\lambda_R^\dagger\right)(1 + b^2 - h^2) \\ &\quad + b\left((\lambda_L)^2 + (\lambda_R)^2 + (\lambda_L^\dagger)^2 + (\lambda_R^\dagger)^2 + 2\lambda_L^\dagger\lambda_R + 2\lambda_L\lambda_R^\dagger\right)\Big] \end{aligned} \tag{D.41}$$

  where $b = m_B/m_A, h = m_h/m_A$.

Appendix E

Validation of the LHC Analysis

In this appendix, we show the validation of our analysis for the heavy neutralinos/chargino searches at the LHC. We show the 8 TeV analysis in Appendix E.1 and the 14 TeV analysis in Appendix E.2. See also Sec. 5.5.

E.1 8 TeV

Here, we show the validation of our 8 TeV analysis. See also Sec. 5.5.1. To compare with the ATLAS results, we use the pure Bino-Wino model. First, we show the cut flows of some SRs. We check the following two model points which are validated by the CheckMATE collaboration [115]

$$(m_{\chi_2^0}, m_{\chi_1^\pm}, m_{\chi_1^0}) = (175, 175, 100), (350, 350, 50)\ \text{GeV}\,. \tag{E.1}$$

Here, we assume $\mathrm{Br}(\chi_1^\pm \to W^\pm \chi_1^0) = \mathrm{Br}(\chi_j^0 \to Z\chi_1^0) = 1$ for kinematically allowed region, and $\mathrm{Br}(\chi_1^\pm \to W^{\pm *}\chi_1^0 \to l\nu\chi_1^0) = \mathrm{Br}(W^\pm \to l\nu)$ and $\mathrm{Br}(\chi_j^0 \to Z^*\chi_1^0 \to ll\chi_1^0) = \mathrm{Br}(Z \to ll)$ for kinematically forbidden region. The results are shown in Table E.1. The cut flows are defined in Sec. 5.5.1. The initial event number is normalized to the one of Ref. [115]. Our results agree with the ones of Ref. [115] within 10%. In particular, in the SR0τa16 which gives the strongest constraint in most of the parameter region, the acceptance in our analysis agrees very well with Ref. [115].

Second, in Table E.2, we compare the cross section and the acceptance of our analysis with those of the ATLAS analysis for the model points $(m_{\chi_2^0} = m_{\chi_1^\pm}, m_{\chi_1^0}) = (200, 50), (200, 25)$ and $(150, 37.5)$ GeV.[1] Here, the acceptance $A_{\mathrm{SR0}\tau\mathrm{a16}}$ is defined as Eq. (5.18). The effective acceptance of the ATLAS is calculated as $A^{\mathrm{ATLAS}}_{\mathrm{SR0}\tau\mathrm{a16}} = [A \times \epsilon]^{\mathrm{ATLAS}}_{\mathrm{SR0}\tau\mathrm{a16}} \times \mathrm{Br}(Z \to ll)^{-1}\mathrm{Br}(W^\pm \to l\nu)^{-1}$, where the acceptance times the efficiency $[A \times \epsilon]^{\mathrm{ATLAS}}_{\mathrm{SR0}\tau\mathrm{a16}}$ is taken from the HepData [116].[2] Compared

[1] These model points are chosen because the efficiency, the acceptance, and the production cross section in the ATLAS analysis are available in Ref. [116].

[2] In our simulation, the contributions from the hadronic decays of the W boson and the Z boson are negligibly small.

Point		$m_{\chi_2^0} = m_{\chi_1^\pm} = 175$ GeV, $m_{\chi_1^0} = 100$ GeV		
Source		ATLAS [50, 116]	CheckMATE [115]	our analysis
Generated events		20000	50000	50000
Initial Events		897 ± 0	897 ± 0	897 ± 0
3 isol. lep., no tau		148 ± 2.4	142 ± 1.5	138 ± 1.6
SFOS, $m_{\text{SFOS}} = 60$–81.2 GeV		78 ± 1.8	73.9 ± 1.1	67.7 ± 1.1
b-veto		75 ± 1.8	71.1 ± 1.1	65.8 ± 1.1
SR0τa9	$E_T^{\text{miss}} = 50$–75 GeV	20 ± 0.94	19.4 ± 0.58	17.7 ± 0.56
	$m_T = 0$–80 GeV	13 ± 0.76	13.5 ± 0.49	12.4 ± 0.47
	$\lvert m_{3\ell} - m_Z \rvert > 10$ GeV	10 ± 0.67	9.45 ± 0.41	8.16 ± 0.38
SR0τa10	$E_T^{\text{miss}} = 50$–75 GeV	20 ± 0.94	19.4 ± 0.58	17.7 ± 0.56
	$m_T \geq 80$ GeV	7 ± 0.56	5.95 ± 0.33	5.47 ± 0.31
SR0τa11	$E_T^{\text{miss}} \geq 75$ GeV	19 ± 0.91	18.8 ± 0.57	16.7 ± 0.55
	$m_T = 0$–100 GeV	15 ± 0.81	15.7 ± 0.53	13.9 ± 0.50
SR0τa12	$E_T^{\text{miss}} \geq 75$ GeV	19 ± 0.91	18.8 ± 0.57	16.7 ± 0.55
	$m_T \geq 100$ GeV	4 ± 0.42	3.07 ± 0.23	2.93 ± 0.23

Point		$m_{\chi_2^0} = m_{\chi_1^\pm} = 350$ GeV, $m_{\chi_1^0} = 50$ GeV		
Source		ATLAS [50, 116]	CheckMATE [115]	our analysis
Generated events		20000	50000	50000
Initial Events		49.2 ± 0	49.2 ± 0	49.2 ± 0
3 isol. lep., no tau		11 ± 0.14	11.9 ± 0.094	11.7 ± 0.11
SFOS, $m_{\text{SFOS}} = 81.2$–101.2 GeV		10 ± 0.14	9.87 ± 0.088	9.47 ± 0.097
b-veto		10 ± 0.14	9.39 ± 0.086	9.11 ± 0.095
SR0τa13	$E_T^{\text{miss}} = 50$–90 GeV	1.1 ± 0.051	1.03 ± 0.031	1.03 ± 0.032
	$m_T = 0$–110 GeV	0.6 ± 0.038	0.673 ± 0.026	0.671 ± 0.026
	$\lvert m_{3\ell} - m_Z \rvert > 10$ GeV	0.6 ± 0.038	0.665 ± 0.025	0.665 ± 0.026
SR0τa14	$E_T^{\text{miss}} \geq 90$ GeV	8 ± 0.13	7.87 ± 0.081	7.63 ± 0.0866
	$m_T = 0$–110 GeV	2.4 ± 0.075	2.53 ± 0.049	2.34 ± 0.048
SR0τa15	$E_T^{\text{miss}} = 50$–135 GeV	2.9 ± 0.082	2.78 ± 0.051	2.66 ± 0.051
	$m_T \geq 110$ GeV	1.6 ± 0.062	1.29 ± 0.035	1.25 ± 0.035
SR0τa16	$E_T^{\text{miss}} \geq 135$ GeV	7 ± 0.12	6.12 ± 0.073	6.00 ± 0.077
	$m_T \geq 110$ GeV	5 ± 0.11	4.4 ± 0.063	4.40 ± 0.066

Table E.1: The cut flow validation of the 8 TeV analysis is shown. The errors are the statistical errors of Monte-Carlo events.

$m_{\chi_2^0} = m_{\chi_1^\pm}, m_{\chi_1^0}$ [GeV]	$\sigma^{\rm NLO}_{\chi_1^\pm \chi_2^0}$ [fb]	$\sigma^{\rm ATLAS}_{\chi_1^\pm \chi_2^0}$ [fb]	$A_{\rm SR0\tau a16} \times 10^3$	$A^{\rm ATLAS}_{\rm SR0\tau a16} \times 10^3$
200, 50	788	802	15.5 ± 0.2	18.5
200, 25	788	802	20.3 ± 0.1	24.0
150, 37.5	2427	2452	2.26 ± 0.07	2.71

Table E.2: The validation of the cross section and the acceptance for the ATLAS 8 TeV analysis is shown. The errors for the acceptances are the statistical errors of Monte-Carlo events.

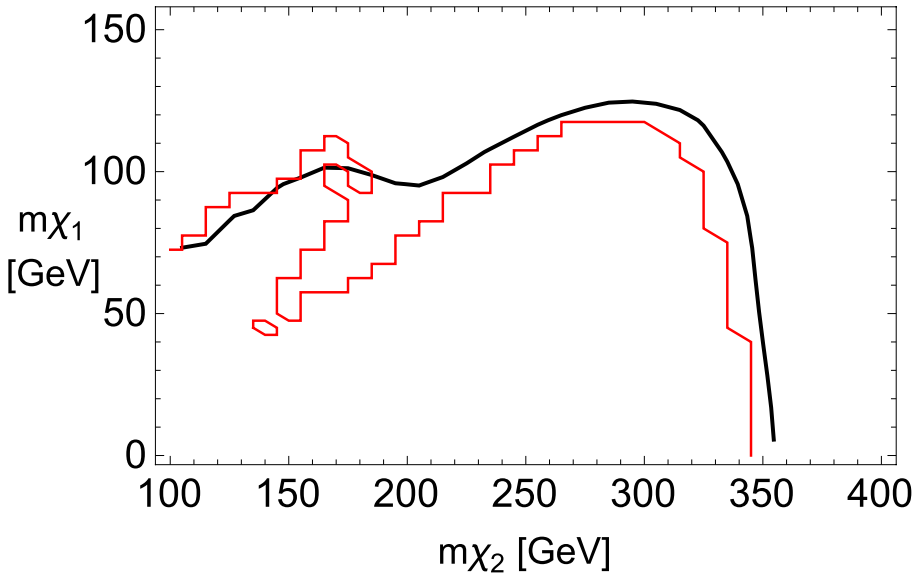

Figure E.1: The reinterpretation of the ATLAS 8 TeV analysis [50]. The black line shows the ATLAS result given in Ref. [50, 116]. The red line denotes the result of our analysis.

to the ATLAS analysis [50, 116], the estimated acceptance is about 20% smaller. The cross sections are well reproduced within 1–2%.

Finally, we perform the same analysis in the $(m_{\chi_2^0}, m_{\chi_1^0})$-plane, and show the exclusion contour in Figure E.1. Here, all the 20 SRs (SR0τa1–20) are taken into account. The ATLAS result [50] is shown in the black line (see also Figure 3.6).[3] The red line denotes the result of our analysis. In this plane, our results agree with the ATLAS analysis within 20%. Although the shape near the kinematical edge $m_{\chi_2^0} - m_{\chi_1^0} \sim M_Z$ seems to be different, the differences of the event numbers between our results and the ATLAS analysis are within 20%.

In order to check the differences between the simulation programs, we also simulate with Herwig++. The results using Herwig++ agree with the above results using MadGraph and PYTHIA within the statistical uncertainties of the Monte-Carlo events.

[3]The black line is drawn using the data of Ref. [116].

$(m_{\chi_2^0}, m_{\chi_1^0})$	SRA		SRB	
	ATLAS [51]	our analysis	ATLAS [51]	our analysis
(400,0)	407±6	408.8±7.3	224±5	209.2±5.2
(600,0)	194.8±2.0	205.8±3.1	148.9±1.7	153.4±2.6
(800,0)	69.6±0.6	68.6±0.9	59.1±0.6	58.7±0.8
(1000,0)	22.94±0.19	21.9±0.3	20.42±0.18	19.5±0.3
$(m_{\chi_2^0}, m_{\chi_1^0})$	SRC		SRD	
	ATLAS [51]	our analysis	ATLAS [51]	our analysis
(400,0)	67.9±2.6	55.8±2.7	19.7±1.4	14.9±1.4
(600,0)	81.6±1.3	78.6±1.9	33.5±0.8	28.9±1.1
(800,0)	42.4±0.5	41.2±0.7	25.2±0.4	22.9±0.5
(1000,0)	16.36±0.16	15.7±0.2	11.55±0.14	10.9±0.2

Table E.3: The validation of the number of events for the ATLAS 14 TeV analysis is shown. The errors are the statistical errors of Monte-Carlo events.

E.2 14 TeV

Here, we show the validation of our 14 TeV analysis. See also Sec. 5.5.2.

As a validation of our analysis, we simulate with the pure Bino-Wino model. In Table E.3, we show the comparison of the expected number of events at 3000 fb^{-1} for the model points $(m_{\chi_2^0} = m_{\chi_1^\pm}, m_{\chi_1^0})$ =(400,0), (600,0), (800,0), (1000,0) GeV. The ATLAS results are given in Ref. [51]. They are in good agreement with the ATLAS analysis.

We also show perform the validation for the $(m_{\chi_2^0}, m_{\chi_1^0})$-plane in Figure E.2. The exclusion limits are set by the method as written in Sec. 5.5.2. The envelopes denoted by the black lines are the discovery/exclusion prospects of our analysis where the yellow, red, blue and green lines denote the results from the SR A, B, C and D respectively. The black lines correspond to the black lines in Figure 3.6. Here, not only the 95% CL exclusion prospects (dashed lines) but also the 5 σ discovery prospects (solid lines) are shown. To calculate the 5 σ discovery prospects where $Z_N^X = 5$, we use the following value which is calculated as in Sec. 5.5.2

$$N^{\rm dis.A}(Z_N^{\rm dis.A} = 5) = 77.2\,, \tag{E.2}$$

$$N^{\rm dis.B}(Z_N^{\rm dis.B} = 5) = 43.7\,, \tag{E.3}$$

$$N^{\rm dis.C}(Z_N^{\rm dis.C} = 5) = 27.9\,, \tag{E.4}$$

$$N^{\rm dis.D}(Z_N^{\rm dis.D} = 5) = 22.4\,, \tag{E.5}$$

for 3000 fb^{-1}. As we can see, the results of the ATLAS can be reproduced.

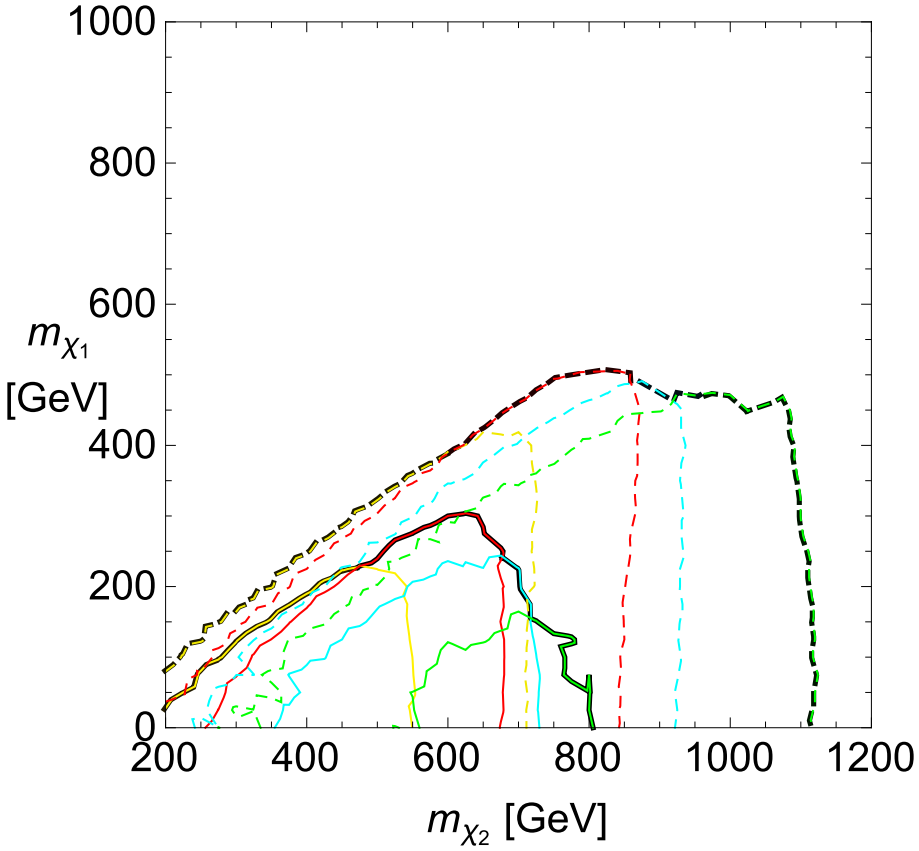

Figure E.2: The reinterpretation of the ATLAS 14 TeV analysis [51] is shown. The yellow, red, blue and green lines denote the results from the SR A, B, C and D respectively. The solid lines correspond to the 5 σ discovery prospects and the dashed lines correspond to the 95% CL exclusion prospects. The envelopes denoted by the black lines are the discovery/exclusion prospects of our analysis which correspond to the black lines in Figure 3.6.

Bibliography

[1] **ATLAS Collaboration** Collaboration, G. Aad *et al.*, "Observation of a new particle in the search for the Standard Model Higgs boson with the ATLAS detector at the LHC," *Phys.Lett.* **B716** (2012) 1–29, arXiv:1207.7214 [hep-ex].

[2] **CMS Collaboration** Collaboration, S. Chatrchyan *et al.*, "Observation of a new boson at a mass of 125 GeV with the CMS experiment at the LHC," *Phys.Lett.* **B716** (2012) 30–61, arXiv:1207.7235 [hep-ex].

[3] J. Wess and B. Zumino, "Supergauge Transformations in Four-Dimensions," *Nucl. Phys.* **B70** (1974) 39–50.

[4] S. P. Martin, "A Supersymmetry primer," arXiv:hep-ph/9709356 [hep-ph]. [Adv. Ser. Direct. High Energy Phys.18,1(1998)].

[5] **ATLAS** Collaboration, G. Aad *et al.*, "Summary of the searches for squarks and gluinos using $\sqrt{s} = 8$ TeV pp collisions with the ATLAS experiment at the LHC," *JHEP* **10** (2015) 054, arXiv:1507.05525 [hep-ex].

[6] Y. Okada, M. Yamaguchi, and T. Yanagida, "Upper bound of the lightest Higgs boson mass in the minimal supersymmetric standard model," *Prog.Theor.Phys.* **85** (1991) 1–6.

[7] Y. Okada, M. Yamaguchi, and T. Yanagida, "Renormalization group analysis on the Higgs mass in the softly broken supersymmetric standard model," *Phys.Lett.* **B262** (1991) 54–58.

[8] G. F. Giudice and A. Strumia, "Probing High-Scale and Split Supersymmetry with Higgs Mass Measurements," *Nucl. Phys.* **B858** (2012) 63–83, arXiv:1108.6077 [hep-ph].

[9] N. Arkani-Hamed and S. Dimopoulos, "Supersymmetric unification without low energy supersymmetry and signatures for fine-tuning at the LHC," *JHEP* **06** (2005) 073, arXiv:hep-th/0405159 [hep-th].

[10] G. F. Giudice and A. Romanino, "Split supersymmetry," *Nucl. Phys.* **B699** (2004) 65–89, arXiv:hep-ph/0406088 [hep-ph]. [Erratum: Nucl. Phys.B706,65(2005)].

[11] N. Arkani-Hamed, S. Dimopoulos, G. F. Giudice, and A. Romanino, "Aspects of split supersymmetry," *Nucl. Phys.* **B709** (2005) 3–46, arXiv:hep-ph/0409232 [hep-ph].

[12] L. J. Hall and Y. Nomura, "Spread Supersymmetry," *JHEP* **01** (2012) 082, arXiv:1111.4519 [hep-ph].

[13] L. J. Hall, Y. Nomura, and S. Shirai, "Spread Supersymmetry with Wino LSP: Gluino and Dark Matter Signals," *JHEP* **01** (2013) 036, arXiv:1210.2395 [hep-ph].

[14] M. Ibe and T. T. Yanagida, "The Lightest Higgs Boson Mass in Pure Gravity Mediation Model," *Phys. Lett.* **B709** (2012) 374–380, arXiv:1112.2462 [hep-ph].

[15] M. Ibe, S. Matsumoto, and T. T. Yanagida, "Pure Gravity Mediation with $m_{3/2} =$ 10-100TeV," *Phys. Rev.* **D85** (2012) 095011, arXiv:1202.2253 [hep-ph].

[16] B. Bhattacherjee, B. Feldstein, M. Ibe, S. Matsumoto, and T. T. Yanagida, "Pure gravity mediation of supersymmetry breaking at the Large Hadron Collider," *Phys. Rev.* **D87** no. 1, (2013) 015028, arXiv:1207.5453 [hep-ph].

[17] T. Moroi and M. Nagai, "Probing Supersymmetric Model with Heavy Sfermions Using Leptonic Flavor and CP Violations," *Phys. Lett.* **B723** (2013) 107–112, arXiv:1303.0668 [hep-ph].

[18] W. Altmannshofer, R. Harnik, and J. Zupan, "Low Energy Probes of PeV Scale Sfermions," *JHEP* **11** (2013) 202, arXiv:1308.3653 [hep-ph].

[19] **Planck** Collaboration, P. A. R. Ade *et al.*, "Planck 2015 results. XIII. Cosmological parameters," arXiv:1502.01589 [astro-ph.CO].

[20] J. Hisano, S. Matsumoto, M. Nagai, O. Saito, and M. Senami, "Non-perturbative effect on thermal relic abundance of dark matter," *Phys. Lett.* **B646** (2007) 34–38, arXiv:hep-ph/0610249 [hep-ph].

[21] M. Cirelli, A. Strumia, and M. Tamburini, "Cosmology and Astrophysics of Minimal Dark Matter," *Nucl. Phys.* **B787** (2007) 152–175, arXiv:0706.4071 [hep-ph].

[22] N. Nagata and S. Shirai, "Higgsino Dark Matter in High-Scale Supersymmetry," *JHEP* **01** (2015) 029, arXiv:1410.4549 [hep-ph].

[23] A. Birkedal-Hansen and B. D. Nelson, "The Role of Wino content in neutralino dark matter," *Phys. Rev.* **D64** (2001) 015008, arXiv:hep-ph/0102075 [hep-ph].

[24] **Michigan Center for Theoretical Physics, U. of Michigan** Collaboration, A. Birkedal-Hansen and B. D. Nelson, "Relic neutralino densities and detection rates with nonuniversal gaugino masses," *Phys. Rev.* **D67** (2003) 095006, arXiv:hep-ph/0211071 [hep-ph].

[25] S. Profumo and C. E. Yaguna, "Gluino coannihilations and heavy bino dark matter," *Phys. Rev.* **D69** (2004) 115009, arXiv:hep-ph/0402208 [hep-ph].

[26] H. Baer, A. Mustafayev, E.-K. Park, and S. Profumo, "Mixed wino dark matter: Consequences for direct, indirect and collider detection," *JHEP* **07** (2005) 046, arXiv:hep-ph/0505227 [hep-ph].

[27] H. Baer, T. Krupovnickas, A. Mustafayev, E.-K. Park, S. Profumo, and X. Tata, "Exploring the BWCA (bino-wino co-annihilation) scenario for neutralino dark matter," *JHEP* **12** (2005) 011, arXiv:hep-ph/0511034 [hep-ph].

[28] N. Arkani-Hamed, A. Delgado, and G. F. Giudice, "The Well-tempered neutralino," *Nucl. Phys.* **B741** (2006) 108–130, arXiv:hep-ph/0601041 [hep-ph].

[29] J. L. Feng, K. T. Matchev, and F. Wilczek, "Neutralino dark matter in focus point supersymmetry," *Phys. Lett.* **B482** (2000) 388–399, arXiv:hep-ph/0004043 [hep-ph].

[30] A. Pierce, "Dark matter in the finely tuned minimal supersymmetric standard model," *Phys. Rev.* **D70** (2004) 075006, arXiv:hep-ph/0406144 [hep-ph].

[31] M. Drees and M. M. Nojiri, "The Neutralino relic density in minimal $N = 1$ supergravity," *Phys. Rev.* **D47** (1993) 376–408, arXiv:hep-ph/9207234 [hep-ph].

[32] P. Grothaus, M. Lindner, and Y. Takanishi, "Naturalness of Neutralino Dark Matter," *JHEP* **07** (2013) 094, arXiv:1207.4434 [hep-ph].

[33] T. Han, Z. Liu, and A. Natarajan, "Dark matter and Higgs bosons in the MSSM," *JHEP* **11** (2013) 008, arXiv:1303.3040 [hep-ph].

[34] C. Han, "Probing light bino and higgsinos at the LHC," arXiv:1409.7000 [hep-ph].

[35] L. Calibbi, J. M. Lindert, T. Ota, and Y. Takanishi, "LHC Tests of Light Neutralino Dark Matter without Light Sfermions," *JHEP* **11** (2014) 106, arXiv:1410.5730 [hep-ph].

[36] M. Chakraborti, U. Chattopadhyay, A. Choudhury, A. Datta, and S. Poddar, "Reduced LHC constraints for higgsino-like heavier electroweakinos," *JHEP* **11** (2015) 050, arXiv:1507.01395 [hep-ph].

[37] K. Griest, "Cross-Sections, Relic Abundance and Detection Rates for Neutralino Dark Matter," *Phys. Rev.* **D38** (1988) 2357. [Erratum: Phys. Rev.D39,3802(1989)].

[38] C. Cheung, L. J. Hall, D. Pinner, and J. T. Ruderman, "Prospects and Blind Spots for Neutralino Dark Matter," *JHEP* **05** (2013) 100, arXiv:1211.4873 [hep-ph].

[39] M. Farina, M. Kadastik, D. Pappadopulo, J. Pata, M. Raidal, and A. Strumia, "Implications of XENON100 and LHC results for Dark Matter models," *Nucl. Phys.* **B853** (2011) 607–624, arXiv:1104.3572 [hep-ph].

[40] **LUX** Collaboration, D. S. Akerib *et al.*, "First results from the LUX dark matter experiment at the Sanford Underground Research Facility," *Phys. Rev. Lett.* **112** (2014) 091303, arXiv:1310.8214 [astro-ph.CO].

[41] **XENON1T** Collaboration, E. Aprile, "The XENON1T Dark Matter Search Experiment," *Springer Proc. Phys.* **148** (2013) 93–96, arXiv:1206.6288 [astro-ph.IM].

[42] **XENON100** Collaboration, E. Aprile *et al.*, "Limits on spin-dependent WIMP-nucleon cross sections from 225 live days of XENON100 data," *Phys. Rev. Lett.* **111** no. 2, (2013) 021301, arXiv:1301.6620 [astro-ph.CO].

[43] M. Garny, A. Ibarra, M. Pato, and S. Vogl, "On the spin-dependent sensitivity of XENON100," *Phys. Rev.* **D87** no. 5, (2013) 056002, arXiv:1211.4573 [hep-ph].

[44] P. P. Giardino, K. Kannike, I. Masina, M. Raidal, and A. Strumia, "The universal Higgs fit," *JHEP* **05** (2014) 046, arXiv:1303.3570 [hep-ph].

[45] G. Belanger, B. Dumont, U. Ellwanger, J. F. Gunion, and S. Kraml, "Global fit to Higgs signal strengths and couplings and implications for extended Higgs sectors," *Phys. Rev.* **D88** (2013) 075008, arXiv:1306.2941 [hep-ph].

[46] H. Okawa, J. Kunkle, and E. Lipeles, "Prospects on the search for invisible Higgs decays in the ZH channel at the LHC and HL-LHC: A Snowmass White Paper," in *Community Summer Study 2013: Snowmass on the Mississippi (CSS2013) Minneapolis, MN, USA, July 29-August 6, 2013*. 2013. arXiv:1309.7925 [hep-ex]. http://inspirehep.net/record/1256093/files/arXiv:1309.7925.pdf.

[47] S. Dawson *et al.*, "Working Group Report: Higgs Boson," in *Community Summer Study 2013: Snowmass on the Mississippi (CSS2013) Minneapolis, MN, USA, July 29-August 6, 2013*. 2013. arXiv:1310.8361 [hep-ex]. http://inspirehep.net/record/1262795/files/arXiv:1310.8361.pdf.

[48] D. M. Asner *et al.*, "ILC Higgs White Paper," in *Community Summer Study 2013: Snowmass on the Mississippi (CSS2013) Minneapolis, MN, USA, July 29-August 6, 2013*. 2013. arXiv:1310.0763 [hep-ph]. http://inspirehep.net/record/1256491/files/arXiv:1310.0763.pdf.

[49] **SLD Electroweak Group, DELPHI, ALEPH, SLD, SLD Heavy Flavour Group, OPAL, LEP Electroweak Working Group, L3** Collaboration, S. Schael

et al., "Precision electroweak measurements on the Z resonance," *Phys. Rept.* **427** (2006) 257–454, arXiv:hep-ex/0509008 [hep-ex].

[50] **ATLAS** Collaboration, G. Aad *et al.*, "Search for direct production of charginos and neutralinos in events with three leptons and missing transverse momentum in $\sqrt{s} =$ 8TeV pp collisions with the ATLAS detector," *JHEP* **04** (2014) 169, arXiv:1402.7029 [hep-ex].

[51] **ATLAS** Collaboration, "Search for Supersymmetry at the high luminosity LHC with the ATLAS Detector.," ATLAS-PHYS-PUB-2014-010.

[52] K. Hamaguchi and K. Ishikawa, "Prospects for Higgs- and Z-resonant Neutralino Dark Matter," arXiv:1510.05378 [hep-ph].

[53] S. R. Coleman and E. J. Weinberg, "Radiative Corrections as the Origin of Spontaneous Symmetry Breaking," *Phys. Rev.* **D7** (1973) 1888–1910.

[54] S. Weinberg, "Implications of Dynamical Symmetry Breaking," *Phys. Rev.* **D13** (1976) 974–996.

[55] S. Weinberg, "Implications of Dynamical Symmetry Breaking: An Addendum," *Phys. Rev.* **D19** (1979) 1277–1280.

[56] E. Gildener, "Gauge Symmetry Hierarchies," *Phys. Rev.* **D14** (1976) 1667.

[57] L. Susskind, "Dynamics of Spontaneous Symmetry Breaking in the Weinberg-Salam Theory," *Phys. Rev.* **D20** (1979) 2619–2625.

[58] **ATLAS, CMS** Collaboration, G. Aad *et al.*, "Combined Measurement of the Higgs Boson Mass in pp Collisions at $\sqrt{s} = 7$ and 8 TeV with the ATLAS and CMS Experiments," *Phys. Rev. Lett.* **114** (2015) 191803, arXiv:1503.07589 [hep-ex].

[59] **Super-Kamiokande** Collaboration, H. Nishino *et al.*, "Search for Proton Decay via p $\to$ e+ pi0 and p $\to$ mu+ pi0 in a Large Water Cherenkov Detector," *Phys. Rev. Lett.* **102** (2009) 141801, arXiv:0903.0676 [hep-ex].

[60] **ATLAS** Collaboration, G. Aad *et al.*, "ATLAS Run 1 searches for direct pair production of third-generation squarks at the Large Hadron Collider," *Eur. Phys. J.* **C75** no. 10, (2015) 510, arXiv:1506.08616 [hep-ex].

[61] **MEG** Collaboration, J. Adam *et al.*, "New constraint on the existence of the $\mu^+ \to e^+\gamma$ decay," *Phys. Rev. Lett.* **110** (2013) 201801, arXiv:1303.0754 [hep-ex].

[62] J. Hisano, T. Moroi, K. Tobe, and M. Yamaguchi, "Lepton flavor violation via right-handed neutrino Yukawa couplings in supersymmetric standard model," *Phys. Rev.* **D53** (1996) 2442–2459, arXiv:hep-ph/9510309 [hep-ph].

[63] **Particle Data Group** Collaboration, K. A. Olive *et al.*, "Review of Particle Physics," *Chin. Phys.* **C38** (2014) 090001.

[64] L. Randall and R. Sundrum, "Out of this world supersymmetry breaking," *Nucl. Phys.* **B557** (1999) 79–118, arXiv:hep-th/9810155 [hep-th].

[65] G. F. Giudice, M. A. Luty, H. Murayama, and R. Rattazzi, "Gaugino mass without singlets," *JHEP* **12** (1998) 027, arXiv:hep-ph/9810442 [hep-ph].

[66] M. Ibe, T. Moroi, and T. T. Yanagida, "Possible Signals of Wino LSP at the Large Hadron Collider," *Phys. Lett.* **B644** (2007) 355–360, arXiv:hep-ph/0610277 [hep-ph].

[67] S. Asai, T. Moroi, and T. T. Yanagida, "Test of Anomaly Mediation at the LHC," *Phys. Lett.* **B664** (2008) 185–189, arXiv:0802.3725 [hep-ph].

[68] T. Moroi and K. Nakayama, "Wino LSP detection in the light of recent Higgs searches at the LHC," *Phys. Lett.* **B710** (2012) 159–163, arXiv:1112.3123 [hep-ph].

[69] T. Cohen, M. Lisanti, A. Pierce, and T. R. Slatyer, "Wino Dark Matter Under Siege," *JCAP* **1310** (2013) 061, arXiv:1307.4082.

[70] J. Fan and M. Reece, "In Wino Veritas? Indirect Searches Shed Light on Neutralino Dark Matter," *JHEP* **10** (2013) 124, arXiv:1307.4400 [hep-ph].

[71] A. Hryczuk, I. Cholis, R. Iengo, M. Tavakoli, and P. Ullio, "Indirect Detection Analysis: Wino Dark Matter Case Study," *JCAP* **1407** (2014) 031, arXiv:1401.6212 [astro-ph.HE].

[72] B. Bhattacherjee, M. Ibe, K. Ichikawa, S. Matsumoto, and K. Nishiyama, "Wino Dark Matter and Future dSph Observations," *JHEP* **07** (2014) 080, arXiv:1405.4914 [hep-ph].

[73] M. Ibe, S. Matsumoto, S. Shirai, and T. T. Yanagida, "Wino Dark Matter in light of the AMS-02 2015 Data," *Phys. Rev.* **D91** no. 11, (2015) 111701, arXiv:1504.05554 [hep-ph].

[74] K. Hamaguchi, T. Moroi, and K. Nakayama, "AMS-02 Antiprotons from Annihilating or Decaying Dark Matter," *Phys. Lett.* **B747** (2015) 523–528, arXiv:1504.05937 [hep-ph].

[75] D. Feldman, Z. Liu, and P. Nath, "Gluino NLSP, Dark Matter via Gluino Coannihilation, and LHC Signatures," *Phys. Rev.* **D80** (2009) 015007, arXiv:0905.1148 [hep-ph].

[76] K. Harigaya, K. Kaneta, and S. Matsumoto, "Gaugino coannihilations," *Phys. Rev.* **D89** no. 11, (2014) 115021, arXiv:1403.0715 [hep-ph].

[77] N. Nagata, H. Otono, and S. Shirai, "Probing Bino-Wino Coannihilation at the LHC," *JHEP* **10** (2015) 086, arXiv:1506.08206 [hep-ph].

[78] G. Steigman, B. Dasgupta, and J. F. Beacom, "Precise Relic WIMP Abundance and its Impact on Searches for Dark Matter Annihilation," *Phys. Rev.* **D86** (2012) 023506, arXiv:1204.3622 [hep-ph].

[79] P. Gondolo and G. Gelmini, "Cosmic abundances of stable particles: Improved analysis," *Nucl. Phys.* **B360** (1991) 145–179.

[80] O. Buchmueller, M. J. Dolan, S. A. Malik, and C. McCabe, "Characterising dark matter searches at colliders and direct detection experiments: Vector mediators," *JHEP* **01** (2015) 037, arXiv:1407.8257 [hep-ph].

[81] **DELPHI** Collaboration, J. Abdallah *et al.*, "Photon events with missing energy in e+ e- collisions at s**(1/2) = 130-GeV to 209-GeV," *Eur. Phys. J.* **C38** (2005) 395–411, arXiv:hep-ex/0406019 [hep-ex].

[82] **CMS** Collaboration, V. Khachatryan *et al.*, "Searches for electroweak production of charginos, neutralinos, and sleptons decaying to leptons and W, Z, and Higgs bosons in pp collisions at 8 TeV," *Eur. Phys. J.* **C74** no. 9, (2014) 3036, arXiv:1405.7570 [hep-ex].

[83] **CMS** Collaboration, C. Collaboration, "Study of the Discovery Reach in Searches for Supersymmetry at CMS with 3000/fb,".

[84] **CMS** Collaboration, "Search for new physics in monojet events in pp collisions at sqrt(s)= 8 TeV,".

[85] **Fermi-LAT** Collaboration, M. Ackermann *et al.*, "Searching for Dark Matter Annihilation from Milky Way Dwarf Spheroidal Galaxies with Six Years of Fermi Large Area Telescope Data," *Phys. Rev. Lett.* **115** no. 23, (2015) 231301, arXiv:1503.02641 [astro-ph.HE].

[86] **Super-Kamiokande** Collaboration, K. Choi *et al.*, "Search for neutrinos from annihilation of captured low-mass dark matter particles in the Sun by Super-Kamiokande," *Phys. Rev. Lett.* **114** no. 14, (2015) 141301, arXiv:1503.04858 [hep-ex].

[87] G. Bertone, D. Hooper, and J. Silk, "Particle dark matter: Evidence, candidates and constraints," *Phys. Rept.* **405** (2005) 279–390, arXiv:hep-ph/0404175 [hep-ph].

[88] J. D. Lewin and P. F. Smith, "Review of mathematics, numerical factors, and corrections for dark matter experiments based on elastic nuclear recoil," *Astropart. Phys.* **6** (1996) 87–112.

[89] M. C. Smith *et al.*, "The RAVE Survey: Constraining the Local Galactic Escape Speed," *Mon. Not. Roy. Astron. Soc.* **379** (2007) 755–772, arXiv:astro-ph/0611671 [astro-ph].

[90] G. Belanger, F. Boudjema, A. Pukhov, and A. Semenov, "Dark matter direct detection rate in a generic model with micrOMEGAs 2.2," *Comput. Phys. Commun.* **180** (2009) 747–767, arXiv:0803.2360 [hep-ph].

[91] G. Belanger, F. Boudjema, A. Pukhov, and A. Semenov, "micrOMEGAs_3: A program for calculating dark matter observables," *Comput. Phys. Commun.* **185** (2014) 960–985, arXiv:1305.0237 [hep-ph].

[92] G. Blanger, F. Boudjema, A. Pukhov, and A. Semenov, "micrOMEGAs4.1: two dark matter candidates," *Comput. Phys. Commun.* **192** (2015) 322–329, arXiv:1407.6129 [hep-ph].

[93] O. Wantz and E. P. S. Shellard, "Axion Cosmology Revisited," *Phys. Rev.* **D82** (2010) 123508, arXiv:0910.1066 [astro-ph.CO].

[94] **JLQCD** Collaboration, H. Ohki, K. Takeda, S. Aoki, S. Hashimoto, T. Kaneko, H. Matsufuru, J. Noaki, and T. Onogi, "Nucleon strange quark content from $N_f = 2 + 1$ lattice QCD with exact chiral symmetry," *Phys. Rev.* **D87** (2013) 034509, arXiv:1208.4185 [hep-lat].

[95] **HERMES** Collaboration, A. Airapetian *et al.*, "Precise determination of the spin structure function g(1) of the proton, deuteron and neutron," *Phys. Rev.* **D75** (2007) 012007, arXiv:hep-ex/0609039 [hep-ex].

[96] G. K. Mallot, "The Spin structure of the nucleon," *Int. J. Mod. Phys.* **A15S1** (2000) 521–537, arXiv:hep-ex/9912040 [hep-ex].

[97] J. Alwall, R. Frederix, S. Frixione, V. Hirschi, F. Maltoni, O. Mattelaer, H. S. Shao, T. Stelzer, P. Torrielli, and M. Zaro, "The automated computation of tree-level and next-to-leading order differential cross sections, and their matching to parton shower simulations," *JHEP* **07** (2014) 079, arXiv:1405.0301 [hep-ph].

[98] T. Sjostrand, S. Mrenna, and P. Z. Skands, "PYTHIA 6.4 Physics and Manual," *JHEP* **05** (2006) 026, arXiv:hep-ph/0603175 [hep-ph].

[99] **DELPHES 3** Collaboration, J. de Favereau, C. Delaere, P. Demin, A. Giammanco, V. Lematre, A. Mertens, and M. Selvaggi, "DELPHES 3, A modular framework for fast simulation of a generic collider experiment," *JHEP* **02** (2014) 057, arXiv:1307.6346 [hep-ex].

[100] W. Beenakker, R. Hopker, M. Spira, and P. M. Zerwas, "Squark and gluino production at hadron colliders," *Nucl. Phys.* **B492** (1997) 51–103, arXiv:hep-ph/9610490 [hep-ph].

[101] W. Beenakker, M. Klasen, M. Kramer, T. Plehn, M. Spira, and P. M. Zerwas, "The Production of charginos / neutralinos and sleptons at hadron colliders," *Phys. Rev. Lett.* **83** (1999) 3780–3783, arXiv:hep-ph/9906298 [hep-ph]. [Erratum: Phys. Rev. Lett.100,029901(2008)].

[102] J. Pumplin, D. R. Stump, J. Huston, H. L. Lai, P. M. Nadolsky, and W. K. Tung, "New generation of parton distributions with uncertainties from global QCD analysis," *JHEP* **07** (2002) 012, arXiv:hep-ph/0201195 [hep-ph].

[103] M. Cacciari, G. P. Salam, and G. Soyez, "The Anti-k(t) jet clustering algorithm," *JHEP* **04** (2008) 063, arXiv:0802.1189 [hep-ph].

[104] M. Drees, H. Dreiner, D. Schmeier, J. Tattersall, and J. S. Kim, "CheckMATE: Confronting your Favourite New Physics Model with LHC Data," *Comput. Phys. Commun.* **187** (2014) 227–265, arXiv:1312.2591 [hep-ph].

[105] M. Cacciari and G. P. Salam, "Dispelling the N^3 myth for the k_t jet-finder," *Phys. Lett.* **B641** (2006) 57–61, arXiv:hep-ph/0512210 [hep-ph].

[106] M. Cacciari, G. P. Salam, and G. Soyez, "FastJet User Manual," *Eur. Phys. J.* **C72** (2012) 1896, arXiv:1111.6097 [hep-ph].

[107] J. T. Linnemann, "Measures of significance in HEP and astrophysics," *eConf* **C030908** (2003) MOBT001, arXiv:physics/0312059 [physics.data-an].

[108] A. Djouadi, "The Anatomy of electro-weak symmetry breaking. I: The Higgs boson in the standard model," *Phys. Rept.* **457** (2008) 1–216, arXiv:hep-ph/0503172 [hep-ph].

[109] P. Cushman *et al.*, "Working Group Report: WIMP Dark Matter Direct Detection," in *Community Summer Study 2013: Snowmass on the Mississippi (CSS2013) Minneapolis, MN, USA, July 29-August 6, 2013*. 2013. arXiv:1310.8327 [hep-ex]. http://inspirehep.net/record/1262767/files/arXiv:1310.8327.pdf.

[110] M. Bahr *et al.*, "Herwig++ Physics and Manual," *Eur. Phys. J.* **C58** (2008) 639–707, arXiv:0803.0883 [hep-ph].

[111] J. Lindert, "private communication,".

[112] M. A. Shifman, A. I. Vainshtein, and V. I. Zakharov, "Remarks on Higgs Boson Interactions with Nucleons," *Phys. Lett.* **B78** (1978) 443.

[113] J. Hisano, R. Nagai, and N. Nagata, "Effective Theories for Dark Matter Nucleon Scattering," *JHEP* **05** (2015) 037, arXiv:1502.02244 [hep-ph].

[114] M. V. Polyakov, A. Schafer, and O. V. Teryaev, "The Intrinsic charm contribution to the proton spin," *Phys. Rev.* **D60** (1999) 051502, arXiv:hep-ph/9812393 [hep-ph].

[115] "http://checkmate.hepforge.org/analyseslist/validatedlist.html,".

[116] "http://atlas.web.cern.ch/atlas/groups/physics/papers/susy-2013-12/,".